Universitat Politècnica de Catalunya

Three-dimensional SPH simulations of the interaction between the nova ejecta and the companion star

Author:

Joana Figueira

Thesis submitted for the degree of

Doctor of Philosophy

Advisor:

Jordi José

Barcelona, March 2023

Ao Diego e ao nosso caminho

Contents

Acknowledgements

It has been a bumpy adventure... I wish to thank everyone who took part in the ups and downs, and to the Spanish MINECO grant AYA2014–59084–P, which, together with the AGAUR/ Generalitat de Catalunya grant SGR0038/2014 funded, this crazy trip.

I started this adventure with the best advisors I could ask for, Jordi José and Enrique García-Berro. Jordi, I don't even know how can I begin to thank you... You've always been there, and without you this road would have been even bumpier (or have led to a dead end). So, thank you so much for all your support, your infinite patience, and your sense of humor that made this Thesis possible! Enrique, thank you for always pushing me to go one step further. Your unexpected and premature departure is a great loss and was one of the worst moments of this process! I can only be grateful for having met you and having you as my advisor.

I would also like to thank Domingo García-Senz for having his door always open for unsolicited questions! To Ruben Cabezón for many fruitful discussions and exchanges. Shazreene Mohamed and Simon Campbell, for giving me the pleasure of working together. And especially to Jordi Casanova, Anuj Parik, Fermin Moreno, Gloria Sala, and Yago Herrera for making it easier and fun! I would also like to thank Ana Maria Ortega for all her help with all the needed paperwork, and her patience with all my never-ending questions.

It has been a long ride, and a lot of people have helped me, even if they were not aware of it... Thank you Barros, Judit, Helder, Victor, Laia, Laura, Glori, Adri, Ana, Rita, Kaba, Djudju, Telmo, Caio, Miguel for helping me to disconnect, so I could connect again with a more clear mindset.

To my team at Som, especially to Xavi, Joan, Oriol, Juanpe, Voki, Marta, Benji, Gil, Bea, Marité and Javi for their understanding, support, and originality in making me laugh! To Marc, Anna, Nuria, and Monica for their warmth and encouragement. To Pol, for putting things in perspective when I most needed it. And a special thanks to Jordi, who, in a humble and silent way, provided me with the help that I needed, without which this journey would have taken me even longer!

To my family, thank you for always being there! To my aunt Mimi, to my brothers, sister, sister in law, nephews, niece and cousins. To my grandmother, that in one way or another is always by my side! And especially to my mom, for her encouragement in every single step! Even faraway, you always made me feel close to home.

And finally to Diego, who has been part of this trip since the beginning (even without buying a ticket) and helped me through every single bump! Gracias fofo!

I am really grateful for getting the chance to pursue these incredible binary systems, which only made sense with all of you! Without all your support, this would have been an impossible quest! Thank you so much!

List of Figures

List of Tables

Chapter 1

Introduction

1.1 Stella novae

The first reported observations of novae go back to approximately 200 BC in China (Duerbeck 2008). At that time, any celestial body exhibiting a sudden and unexpected increase in brightness, fading away after days to months, was labeled as a *stella nova* (latin for "new star"). Back then, there was no distinction between (classical) novae and supernovae. In fact, the differentiation between both phenomena came much later. Only after Hubble established the distance scale to galaxies, in the mid twenties (1923 - 1924), it became clear that different classes of *stella novae* must exist. Since some novae, such as S Andromedae, could be placed outside of the Milky Way, they had to be considerably more energetic than other galactic events. Thus, in 1925, Lundmark proposed a division of novae into two different classes: "lower-class" and "upper-class". The latter, being extremely bright novae, were renamed as "supernovae" by Baade & Zwicky. A few years later, Baade (1938) showed, from photometric and spectroscopic studies, that the previously defined classes were in fact two different types of objects that he referred to as "common novae" and "supernovae".

The physics behind these "common novae" and the origin of their outbursts was first proposed nearly twenty years later by Schatzman (1951), who theorized that such events had a thermonuclear origin. In parallel, Kraft, guided by observations of DQ Her (Walker 1954), was able to show that cataclysmic variables (and novae, in particular) involve close stellar binary systems (Kraft 1964). Indeed, he suggested that novae take place in stellar systems composed of a white dwarf (WD) that is accreting hydrogen-rich matter via an accretion disk from a red dwarf companion. Mass accumulation on top of the WD drives the outburst. After many attempts to understand the physics behind such explosions, it was Starrfield (1971a,b) who first suggested that a CNO enhancement was needed to trigger the nova eruption (at least, to reproduce their gross observational features).

Since then, our understanding of these now called "classical nova" systems (a term that started to be broadly used after Warner 1972) has greatly increased. By combining the efforts in different fronts, from observations (photometry, spectroscopy) at different wavelengths to nuclear experiments, as well as numerical simulations, much has been accomplished in understanding these unique stellar explosions.

In this Thesis we will make our contribution by looking into the long-term dynamical evolution of these systems, since most of the efforts undertaken in modeling nova outbursts

have been focused on the early stages of the explosion and ejection (see Starrfield *et al.* 2008, 2016; José & Shore 2008; José 2016, for recent reviews). Therefore, key aspects of the evolution of these systems, associated with the interaction of the ejecta, first with the accretion disk orbiting the white dwarf, and ultimately with the secondary star, have been largely unexplored[1].

1.2 Cataclysmic variables: origin, nature, and classification

Classical and Recurrent Novae are a type of Cataclysmic variables (CVs), that is, stars that exhibit an irregular increase in brightness by a huge factor[2], after which they return to quiescence. CVs consist of two components: a (accreting) white dwarf primary star and a mass-transferring (or donor) secondary. CVs are subdivided into several groups, that include supernovae type Ia, classical and recurrent novae, dwarf novae, and other subclasses designated after a bright prototype, such as VY Sculptoris, AM Canum Venaticorum, SW Sextantis, and Z Andromedae (see Warner 2009, for an in-depth analysis of the different types of CVs and their properties).

Depending on how strong the primary magnetic field is, CVs can be grouped in:

- Polar ($B \gtrsim 10^7$ G)
- Intermediate Polar (IP) ($10^6 \lesssim B \lesssim 10^7$ G)
- Non-magnetic

For the Polar and IP types, the material that is being transferred is accreted along the magnetic poles of the primary. If the magnetic field is too strong, as in polar CVs, the formation of an accretion disk is prevented. For IPs, an accretion disk can be formed up to the magnetospheric boundary, where the magnetic field of the WD takes over and truncates the accretion disk. In non-magnetic CVs an accretion disk is formed reaching the surface of the WD primary. It is, however, worth noting that different classifications of CVs exist. Smith (2006), for instance, just considers three main subgroups (novae, dwarf novae, and magnetic novae), and leave aside from the CV category other objects (e.g., AM Canum Venaticorum stars).

The CV formation path, depicted in Figure 1.1, is only possible if the initial binary exhibits specific features, e.g., it is essential that the initial binary is composed of two main-sequence (MS) stars (upper panel): a low-mass star as the secondary and an intermediate-mass primary, which is required for the formation of a partially electron-degenerate core. Such core can only be formed if the latter does not fill its Roche lobe[3] before its formation.

[1] We note, however, that a similar scenario, the interaction between the material ejected in a type Ia supernova and the companion star, has been addressed in a number of papers (see, e.g, Marietta *et al.* 2000; García-Senz *et al.* 2012).

[2] Recurrent novae brighten typically by 9 magnitudes, whereas classical novae may brighten by more than 12 magnitudes (Schaefer 2010). Other CV subclasses, like dwarf novae, experience more modest variations (becoming 6 to 100 times brighter than in quiescence).

[3] In a binary system, the Roche lobe defines a closed region that encircles each star. Matter inside such region is gravitationally bound to a star and cannot escape it, except in the case where its size exceeds the Roche lobe radius and matter can be transferred to its companion. This is called Roche Lobe overflow (RLOF).

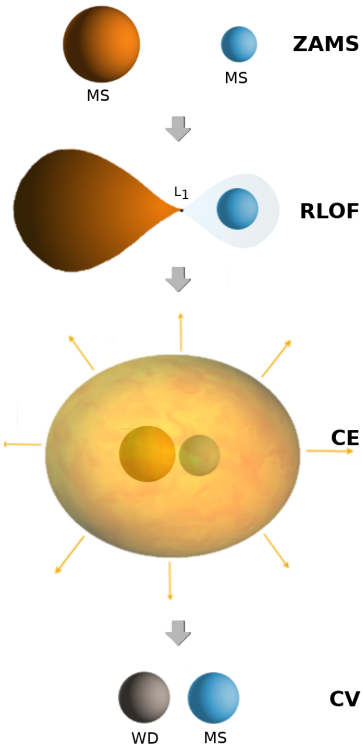

Figure 1.1: Schematic representation of the evolution of a binary system towards a cataclysmic variable one (not to scale).

Thus, their initial orbital separation has to be large enough ($\sim 100\ R_\odot$). Initially, both stars are well inside their Roche lobes (see upper panel). As stellar evolution proceeds, the more massive one will evolve faster becoming a red giant (RG)[4] or an asymptotic giant branch (AGB)[5] star. At this stage, the aforementioned core has already been developed and the star is able to fill its Roche lobe (second panel). Thus, matter can now be transferred to the companion through the inner Lagrangian point (L1)[6]. Due to the nature of the primary (for more details on mass transfer, see, for example, Eggleton 2006), the process of mass transfer happens very rapidly preventing the companion from accreting all the incoming material. Therefore, the material will be built on top of the secondary leading to its Roche lobe overflow and consequently drive the system to a common envelope (CE) configuration (third panel). At this point, the friction exerted by the binary and the outer envelope will

[4]Stellar phase that follows after the main-sequence one. As the main-sequence phase proceeds, the hydrogen burning core gradually gives place to an helium one. During this process, and while an hydrogen shell surrounding the core keeps burning, the core contracts due to its gravity. Forcing the outer layers to expand (100 - 1000 $R_\odot$) towards lower temperatures becoming a red giant.

[5]This phase is the final nuclear burning phase, where the helium in the core is converted into carbon and oxygen. The He-burning shell, that surrounds the core, gradually adds mass to the growing CO core, which becomes degenerate. The star expands towards lower temperatures becoming an asymptotic giant branch star.

[6]Point where the gravitational equipotentials around both stars, that is, the Roche Lobes, touch each other.

force the secondary to lose angular momentum spiraling towards smaller separations and consequently the envelope is ejected (Paczynski 1976). This crucial stage provides us with a close binary composed of a white dwarf (WD) (CO- or ONe-rich, depending on the initial mass of the star) and a low-mass MS star - that is, a Cataclysmic Variable (CV) system (lower panel).

It is worth mentioning, even though it is out of the scope of the current study, that this standard theory has some drawbacks: numerical simulations of pre-cataclysmic variable populations cannot predict the observed WD masses in CVs, the minimum orbital period, or its space density. However, recent studies performed by Schreiber *et al.* (2016), and independently by Nelemans *et al.* (2016), offer a possible solution that relies on frictional angular momentum losses after the initial outburst (or outbursts).

1.3 Classical novae

This Thesis mostly focuses on the classical nova (CN) and recurrent nova (RN) subtypes, in which the underlying CO- or ONe-WD that hosts the outburst is not (or is weakly) magnetized, and the resulting explosion is triggered by a thermonuclear runaway (TNR). This outburst is a consequence of the piling up of matter on top of the WD, fed by the accretion disk (see Section 1.7.1). Even though such events are quite violent, releasing typically 10^{45} ergs per outburst, the close stellar binary system is not disrupted by the explosion. In fact, shortly after the outburst, mass transfer resumes, which ultimately leads to another outburst. The recurrence time between outbursts depends on details of the binary itself (e.g., mass of the white dwarf, rate and composition of the accreted material...): it is expected that classical nova outbursts recur typically every 10^4 - 10^5 yr, reaching peak luminosities about $10^5 L_{\odot}$. However, the subclass of recurrent novae (by definition, novae observed in outburst more than once), show much shorter recurrence times, ranging from 1 year (Darnley *et al.* 2014, for M31N 2008-12a) to about hundred years[7] (Schaefer 2010, for V2487 Ophiuchi), requiring extreme conditions.

Nova outbursts are not uncommon, and even though only 5 to 10 systems are typically discovered per year, the predicted nova rate is actually much higher: estimates yield $50\ ^{+31}_{-23}$ novae per year in the Milky Way (Shafter 2017), while for Andromeda (M31) the rate increases to 60^{+16}_{-15} per year (Darnley *et al.* 2006), or according to Soraisam *et al.* (2016) to approximately 106 novae per year. The reason for the mismatch between the number of observed novae and the predicted rate is due to a number of issues, including extinction from interstellar dust, or the apparent location of the CV (i.e., eruptions occurring along a line of sight that passes close to the Sun). Indeed, studies performed by Schaefer (2014) showed a low efficiency of discovery: for novae with peak apparent magnitude of 6 the efficiency is 22 %, while for novae with V = 10 mag the efficiency drops to 9%. It is worth noting that about 800 nova candidates have been reported from M31 (Pietsch 2010), and nearly 400 from our own Galaxy, from which roughly 100 are expected to be RN masqueraded as CN (Pagnotta & Schaefer 2014). Those numbers are increasing rapidly as more systematic and deeper sky surveys are being conducted. It is also worth mentioning that amateur astronomers have greatly contributed to the discovery of these novae and continue to do so.

CN systems, as can be seen from the observed orbital period distribution shown in Fig.1.2

[7] Theoretical models can result in even shorter recurrence times, of about 25 - 50 days (Hillman *et al.* 2015; Hachisu *et al.* 2016).

(Diaz & Bruch 1997), are characterized by short orbital periods ranging between 1 and 10 hours. In fact, larger orbital periods would require a more evolved companion to fill its Roche lobe. The orbital period provides useful insight on the nature of the system itself, since it puts constraints on the mass of each component, and hence, on the nature of the secondary.

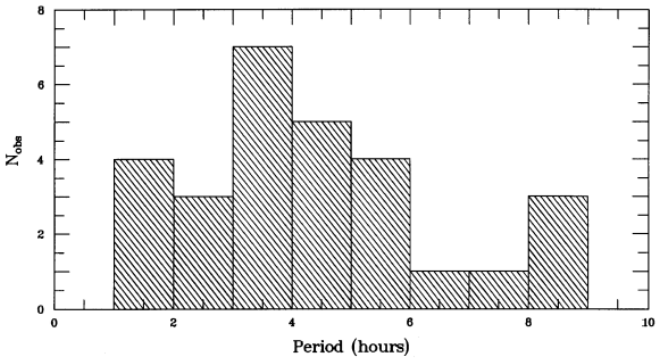

Figure 1.2: Orbital period distribution for Classical Novae. Taken from Diaz & Bruch (1997)

In CN systems, the companion is typically a low mass, K-M dwarf, main-sequence star (although observations demonstrate the presence of more evolved companions). When the secondary nearly overfills its Roche lobe, its mass, M_2, can be inferred from the orbital period (P_{orb}) through the relation (Warner 2009):

$$\frac{M_2}{M_\odot} = 0.065 P_{orb}^{\frac{5}{4}}(hour) \tag{1.1}$$

A full nova cycle is driven by a mass transfer episode from the companion star, a fraction of which is accreted by the WD, powering an eruption and mass loss, until the next accretion stage resumes (Prialnik 1986). The eruption itself, is initiated at the base of the accreted envelope via a TNR (Shara 1989; Starrfield *et al.* 2008). In a typical nova outburst, material is ejected at typical velocities around several thousand km s^{-1}. Usually, the more massive the primary is, the faster the ejection velocities. The primary star can be a CO- or an ONe-WD depending on the initial mass of its progenitor. Typically, a CO-WD has a less massive progenitor ($\lesssim$ 8 $M_\odot$) than an ONe-WD (8 to 10 $M_\odot$, even though the exact limits leading to a CO- and/or an ONe-WD are a matter of debate). As a result, the latter is expected to be more massive than its CO counterpart. Even though a clear threshold has not been established, an approximate value of about 1.1 $M_\odot$ has been proposed by Hurley *et al.* (2000) and Catalán *et al.* (2008).

1.4 Recurrent novae

The extremely short recurrent times that characterize recurrent novae require very high mass-accretion rates, white dwarf masses close to the Chandrasekhar limit, and very high initial white dwarf luminosities or temperatures (e.g. Starrfield *et al.* 1988; Yaron *et al.* 2005). In such massive white dwarfs, the mass required to trigger a TNR (see section 1.7.2)

is smaller than for lower-mass WDs. This partially results from the fact that more massive WDs have smaller radii, and in turn, larger surface gravity, thus requiring a smaller amount of mass to achieve the critical pressure at the base of the envelope, $P_{crit} \sim 10^{20}$ dyn cm^{-2}, needed to power a nova outburst (Shara 1981; Fujimoto 1982). The resulting explosions are characterized by larger ejection velocities and peak luminosities.

The high mass-accretion rates put constrains on the nature of the stellar companion, demanding a more evolved star. For instance, in U Scorpii a Roche lobe overflowing subgiant star has been observed, while in RS Ophiuchi mass transfer is the result of a strong stellar wind from a red giant companion (Darnley 2021).

Observations, as well as simulations, suggest that in RNe the mass of the WD increases (that is, not all the matter accreted by the WD is ejected during the outburst). Accordingly, these systems are likely type Ia supernova progenitors[8] (see, e.g. Kahabka *et al.* 1999; Anupama & Dewangan 2000; Hachisu & Kato 2001).

Compared to CN systems, RNe exhibit a wider range of orbital periods, ranging from a few hours to several hundred days. Given this disparity, Anupama (2008) subdivided the RN systems into three main groups:

- RS Oph/T CrB:
  This group is characterized by long orbital periods, of approximately a year, and red giant secondary stars. Their outbursts show fast declines from maxima, and are characterized by smaller ejected masses (by, at least, two orders of magnitude) with larger velocities ($\gtrsim$ 4000 km s^{-1}) than CNe.

- U Sco:
  The orbital periods in this group resemble those observed in CNe (ranging from hours to a day). They show evolved main sequence or subgiant companions. They also exhibit similar ejected masses than the RS Oph group, with similar extreme velocities (up to 10 000 km s^{-1}). This group hosts the fastest declining novae.

- T Pyx:
  This group has shorter orbital periods, ranging approximately between 1 and 3 hours. Their ejecta are characterized by similar velocities than those reported for CNe, with ejected masses $\gtrsim 10^{-5}$ M$_\odot$. It has been suggested that the mass of the WD component is lower than for the other two groups (Chomiuk *et al.* 2014). Among the different RNe that form this group, one can find fast and slow novae.

In this Thesis, we focused on the U Sco group (in particular, on U Sco itself, which has been observed in outburst, at least 8 times, the last one in 2022. The outburst detected in 2010 had an exceptional observational coverage, see, e.g, Schaefer *et al.* 2011; Mason *et al.* 2012; Pagnotta *et al.* 2015).

1.5 The nova light curve

Observationally, all nova eruptions tend to follow a characteristic light curve, shown in Fig. 1.3. Although the majority of novae have been found already during its rise in visual luminosity, observations at different wavelengths are crucial to piece together the physics

[8] Unfortunately, recent observations are not clear in this regard (see Pagnotta *et al.* 2015, for a work that exposes the difficulty to determine whether the white dwarf of U Sco loses or gains mass).

behind such events. The Figure, not to scale, illustrates the spectral evolution at different wavelengths as well as the different stages of the outburst as a function of time for very fast (U Scorpii), fast (V1974 Cygni), moderately fast (V705 Cassiopeiae) and slow (V992 Scorpii) novae.

1.5.1 Initial and final rise to maximum

Once the TNR sets in, the envelope expands. The initial expansion of this optically-thick shell (the "fireball" stage), first detected in X-rays by König *et al.* (2022), is characterized by a rapid rise in the visual luminosity. Depending on the mass and velocity of the ejected material, this stage can last from a few hours up to 3 days until it reaches a plateau (pre-maximum halt). Therefore, observations during this stage are scarce, and only a few novae (classical and recurrent) have been caught (e.g. OS And, V723 Cas, V1974 Cyg, and LMC 1991, U Sco 2010). The current study focuses on this stage by modeling the initial expansion stages of the ejecta, when the ejected layers from the WD collide with the accretion disk and at later times with the companion star.

At the pre-maximum halt, when the ejecta had expanded enough for the density to drop and the effective temperature to reach $\backsimeq 10^4$ K, the ions start to recombine with the electrons, increasing the ultraviolet opacity. This takes place at a constant bolometric luminosity and marks the beginning of the "iron curtain" (Shore 2002). The absorbed UV energy is then reemitted at larger wavelengths (in the optical and infrared).

During the final rise to optical maximum, the "iron curtain" thickens and the UV absorption maximizes. This occurs in a day or two for fast novae, while slow novae can spend several weeks until the visual peak is reached.

1.5.2 Early decline

As expansion proceeds, the density decreases and with it, the "iron curtain" starts to lift. After a decrease of 2 to 3 magnitudes in the visible, the ultraviolet spectra begins to show strong emission lines, which indicates that the nova is entering the prenebular stage. The time it takes for a nova to drop 2 (t_2) or 3 (t_3) magnitudes from maximum brightness establishes its "speed class", that is, whether it is a fast or a slow nova. This distinction is tied to the peak magnitude and the velocity of the ejecta. Fast novae are characterized by larger ejection velocities as well as larger peak magnitudes (reaching super-Eddington luminosities; Warner 2008) than slow novae. In fact, speed classes range from: very fast (t_2 $<$ 10 days) and fast ($t_2 \sim$ 11 - 25 days) to slow ($t_2 \sim$ 81 - 150 days) and very slow ($t_2 \sim$ 151 - 250 days) (Payne-Gaposchkin 1957). Some examples are the very fast nova U Scorpii, which had $t_2 \sim$ 2 days, the fast V1974 Cyg with $t_2 \sim$ 16 days, the moderately fast V705 Cas with $t_2 \sim$ 33 days and the slow nova V992 Sco with $t_2 \sim$ 100 days.

1.5.3 Transition phase

The subsequent decrease by nearly 3.5 magnitudes from the visual maximum indicates the beginning of a new stage, the transition phase, in which emission in the infrared rises, reflecting dust formation (Gehrz 1988). While CO novae are considered to be "prolific dust producers", observations of ONe novae seem to suggest that in these systems the condensation of matter into dust is not as abundant (resulting from the lower amount of matter being ejected, together with its higher velocities and lower densities). Dust condensed in

some ancient novae has been linked to the origin of a handful of presolar grains isolated from meteorites (Amari *et al.* 2001; Amari 2002).

At this stage, three different patterns are observed in the visual part of the spectra, as seen in Fig. 1.3: while fast novae generally cross this stage with no big changes, slower novae experience amplitude fluctuations of the order of 1-1.5 mag, with periods of nearly 5 up to 15 days. Some exceptional cases have experienced a drop of 7-10 magnitudes, that last for a few months (and in some cases, even years).

1.5.4 Final decline

After the transition phase, there is a continuous decrease in the visual luminosity until mass loss has ceased and the WD has been uncovered, reaching the pre-nova values. At this stage, X-ray emission takes over reaching its highest values. Observations in this band allow to infer estimates of the WD mass. In addition, once the expanding ejecta becomes optically thin, the nature of the underlying WD (CO or ONe) can be revealed spectroscopically.

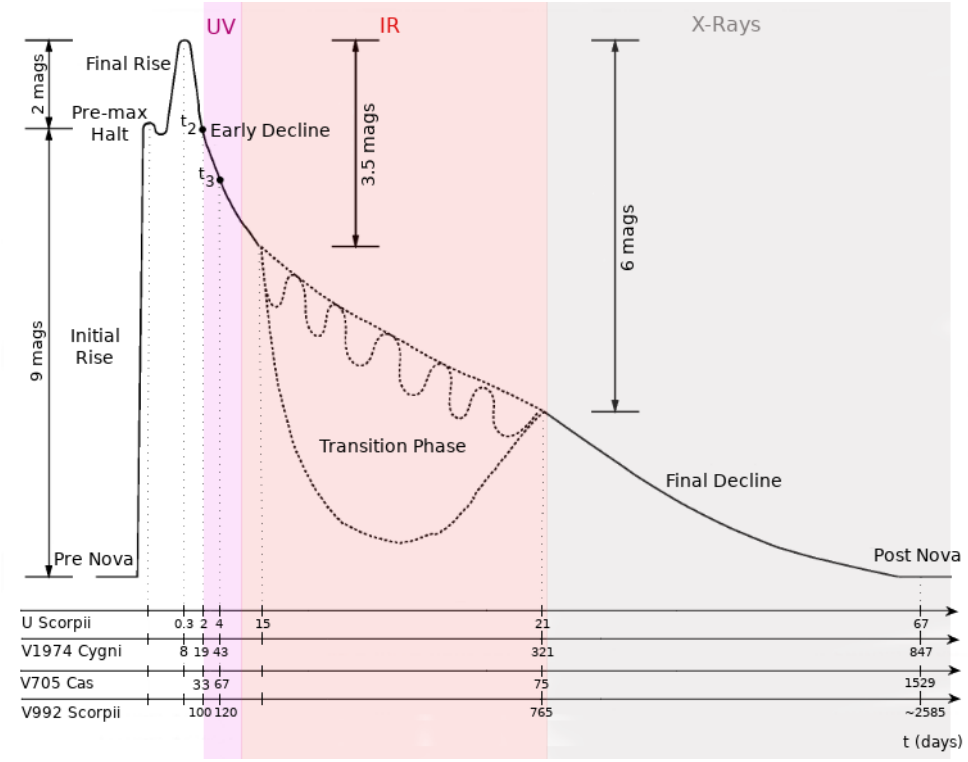

Figure 1.3: Morphology of a nova outburst. Figure adapted from Bode & Evans (1989) and O'Brien & Bode (2008). The spectral evolution of the different stages of the outburst as a function of time for very fast (U Scorpii), fast (V1974 Cygni), moderately fast (V705 Cassiopeiae) and slow novae (V992 Scorpii) are also shown. The shaded regions indicate the peak for ultraviolet (UV), infrared (IR) and X-rays wavelengths. The Figure is not to scale.

1.6 Spectroscopy

Understanding the spectra of classical or recurrent novae enables us to obtain information not only on the physical conditions of the emitting gas but also on the characteristics and nature of the system. And although each novae has its own signature, there are common features during the different stages of the nova outburst.

1.6.1 Spectroscopic stages

These spectroscopic stages, defined by McLaughlin (1944) and Payne-Gaposchkin (1957), are grouped by different epochs of the outburst:

- **The Pre-maximum spectrum**: Emerges through the initial rise and can last for a day or two after the optical peak. During the expansion of this optically-thick ejecta, the spectrum is characterized by strong and blue-shifted absorption lines.

- **Principal spectrum:** Coexists briefly with the pre-maximum spectrum, as it appears close to visual maximum. At the optical peak strong absorption lines are seen, resembling A-F supergiants with enhanced CNO lines. These absorption lines reveal larger velocities when comparing with the pre-maximum phase and are correlated with the speed class. And at this moment or immediately after, an emission-line component appears, being the strongest lines due to H, Ca II, Na II, Fe II, N, He and O.

- **Diffuse enhanced spectrum:** Starts to appear in the early decline stage of the light curve, while the principal spectrum is still strong. It is characterized by very strong and diffuse lines of hydrogen and ionized metals. This spectrum is displaced towards the violet around twice as that of the principal spectrum. And when the absorption reaches its maximum, the lines show P-Cygni profiles with broad emissions. Towards the end of this stage, the lines tend to split up into several components becoming narrower, then weaker and later disappear.

- **Orion system:** Rises when the diffuse enhanced system is at its maximum. The spectrum shows broad and diffuse absorption lines, and is characterized by He, O II, N II and in some cases H, with velocities similar or larger than that of the diffuse enhanced spectrum. The excitation and ionization levels increase at this stage.

  When this absorption system reaches its maximum, N III starts to appear. And as the absorption component disappears, the emission line component strengthens. The absorption systems cease when the transition phase is reached.

- **Nebular spectrum:** Is the final stage of the eruption, before reaching the post nova phase. The spectrum exhibits high ionization lines such as the auroral, nebular forbidden lines ([O III] lines) and high excitation coronal lines.

- **Post-nova:** At this stage, the ejecta clears and the contributors to the emission lines are now the companion, the disk and the white dwarf.

1.6.2 Spectral classification

By analyzing the optical spectra (at wavelengths 3500-7500 Å) after the outburst, Williams (1992) was able to find a pattern based on the strongest non-Balmer lines. He claims that the characteristics of the emission lines during the first few days after visual maximum, are correlated with their evolution thereafter. Moreover, he divided novae novae in two main groups: the "Fe II" and the "Ne/N" types. A survey on M31 novae, performed by Shafter *et al.* (2011) showed that nearly 85% of novae in M31 can be classified as "Fe II"-type, while the remaining 15% were considered to belong to the "He/N" class. They also found a particular novae (LMC 1988 No. 2) that showed both classes of spectra. These kind of novae are called "hybrid".

The characteristics of these three groups can be summarized as follows:

- Fe II:
  In this class the strongest non-Balmer lines are due to Fe II. The spectra is characterized by pronounced P Cygni absorption and narrow emission lines with velocities not exceeding 2500 km s^{-1}. Another feature that characterizes this class are the low ionization transitions during the first phases of the spectra.

  In the nebular phase of the spectra, forbidden lines start to appear. At the beginning of this phase low ionization auroral lines are detected, such as [N II] λ5755, [O II] λ7325, [O III] λ4363, and [OI] λ6300. It has a slow spectral evolution, over timescales of weeks and this class is generally associated with moderately fast to slow novae. Examples of such spectra can be seen on Figure 1.4.

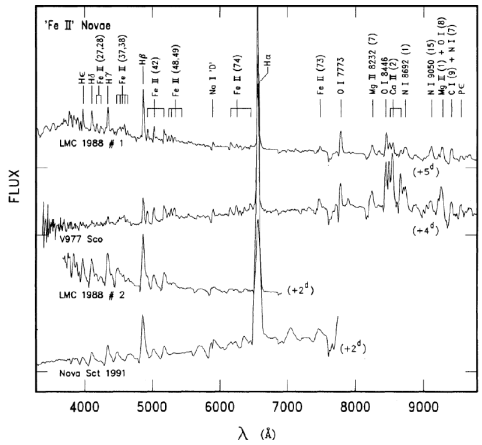

Figure 1.4: Example of the "Fe II" spectral nova class (Figure taken from Williams 1992).

- He/N:
  In this class the strongest non-Balmer lines are due to helium (He I/ He II) or nitrogen (N II/ N III). In contrast to the "Fe" class, this class exhibits higher ionization, broad emission lines with velocities larger than 2500 km s^{-1}, and rectangular profiles, while P-Cygni absorptions are either weak or absent.

  The nebular phase spectrum in this case is not as straightforward as in the "Fe" class. In some "He/Ne" novae no forbidden lines are observed, while in others high excitation

coronal lines are seen. This class is generally associated with very fast to fast novae, with a very rapid spectral evolution over timescales of days.

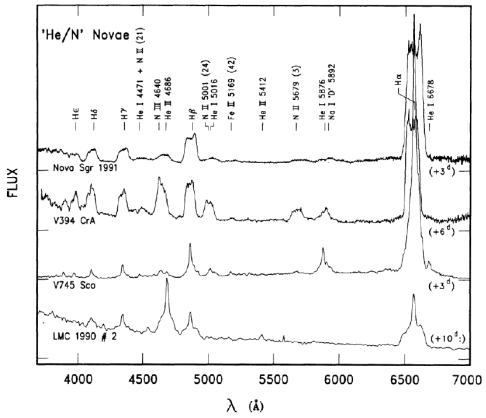

Figure 1.5: Example of the "He/N II" spectral nova class (Figure taken from Williams 1992).

- Hybrid:
  This class includes all novae that switch between both spectral classes during the early permitted line phase and prior to the arrival of the forbidden lines. An example of such spectra can be seen in Figure 1.6.

  Williams (2012) argues that all novae are "hybrid" and that the "Fe" and "He/N" classes do not correspond to different novae, but instead refer to different locations within the system. Specifically, he claimed that the "He/N" class reflects the spectra originated from the WD ejecta, while the "Fe" class spectra would originate from the secondary star.

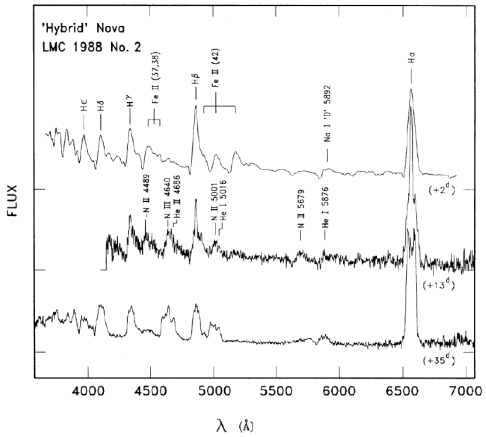

Figure 1.6: Example of a "hybrid" spectral nova class (Figure taken from Williams 1992).

1.7 The long-term evolution of classical and recurrent novae

Most of the efforts undertaken in the modeling of classical and recurrent novae have focused on the early stages of the explosion and ejection (see Starrfield *et al.* 2008, 2016; José & Shore 2008; José 2016, for recent reviews). Therefore, important aspects of the evolution of these systems, associated with the interaction of the ejecta, first with the accretion disk that orbits the white dwarf, and ultimately with the secondary star, have been largely unexplored. In fact, shortly after the outer layers of the white dwarf expand and achieve escape velocity, a fraction of the ejected material is expected to collide with the secondary star. As a result, part of the nova ejecta is expected to mix with the outermost layers of the secondary. The resulting chemical contamination may have potential implications for the next nova cycle, once mass transfer from the secondary resumes.

In this section, we will focus on the formation of the accretion disk orbiting the WD, and on the expansion and ejection of the matter transferred from the disk and piled up on top of the WD (Frank *et al.* 2002; Warner 2009; Eggleton 2006).

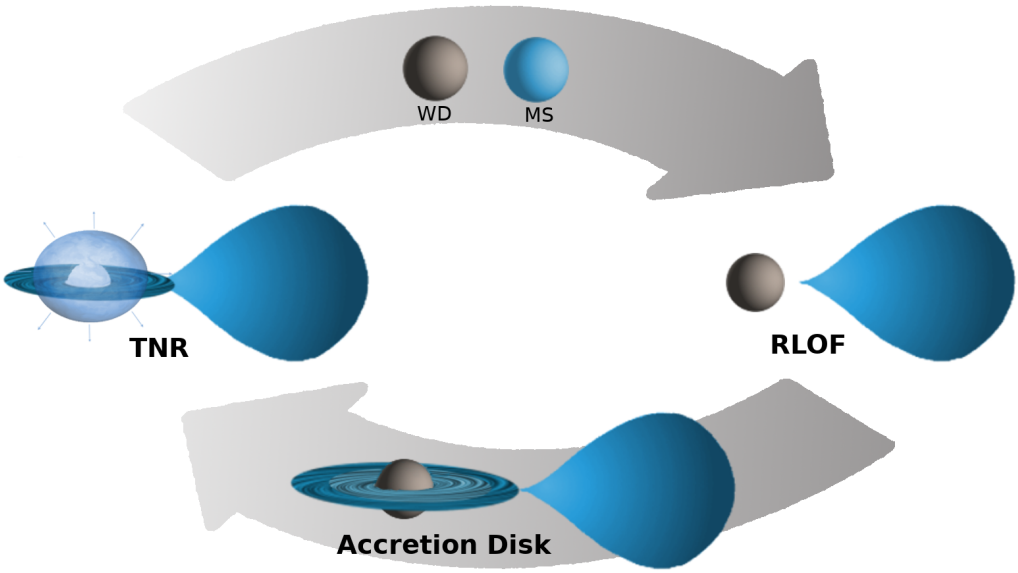

Figure 1.7: Schematic representation of the evolution of a nova system (not to scale).

1.7.1 The accretion disk

CN and RN are composed of a WD and a companion star that can be a MS or a more evolved one, depending on the orbital period. Observations, together with simulations, allow us to distinguish different stages prior to the outburst (see upper, right and lower panels in Fig. 1.7), starting with the aforementioned close binary system composed of a low-mass MS and a WD (upper panel): as stellar evolution proceeds, the secondary will eventually fill its

Roche Lobe[9] (right panel) and consequently hydrogen-rich matter from the companion star can be transferred via the L1 point towards the compact primary. During this process, and considering the high specific angular momentum of the material that is being transferred, the WD is not able to accrete this material directly and instead, in this conservative mass transfer episode, forces the incoming stream to orbit the primary. And due to conservation of angular momentum, this matter will form a ring that revolves around the WD (lower panel).

This ring will spread both inwards and outwards forming the accretion disk. This mechanism can be explained by considering viscous dissipation processes such as shocks, which convert the orbital kinetic energy of the gas into heat, increasing its temperature. Part of this heat will eventually be radiated away, forcing matter to approach the primary by moving to smaller orbits. This entails the loss of angular momentum, only possible if matter is transferred outwards since the total angular momentum of the disk is conserved. Therefore, the initial ring expands to larger radii, where its tidal interactions with the companion are responsible for transporting it back to the orbital motion. This tidal radius, R_d, can be approximated by:

$$R_d \cong 0.9 R_{L1} \tag{1.2}$$

where R_{L1} is the Roche lobe radius of the primary (see Frank *et al.* 2002, for more details). The inner expansion ceases at the surface of the WD.

1.7.2 The outburst

In CN systems, the matter transferred to the primary WD is accreted from the disk at a rate of approximately 10^{-10} to 10^{-8} $M_\odot$ yr^{-1}. In RN, the mass-accretion rate is expected to reach 10^{-7} - 10^{-6} $M_\odot$ yr^{-1} (see, e.g. Hernanz & José 2008; Warner 2008, and references therein).

During this accretion process, matter accumulates on top of the WD. This envelope is gradually compressed reaching high densities, and as a result it becomes mildly (electron) degenerate. This compression, forces the temperature to rise and nuclear fusion to occur. This, in principle, would lead to the expansion of the envelope, but in a degenerate gas, pressure does not depend on the temperature and no expansion occurs. Therefore, the temperature keeps rising, increasing the energy release from nuclear reactions, which in turn, forces the temperature to climb towards higher values resulting in further nuclear fusion and energy release. This continuous cycle, called thermonuclear runaway (TNR)(see Fig. 1.7 left panel) lasts for a few minutes ($\sim$ 100 seconds) and ends once high enough temperatures have been reached, lifting the degeneracy and enabling the envelope to expand - i.e., the outburst.

During the early accretion stage, when temperatures are of the order of $\lesssim 10^7$ K, the accreted hydrogen burns via proton-proton chains. As the temperature increases, the cold CNO cycle takes over triggering the TNR, which in turn, speeds up the temperature escalation ($\gtrsim 10^8$ K), giving way to the hot CNO cycle as the main driver of fusion reactions. During these stages, the energy released is boosted in such a manner that radiation becomes inefficient and as a result convection sets in, promoting mixing and preventing reactions from reaching equilibrium, since the nuclear abundances keep changing. In addition, convection brings some short-lived β^+-unstable nuclei (^{13}N, ^{14}O, ^{15}O, ^{17}F) from deeper regions in the envelope towards its outer cooler layers. Due to its lower temperatures, such isotopes decay,

[9]For CN, the RLOF happens when the star is still on the MS phase, while for RN, when the companion star is at the subgiant or even at the red giant branch, depending on the orbital separation.

rather than being destroyed, releasing 10^{13} up to 10^{15} erg g^{-1} s^{-1}. Degeneracy is lifted when the temperature at the base of the envelope reaches just 3×10^7 K, so very early in the TNR. A fraction of this energy drives the expansion and ultimate ejection of the envelope, which is no longer degenerate (Starrfield *et al.* 1972).

Sparks *et al.* (1978) were able to reproduce the main characteristics of slow novae by considering solar abundances for the WD envelope prior to the outburst. For fast novae, on the other hand, a CNO enhancement was required to achieve the observed abundances (Starrfield *et al.* 1972; MacDonald 1983). Thus, for these cases, it was insufficient to consider that the material synthesised during these episodes proceeded from the MS companion alone (that has solar abundances, Z = 0.02). A workaround, that is currently expected and accepted, is to consider that during these events mixing occurs at the contact region between the WD core and the accreted envelope, before the TNR starts (see for example Prialnik & Kovetz 1984; Alexakis *et al.* 2004) or triggered by the TNR itself (see for example Glasner *et al.* 2007; Casanova *et al.* 2011).

Though the exact mechanism of this mixing is still a matter of debate, it is presumed that the CO- or ONe-WD supplies ^{12}C from its outer layers into the above mentioned envelope[10]. In fact, Casanova *et al.* (2011) showed that once convection sets in and due to Kelvin-Helmholtz instabilities, vortexes are formed, penetrating deeply into the core-envelope interface and bringing material from the core to the envelope, providing the enrichment and the dispersion of abundances observed in the ejecta. These ejected layers have typical velocities of $\sim 10^3$ and $\sim 10^4$ km s^{-1}, with predicted ejected masses of $\sim 10^{-5}$ to 10^{-4} M$_\odot$ and $\sim 10^{-7}$ to 10^{-6} M$_\odot$ for CN and RN, respectively.

1.7.3 The following outburst

This energetic outburst does not disrupt the white dwarf and once sufficient mass has been accumulated, the previously described process resumes (see Fig. 1.7). The time required to power the next eruption can take several months (as for a RN) to thousands of years (as for a CN). An important aspect of the evolution of such systems is the reestablishment of the accretion disk, which will provide the needed fuel for the outburst to recur. Although we are not aware of any theoretical study on this matter, there are two known systems, namely RS Oph and U Sco, in which reformation of the accretion disks has been observed.

The reestablishment of the disk was first observed in RS Oph. Shafter & Misselt (2006) observed a dip in the brightness with respect to the quiescent state, which indicated that the accretion disk was not fully contributing to the total luminosity of the system. The timescale for the reformation of the accretion disk was estimated to be approximately half a year, inferred from the onset of the quiescent brightness and the characteristic flickering observed when an accretion disk is fully formed.

More recently, Schaefer *et al.* (2011) were able to monitor the reestablishment of the accretion disk in U Sco in great detail. Once the ejecta became sufficiently transparent, which happened on day 15, the accretion stream was already visible, meaning that mass transfer had already resumed. For the next days, while the accretion disk was being built, the above mentioned "optical dips" were observed, disappearing by day 61, which is at odds with the expected timescale, of the order of decades, for the re-formation of the accretion

[10]Note that an ONe-WD has a CO "shield" surrounding the ONe core (García-Berro *et al.* 1997). Therefore for such WDs the matter dredged-up into the envelope does not correspond to ONe-rich material (see José *et al.* 2003, for a study of the impact of such CO-rich shields on the classification of classical novae).

disk. A possibility was offered by Corradi *et al.* (2003), who suggested that for non-magnetic systems, as these ones, the accretion disk survives, being disrupted only in IP systems.

1.8 Open questions

Despite the extraordinary achievements made in the past decades, there are still open questions in the physics of classical and recurrent novae that require an answer to. As more powerful telescopes are being built, more surveys being carried, and fastest computers being used, we can seek for a more complete picture of the physics behind the evolution of these stellar explosions.

CNe and RNe are of great astrophysical interest. Being the type of binary systems that can be observed without much difficulty, they also act as live tools that help to understand and increase our knowledge in hydrodynamics, nuclear physics, propagation of shock waves, or the properties of white dwarf stars. The study of the long-term evolution of CNe and RNe is of paramount importance, since a number of physical phenomena linked to those systems occur at typical timescales for which interaction between the ejecta, the accretion disk and the secondary star is expected.

Novae are prolific dust producers and they are considered to be real-time laboratories to study dust formation (Evans & Rawlings 2008; Gehrz 2008). Infrared (Evans & Rawlings 2008; Gehrz *et al.* 1998; Gehrz 2008) and ultraviolet observations (Shore *et al.* 1994) have unambiguously revealed dust forming episodes in the ejected shells accompanying some nova outbursts ~ 100 days after the explosion. In fact, it has been suggested that novae may have contributed to the inventory of presolar grains isolated from meteorites. A major breakthrough in the identification of nova candidate grains was achieved by Amari *et al.* (2001); Amari (2002); these authors reported several SiC and graphite grains, which were isolated from the Murchison and Acfer 094 meteorites and had abundance patterns qualitatively similar to those predicted by models of nova outbursts: low $^{12}C/^{13}C$ and $^{14}N/^{15}N$ ratios, high $^{30}Si/^{28}Si$ and close-to-solar $^{29}Si/^{28}Si$ ratios, and high $^{26}Al/^{27}Al$ and $^{22}Ne/^{20}Ne$ ratios[11]. However, to quantitatively match the grain data of the Amari sample, mixing between material synthesized in the explosion and more than ten times as much unprocessed, isotopically close-to-solar material was required. The collision of the ejecta, either with the accretion disk or with the secondary star, may naturally provide the required chemical dilution to explain the reported grain data.

Moreover, the unexpected discovery of very high-energy emission (> 100 MeV) recently observed in a number of novae by the Large Area Telescope, on board the Fermi γ-ray space observatory (Fermi LAT), has confirmed novae as a distinct class of γ-ray sources (Ackermann *et al.* 2014). In symbiotic binary systems, such as V407 Cyg, this high-energy emission has been attributed to shock acceleration in the ejected shells after interaction with the dense wind of the red giant companion. The emission reported from several classical novae involving less evolved stellar companions (e.g., V1324 Sco, V959 Mon, V339 Del, V1369 Cen), however, has been attributed to internal shocks in the ejecta. In this scenario, gamma-rays are produced either through a hadronic process, in which accelerated protons collide with matter to create neutral pions that decay into γ-ray photons, or through a leptonic process, in which visible or infrared photons reach high energies in the interaction with high-energy electrons. While the hadronic process seems to be favored, the exact nature

[11] See also Iliadis *et al.* (2018); Haenecour *et al.* (2019), for additional studies on putative nova grains.

of the mechanism responsable for gamma-ray production remains unknown[12].

The abovementioned aspects stress the need for a thorough description of the dynamics of the system after a nova explosion, following the collision of the ejecta with the accretion disk, and subsequently, with the secondary star. The present Thesis aims at filling this gap. This Thesis is organized as follows: in Chapter 2 a detailed account of `GADGET-2`, the SPH code used to perform the simulations presented in this Thesis, is given. In addition, we present the methodology adopted to compute the initial configuration of the stellar binary systems used in this Thesis. In Chapter 3, we test the influence of the different parameters (i.e., mass and velocity of the ejecta, mass and geometry of the accretion disk) on the dynamical and chemical properties of a classical nova system, through a suite of three-dimensional, SPH simulations of the interaction between the nova ejecta, accretion disk, and stellar companion. The methodology used in Chapter 3, supplemented by the implementation of rotational effects (Coriolis and centrifugal forces), is applied to a specific recurrent nova, U Scorpii in Chapter 4. In Chapter 5 a sensitivity study, aimed at testing different configurations of the system (i.e., different masses for the white dwarf, orbital separations, properties of the ejecta) is presented. Finally, the main conclusions of this work, together with a list of ideas for future work, are summarized in Chapter 6.

[12]Diffusive shock acceleration of electrons and protons, with a maximum energy of a few TeV, was predicted by Tatischeff & Hernanz (2007) in the framework of the 2006 outburst of the recurrent nova RS Ophiuchi. See also Shore *et al.* (2013) for an explanation of the origin of X-ray emission in Nova Mon 2012 based on internal shocks driven by the collision of filaments that freeze out during expansion.

Chapter 2

Numerical method

Spectroscopic and photometric studies of classical and recurrent novae have provided crucial information regarding the nature and evolution of such systems. Numerical simulations, in turn, have provided a complementary viewpoint to explore the physical conditions that power nova outbursts.

2.1 Types of codes

From a physical viewpoint, novae (and stars in general) can be described by the set of conservation equations of fluid dynamics (i.e., mass, energy and momentum conservation), energy transport (by radiation, conduction and/or convection), energy production and losses (nuclear reactions, neutrinos), supplemented by additional relations that account for the thermodynamic state of the fluid (i.e., equation of state, opacity...). There are two main approaches to perform numerical simulations on such systems: the Eulerian and the Lagrangian formulations. In the Eulerian approach a fluid element is described with respect to an "external" reference frame that is fixed in space. While in the Lagrangian one, a fluid element is at rest with respect to the reference frame (i.e., the reference frame is "attached" to the fluid). Both approaches have been used in numerical simulations with each exhibiting advantages and drawbacks. One way to implement these approaches is by making use of a mesh or grid, which means that the continuous properties of the fluid are discretized in space. In an Eulerian grid method the main setback is tied to expansive flows. That is, by making use of a fixed grid this method cannot account for fluids that expand outside the computational domain. While in Lagrangian grid methods the difficulty arises when dealing with shear or turbulent flows as it can cause large grid deformations, which most likely induces the system to crash.

There are alternative methods where the grid is entirely removed such as smoothed particle hydrodynamics (hereafter SPH). In purely Lagrangian SPH methods, the continuous properties of the fluid are discretized in mass. And as a consequence the resolution of such method follows mass instead of volume as in the abovementioned techniques, allowing for large deformations and complex geometries in fluids; in addition the fluid is not confined as in grid-based methods thus expansive flows can be easily tracked.

We are interested in following the evolution of the material that is ejected from the WD as a result of a nova outburst and its interaction with the accretion disk and the stellar

companion. Given the density contrasts and the dynamic ranges faced in these systems, SPH is better suited with respect to a grid based method.

The 3D-SPH code chosen to reach our goals is `GADGET-2` (Springel 2005; Springel *et al.* 2001), that being parallelized allows for high-resolution simulations. In this Chapter, an overview on SPH methods is provided, with particular emphasis on `GADGET-2`.

2.2 `GADGET-2` - Smoothed Particle Hydrodynamics

2.2.1 The basics

Smoothed Particle Hydrodynamics (SPH) is a mesh-free method first introduced by Lucy (1977) and independently by Gingold & Monaghan (1977). In essence, this method approximates the continuum properties and dynamics of a fluid by means of interpolation points or sets of discrete elements called particles. Hereafter, we will restrict to Lagrangian SPH methods (see Lind & Stansby 2016; Fourtakas *et al.* 2018, for examples of Eulerian and Eulerian-Lagrangian SPH formulations).

To understand how SPH methods work, we follow Monaghan (1992), Price (2005), Price (2012) and Rosswog (2015).

Let's start by considering the following spatial quantity, $A(\mathbf{r})$:

$$A(\mathbf{r}) = \int_V A(\mathbf{r}')\delta(|\mathbf{r} - \mathbf{r}'|)d\mathbf{r}', \tag{2.1}$$

where δ is the Dirac delta function. Such function can be replaced by a normalized smoothing kernel (W), as long as this kernel becomes the delta function as its "size" or width h, called the smoothing length, tends to zero:

$$\lim_{h\to 0} W(|\mathbf{r} - \mathbf{r}', h|) = \delta(\mathbf{r} - \mathbf{r}'), \tag{2.2}$$

A more detailed description on both the kernel and the smoothing length will be given in Sects. 2.2.1.1 and 2.2.1.2, respectively.

Taking into account equation 2.2, equation 2.1 becomes:

$$A(\mathbf{r}) = \int_V A(\mathbf{r}')W(|\mathbf{r} - \mathbf{r}', h|)d\mathbf{r}', \tag{2.3}$$

To move from this continuous representation of the properties of the fluid towards a Lagrangian discretization, the integral must be replaced by a summation, in the form:

$$A(\mathbf{r}) = \sum_{j=1}^{N} \frac{m_j}{\rho_j} A_j W(|\mathbf{r} - \mathbf{r}_j, h|), \tag{2.4}$$

where the continuous properties of the fluid at a particular point (in this case $A(\mathbf{r})$) can now be obtained via kernel interpolation and summation over all the N-neighboring particles (j) (see section 2.2.1.2 for a more detailed description) of particle i. The term $\frac{m_j}{\rho_j}$ corresponds to the discretized volume element $d\mathbf{r}'$ showed in equation 2.1.

The first derivative of a spatial quantity, can be written as:

$$\nabla A_i = \sum_{j=1}^{N} \frac{m_j}{\rho_j} A_j \nabla_i W_{ij}. \tag{2.5}$$

with $W_{ij} = W(|\mathbf{r}_i - \mathbf{r}_j, h|)$.

Alternatively, the derivative can also be computed by considering the following identity:

$$\rho \nabla A = \nabla(\rho A) - A \nabla \rho \tag{2.6}$$

and by taking into account the kernel estimation of the two terms on the right-hand side independently, yields:

$$\nabla_i A_i = \frac{1}{\rho_i} \sum_{j=1}^{N} m_j (A_i - A_j) \nabla_i W_{ij}, \tag{2.7}$$

This formulation ensures that the derivative vanishes if A is constant.

Similarly, the divergence and curl of vector quantities can be written as:

$$\nabla_i \cdot \mathbf{A}_i = -\frac{1}{\rho_i} \sum_j m_j \mathbf{A}_{ij} \cdot \nabla_i W_{ij} \tag{2.8}$$

and

$$\nabla_i \times \mathbf{A}_i = -\frac{1}{\rho_i} \sum_j m_j \mathbf{A}_{ij} \times \nabla_i W_{ij} \tag{2.9}$$

respectively, where $\mathbf{A}_{ij} = (A_i - A_j)$.

The reason behind the use of such formulation in SPH is that it ensures symmetry between pairs of particles imposing momentum conservation.

2.2.1.1 Kernel

As mentioned above, to compute the SPH equations a weight function or smoothing kernel is needed, through which the continuum properties of the flow are obtained from a discrete sample of N particles. Thus, to properly describe the fluid, a few conditions for the kernel are required:

1. It must be normalized to 1:

$$\int_V W(\mathbf{r}, h) dV = 1, \tag{2.10}$$

2. It must become the delta function as its smoothing length tends to zero (see equation 2.2)

3. It is desirable for the kernel to be spherically symmetric; this way the kernel depends only on the particle separation and not on the particle position

4. It must be at least second-order differentiable

With these conditions in mind, a typical form for a kernel is:

$$W(r,h) = \frac{1}{Ch^d} f(r), \tag{2.11}$$

where C is a normalization constant, h the smoothing length, d the number of dimensions and $f(r)$ a function that describes the shape of the kernel.

Gingold & Monaghan (1977) used a Gaussian kernel, which fulfills the conditions mentioned above and in a three dimensional space reads as:

$$W(r,h) = \frac{1}{(\pi\sqrt{\pi})h^3} exp\left(-\frac{r^2}{h^2}\right) \tag{2.12}$$

This choice for the kernel, despite having a spatial derivative that is infinitely differentiable and as a result provides accurate density estimations, is extremely expensive as it never vanishes and thus the summations are made over all the particles in the system, meaning that the computational cost scales as O(N). By bounding the kernel, taking into account that the contribution from distant particles becomes unimportant, the numerical computation becomes considerably more efficient scaling as $O(n_j N)$.

There are different kernel families such as Sinc kernels (Cabezón *et al.* 2008), Wendland kernels (Wendland 1995)[1] or the B-spline ones (Schoenberg 1946a,b). In the current study the latter family is used. These "Bell-shaped" kernels (see Figure 2.1) can be truncated at different radii. For a cubic spline kernel, it vanishes at $2h$, while for a quintic it vanishes at $3h$. By increasing the compact support region, as in the latter ones, the smoothness of the kernel and the accuracy of the density estimate are also increased. However it also means that a larger number of neighbors is needed (see subsection 2.2.1.2), and accordingly, the computational cost rises. The simplest and widely used kernels in SPH codes are the cubic spline kernels, which meet all the above requirements. Nonetheless it is worth mentioning that these cubic kernels exhibit discontinuities at higher-order derivatives. Thus, the choice of the kernel depends on the study in hand. For the simulations presented in this Thesis, cubic spline kernels are accurate enough as high-order derivatives have not been used.

Indeed, `GADGET-2` uses a cubic spline kernel (truncated at 2h) in the form:

$$W(r,h) = \frac{8}{\pi h^3} \begin{cases} 1 - 6(\frac{r}{h})^2 + 6(\frac{r}{h})^3, & 0 \leqslant \frac{r}{h} \leqslant \frac{1}{2}, \\ 2(1 - \frac{r}{h})^3, & \frac{1}{2} < \frac{r}{h} \leqslant 1, \\ 0, & \frac{r}{h} > 1. \end{cases} \tag{2.13}$$

Note that in `GADGET-2` a different notation is used: the kernel vanishes at h and not at $2h$ as used by other authors.

2.2.1.2 Smoothing length

As noted before, the smoothing length h of an SPH particle defines the width or size of a kernel function. In practice, h defines the radius of interaction for each SPH particle as depicted in Figure 2.1. All the particles that lie within this radius (blue dots) are named neighbors and the area of their influence is shaped according to the kernel function, $W(r)$ (in this case, a "Bell-shaped" kernel). Thus, a physical quantity associated to particle i can be retrieved by summing the relevant properties of all the particles that lie within the range

[1] For a more extensive discussion see, for example, Price (2012) and Rosswog (2015).

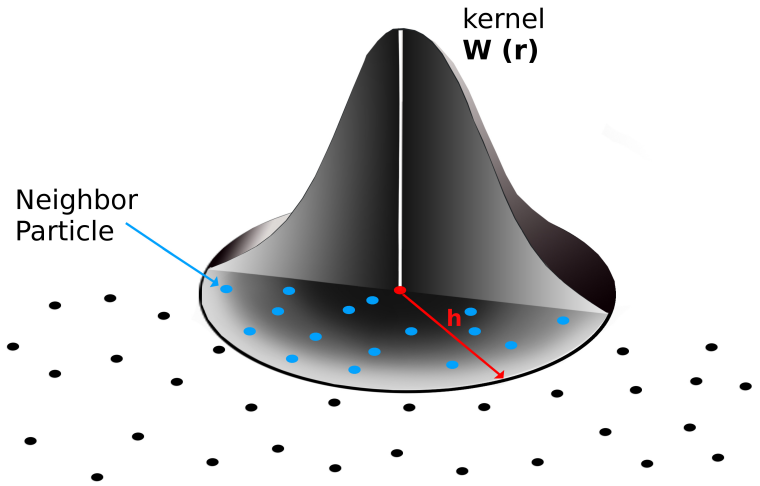

Figure 2.1: Illustration of a spline kernel W(r) and its smoothing length h, with the particle of interest in red and the neighboring particles in blue. The color gradient represents the importance of the neighbours.

of the kernel with the relative contribution of the neighbors reflected by the color gradient depicted in Figure 2.1. That is, the weight of the neighbors decreases as its distance from the particle of interest i (colored in red) increases.

Note that the number of neighbors needed to have a good density estimate depends on the used kernel, which for a cubic spline kernel ranges between 50 and 70. Since particles are not fixed in space, the neighbors will differ as particles move around from one place to another. As such, in SPH and in particular GADGET-2, the neighbors of a particle are found by making use of the so-called tree method, described in detail in section 2.2.4.1.

The pioneering SPH codes had a fixed smoothing length for all particles. This means, as illustrated in the upper panels of Figure 2.2, that both low (upper-left panel) and high (upper-right panel) density regions would have the same size for the kernel, thus leading to a poor resolution at low-density regions and a waste of computational resources at high-density regions. Thus a variable smoothing length (lower panels from Fig. 2.2), associated with each SPH particle and related to the local density, is essential to be able to perform simulations with high-density contrasts. This way, the smoothing length can be made larger in low-density regions (lower-left panel) and smaller in high-density regions (lower-right panel). There are different ways to implement variable smoothing lengths. The method used in GADGET-2 follows from Springel & Hernquist (2002), which relies on the local particle density. In other words, it considers the kernel volume of a particle to have a constant mass for the estimated density, which, for equal mass particles, reads as:

$$\frac{4\pi}{3} h_i^3 \rho_i = N_{sph} m, \tag{2.14}$$

where N_{sph} is the number of smoothing neighbors, and m the mass of each particle.

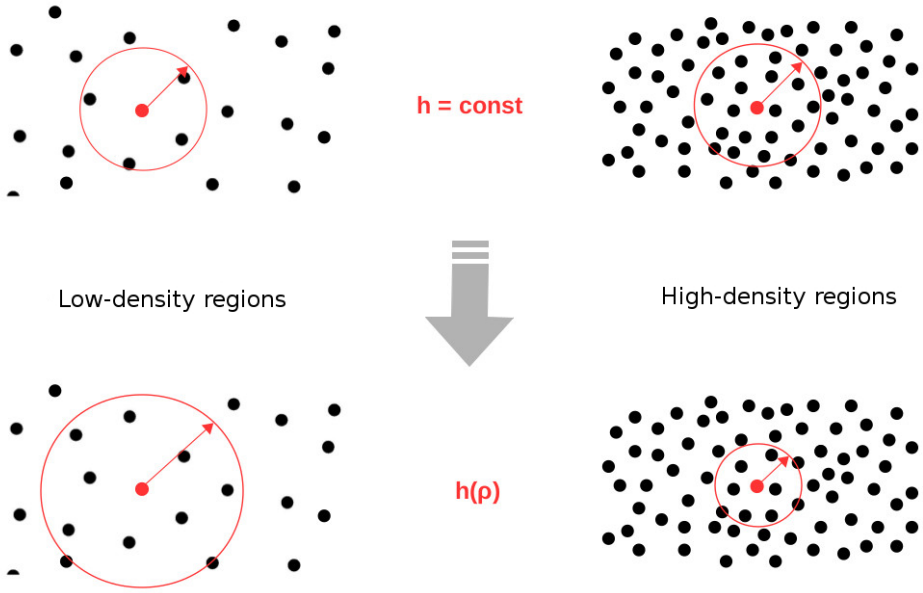

Figure 2.2: Schematic illustration of the importance of variable smoothing lengths, h. In the upper panels, a fixed smoothing length is considered for both low- and high-density regions. In the bottom panels, a variable smoothing length is considered: in low-density regions h increases, in high-density regions h decreases.

2.2.2 Euler equations for fluid dynamics

The physical conditions that characterize a stellar plasma can be described by a set of differential equations that include conservation of mass,

$$\frac{\mathrm{d}\rho}{\mathrm{d}t} = -\rho\nabla\cdot\vec{v}, \tag{2.15}$$

conservation of momentum:

$$\frac{\mathrm{d}\vec{v}}{\mathrm{d}t} = -\frac{\nabla P}{\rho}, \tag{2.16}$$

and conservation of energy:

$$\frac{\mathrm{d}u}{\mathrm{d}t} = -\frac{P}{\rho^2}\frac{\mathrm{d}\rho}{\mathrm{d}t}, \tag{2.17}$$

together with a suitable equation of state (EoS), which for an ideal gas with polytropic index γ is given by:

$$P = (\gamma-1)\rho u, \tag{2.18}$$

In Eqs. 2.15 - 2.18, ρ is the density, $\frac{\mathrm{d}}{\mathrm{d}t} = \frac{\partial}{\partial t} + \vec{v}\cdot\nabla$ the Lagrangian time derivative, $\vec{v}$ the fluid velocity, P the pressure and u the internal energy.

2.2.2.1 Continuity equation

In SPH, the density of a particle i is expressed as a function of the mass and the kernel (see equation 2.1), in the form:

$$\rho_i = \sum_{j=1}^{N} m_j W_{ij,h_i}. \tag{2.19}$$

Making use of equation 2.19 together with equation 2.7, the equation for mass conservation can be written as:

$$\frac{\mathrm{d}\rho_i}{\mathrm{d}t} = -\rho_i \sum_{j=1}^{N} \frac{m_j}{\rho_j} \mathbf{v}_{ij} \nabla_i W_{ij}, \tag{2.20}$$

As mentioned before, one can increase the spatial resolution by letting each particle to have its own associated smoothing length (also known as the "grad-h" formalism), which depends on the local conditions (Hernquist & Katz 1989; Benz 1990). In this framework, the density becomes a function of both the particle coordinates and the smoothing length, and the corresponding continuity equation can be written as:

$$\begin{aligned} \frac{\mathrm{d}\rho_i}{\mathrm{d}t} = \frac{\mathrm{d}}{\mathrm{d}t}\left[\sum_j^N m_j W_{ij}(h_i)\right] &= \sum_j^N m_b \left[\frac{\partial W_{ij}}{\partial \mathbf{r}_{ij}} \frac{\mathrm{d}\mathbf{r}_{ij}}{\mathrm{d}t} + \frac{\partial W_{ij}}{\partial h_i} \frac{\mathrm{d}h_i}{\mathrm{d}t}\right] \\ &= \sum_j^N m_b \mathbf{v}_{ij} \nabla_i W_{ij} + \frac{\mathrm{d}\rho_i}{\mathrm{d}t} \frac{\partial h_i}{\partial \rho_i} \frac{\partial}{\partial h_i} \left(\sum_j^N m_b W_{ij}\right) \end{aligned} \tag{2.21}$$

which, together with equations, 2.19 and 2.14, becomes:

$$\frac{\mathrm{d}\rho_i}{\mathrm{d}t}\left[1 - \frac{\partial h_i}{\partial \rho_i}\frac{\partial \rho_i}{\partial h_i}\right] = \sum_j^N m_b \mathbf{v}_{ij} \nabla_i W_{ij} \tag{2.22}$$

Or

$$\frac{\mathrm{d}\rho_i}{\mathrm{d}t} = \frac{1}{\Omega_i} \sum_j^N m_j \mathbf{v}_{ij} \nabla_i W_{ij} \tag{2.23}$$

with Ω_i being defined as:

$$\Omega_i = \left[1 + \frac{h_i}{3\rho_i}\frac{\partial \rho_i}{\partial h_i}\right] \tag{2.24}$$

for a three-dimensional space.

Note that the smoothing length is needed to calculate the density and likewise the density is needed in order to obtain the smoothing length. Thus, both h_i and ρ_i are obtained alongside, which in GADGET-2 is done with a Newton-Raphson iteration.

2.2.2.2 Momentum equation

Eckart (1960) showed that, for an inviscid ideal gas, the momentum and energy conservation relations could be obtained from the Lagrangian (L) :

$$L = \int \rho \left(\frac{\mathbf{v}}{2} - u \right) dV \tag{2.25}$$

where ρ is the density, $\mathbf{v}$ the velocity and u the internal energy.

By following Eckart and taking into account variable smoothing lengths, Springel & Hernquist (2002) derived these equations by discretizing the Lagrangian in terms of fluid elements, each with mass m_i:

$$L_{SPH} = \sum_j m_j \left(\frac{1}{2} \mathbf{v}_j - u_j \right) \tag{2.26}$$

The equation of motion can be derived from:

$$\frac{\mathrm{d}}{\mathrm{d}t} \frac{\partial L}{\partial \mathbf{v}_i} - \frac{\partial L}{\partial \mathbf{r}_i} = 0 \tag{2.27}$$

That is:

$$\frac{\partial L}{\partial \mathbf{v}_i} = m_i \mathbf{v}_i \qquad \text{and} \qquad \frac{\partial L}{\partial \mathbf{r}_i} = -\sum_j m_j \frac{\partial u_j}{\partial \rho_j} \frac{\partial \rho_j}{\partial \mathbf{r}_i}$$

And considering the first law of thermodynamics:

$$\frac{\partial u}{\partial \rho} = \frac{P}{\rho^2} \tag{2.28}$$

the equation of conservation of momentum (Eq. 2.16) becomes:

$$m_i \frac{\mathrm{d}\vec{v_i}}{\mathrm{d}t} = -\sum_{j=1}^{N} m_j \frac{P_j}{\rho_j^2} \frac{\partial \rho_j}{\partial \mathbf{r}_i} \tag{2.29}$$

Solving the spatial derivative of the density:

$$\begin{aligned} \frac{\partial \rho_j}{\partial \mathbf{r}_i} = \frac{\partial}{\partial \mathbf{r}_i} \left[\sum_k^N m_k W_{jk}(h_j) \right] &= \sum_k^N m_k \left[\frac{\partial W_{jk}}{\partial \mathbf{r}_{jk}} \frac{\partial \mathbf{r}_{jk}}{\partial \mathbf{r}_i} + \frac{\partial W_{jk}}{\partial h_j} \frac{\partial h_j}{\partial \mathbf{r}_i} \right] \\ &= \sum_k m_k \nabla_i W_{jk} + \frac{\partial \rho_j}{\partial \mathbf{r}_i} \frac{\partial h_j}{\partial \rho_j} \frac{\partial}{\partial h_j} \left(\sum_k m_k W_{jk} \right) \\ &= \frac{1}{\Omega_j} \sum_k m_k \nabla_i W_{jk} \end{aligned} \tag{2.30}$$

and using the following identities (see Rosswog 2009, for more details):

$$\nabla_i W_{jk} = \nabla_j W_{kj} (\delta_{ji} - \delta_{ki}) \qquad \text{and} \qquad \nabla_i W_{ij} = -\nabla_j W_{ij}$$

we get:

$$m_i \frac{\mathrm{d}\vec{v_i}}{\mathrm{d}t} = -\sum_j \sum_k m_j \frac{P_j}{\rho_j^2} \frac{1}{\Omega_j} m_k \nabla_j W_{jk} \left(\delta_{ji} - \delta_{ki}\right) \tag{2.31}$$

$$= -m_i \frac{P_i}{\rho_i^2} \frac{1}{\Omega_i} \sum_k m_k \nabla_i W_{ki} + \sum_j m_j \frac{P_j}{\rho_j^2} \frac{1}{\Omega_j} m_i \nabla_j W_{ij} \tag{2.32}$$

$$= -m_i \sum_j m_j \left(\frac{1}{\Omega_i} \frac{P_i}{\rho_i^2} \nabla_i W_{ij} + \frac{P_j}{\rho_j^2} \frac{1}{\Omega_j} \nabla_i W_{ij} \right) \tag{2.33}$$

Rearranging terms, the momentum conservation equation can be finally written as:

$$\frac{\mathrm{d}\vec{v_i}}{\mathrm{d}t} = -\sum_{j=1}^{N} m_j \left(\frac{1}{\Omega_i} \frac{P_i}{\rho_i^2} + \frac{1}{\Omega_j} \frac{P_j}{\rho_j^2} \right) \nabla_i W_{ij}(h_i) \tag{2.34}$$

with Ω_i defined as in equation 2.24.

In this formulation, both linear and angular momenta are conserved. Conservation of linear momentum is due to the the antisymmetry of the kernel gradient, which leads to the translational invariance of the Lagrangian and the density estimate. Angular momentum is also conserved because the Lagrangian and the density are invariant to rotations. These results, stress the importance of a spherical kernel: if a non-spherical kernel is used, the rotational invariance for the density estimate would not hold, leading to the non-conservation of angular momentum.

2.2.2.3 Energy equation

We are left with the derivation of the energy equation to close the set of equations needed to follow the hydrodynamics of a fluid.

Making use of the SPH mass conservation equation 2.22, energy conservation equation 2.17 becomes:

$$\frac{\mathrm{d}u_i}{\mathrm{d}t} = \frac{P_i}{\rho_i^2} \sum_j m_j \mathbf{v}_{ij} \cdot \nabla_i W_{ij} \tag{2.35}$$

In GADGET-2, entropy replaces the internal energy as the independent variable (Springel & Hernquist 2002). As such, the EoS 2.18 can be rewritten as:

$$P = A(s)\rho^\gamma \tag{2.36}$$

where the entropic function $A(s)$ is given by:

$$A(s) = \frac{\gamma - 1}{\rho^{\gamma-1}} u. \tag{2.37}$$

Therefore instead of integrating the internal energy, the code follows the evolution of $A(s)$, which for an adiabatic inviscid flow is constant:

$$\frac{\mathrm{d}A}{\mathrm{d}t} = \frac{\gamma - 1}{\rho^{\gamma-1}} \left(\frac{\mathrm{d}u}{\mathrm{d}t} - \frac{P}{\rho^2} \frac{\mathrm{d}\rho}{\mathrm{d}t} \right) \tag{2.38}$$

and thus in the absence of dissipation, meaning that $\left(\frac{\mathrm{d}u}{\mathrm{d}t} - \frac{P}{\rho^2}\frac{\mathrm{d}\rho}{\mathrm{d}t}\right) = 0$, its time derivative becomes:

$$\frac{\mathrm{d}A}{\mathrm{d}t} = 0 \tag{2.39}$$

The use of a time-independent entropic function helps fulfilling energy conservation as time-integration errors are withdrawn.

2.2.3 Artificial viscosity

Up to this point it has been considered that the fluid is continuous up to a smoothing length, meaning that any discontinuity (i.e., shocks) would not be properly resolved. However, there are many astrophysical environments in which shocks are frequently encountered, in particular during the interaction of the nova ejecta with the accretion disk and the stellar companion. In this context, assuring that the kinetic energy of the ejecta is properly converted into thermal energy becomes crucial.

To solve this problem, and in order to capture shocks, SPH uses artificial viscosity (AV). `GADGET-2` uses the formalism derived in Monaghan (1997),

$$v_{ij}^{sig} = c_i + c_j - 3w_{ij} \tag{2.40}$$

where v_{ij}^{sig} is the maximum signal velocity between particles i and j, c the sound speed of each particle and $w_{ij} = \boldsymbol{v}_{ij} \cdot \boldsymbol{r}_{ij} / |\boldsymbol{r}_{ij}|$. Thus if two particles are approaching each other (i.e, $\boldsymbol{v}_{ij} \cdot \boldsymbol{r}_j < 0$), then $v_{ij}^{sig} \geqslant 0$ and the artificial viscosity takes the form:

$$\Pi_{ij} = \frac{\alpha}{2} w_{ij} v_{ij}^{sig}, \tag{2.41}$$

Otherwise $w_{ij} = 0$, ensuring that artificial viscosity will not play a role when particles diverge. This formulation of AV is particle symmetric, this way momentum is conserved. However, artificial viscosity is applied to all particles leading to unwanted dissipation, for example, when we have shear flows. Thus in SPH a 'switch' is used in order to reduce AV in regions outside discontinuities. In `GADGET-2` the implemented switch is based on Balsara (1995) and Steinmetz (1996) and reads as:

$$f_i = \frac{|\nabla \times \mathbf{v}|_i}{|\nabla \cdot \mathbf{v}|_i + |\nabla \times \mathbf{v}|_i} \tag{2.42}$$

An additional term, that accounts for the role played by viscous forces, is included in the momentum conservation equation, in the form:

$$\left.\frac{\mathrm{d}\boldsymbol{v}_i}{\mathrm{d}t}\right|_{visc} = -\sum_{j=1}^{N} m_j f_{ij} \Pi_{ij} \nabla_i \overline{W}_{ij}. \tag{2.43}$$

When particles approach each other, this viscous force produces a repulsive force. Thus, and in order to guarantee total energy conservation, the conversion of the dissipated kinetic energy to thermal energy must be taken into account. This can be done in terms of entropy, which with the inclusion of the viscous terms becomes:

$$\frac{\mathrm{d}A_i}{\mathrm{d}t} = \frac{1}{2}\frac{\gamma-1}{\rho_i^{\gamma}}\sum_{j=1}^{N} m_j f_{ij}\Pi_{ij}\nabla_i W_{ij} \tag{2.44}$$

where $f_{ij} = (f_i + f_j)/2$.

2.2.4 Newtonian gravity

As mentioned before, in SPH a fluid is described in terms of particles, each having a mass (m), position ($\mathbf{r}$), and momentum ($\mathbf{p}$). Thus by solving the N-body problem we can follow the dynamics of the fluid, which for a Newtonian space[2] is described by the Hamiltonian:

$$H = \sum_i \frac{\mathbf{p}_i^2}{2m_i} + G\sum_{ij} m_i\phi_i, \tag{2.45}$$

where

$$\phi(\mathbf{r}_i) = -\sum_j^N \frac{m_j}{r_i - r_j}, \tag{2.46}$$

when considering two particles i and j.

From equation 2.46, it becomes clear that the gravitational potential diverges as the separation between particles j and i approaches zero. Thus, in order to circumvent this issue and properly follow the gravitational dynamics of a fluid, an extra term is added to equation 2.46, in the form:

$$\phi(\mathbf{r}_i) = -\sum_j^N \frac{m_j}{(|\mathbf{r}_i - \mathbf{r}_j|^2 + \epsilon^2)^{1/2}} \tag{2.47}$$

This extra term, called softening length, ϵ, plays a role only at small particle separations which is done in GADGET-2 by using a cubic spline kernel with $W(r, h = 2.8\epsilon)$. This way, the Newtonian form for the interaction is restored at separations greater than the softening length.

The choice of such parameter is not straightforward and it depends on simulation itself. If ϵ is chosen excessively large, high-density regions would be misrepresented; and conversely, if it is chosen too small, particles will tend to collide in low density-regions.

In previous sections, we have seen that each SPH particle has its own size given by its smoothing length. In the simulations reported in this Thesis, the gravitational softening of the plasma particles is taken to be the same as their smoothing length (Pakmor *et al.* 2012). This way, the mass distribution is consistent when solving gravitational and hydrodynamical equations.

2.2.4.1 Tree method

There are different methods to compute gravitational forces. For instance, one may compute gravity for each particle by summing the contributions from all particles (N) in the system, which represent $O(N^2)$ operations. But clearly, for high-resolution numerical simulations, this approach becomes unfeasible. A possible alternative can be envisaged, in which the

[2]See Springel (2005) for more details when not in Newtonian space.

gravitational forces on a given particle can be estimated by grouping distant particles as an indivisible body, while keeping summation for nearby particles. These so-called tree methods are considerably more efficient, with the number of calculations scaling as NlogN.

In `GADGET-2` an oct-tree algorithm (Barnes & Hut 1986) is adopted[3], which is also employed when searching for the neighboring particles. This iterative method starts by considering the entire computational domain as a cube (size l) that contains all the particles. This root node is then subdivided into eight smaller cubes, with size $l = 2$. Each of these cubes is again subdivided into eight subcubes. The process is iterated until the cubes are empty or contain just a single particle (called "leaf node").

Once the tree is constructed, one can determine the gravitational force acting on a particle by walking the tree: starting at the root node, the algorithm inspects if the ratio between the size of a node (l) and the distance between a particle and the center of mass of that node (r) is smaller than a fixed value, called the opening angle (θ):

$$\theta > \frac{l}{r}, \tag{2.48}$$

If true, a multipole expansion of the potential due to the particles within that node is performed. The walk on this branch ceases and the algorithm proceeds to the next node. If the above ratio is larger than θ then the node is opened until the above criterion is met or a leaf node is reached (see Fig. 2.3). The opening angle, can also be seen as an accuracy parameter. It is worth mentioning that the Barnes and Hut algorithm does not yield the exact force, thus by limiting the opening angle one can control the error introduced by the above approximations. If it is chosen small, more nodes are opened, and in turn, a more accurate, as well as a more expensive force computation, is achieved. If it is chosen excessively large, the errors introduced in the computation increase dramatically. A plausible value for θ would be smaller than 1. In our simulations we chose θ to be 0.7. We also chose to construct the tree at each time-step.

As an alternative for the above criterion, `GADGET-2` allows you to choose a different way of walking the tree and open nodes, by taking into account the dynamical state of the simulation. It considers, aside from the size l of a node and its distance r to the particle, the total mass M of that node and the acceleration $|a|$ obtained in the previous time-step. Thus, the force is computed if the following condition is met:

$$\frac{GM}{r^2}\left(\frac{l}{r}\right)^2 \leqslant \alpha|a|, \tag{2.49}$$

where α is the opening angle.

It is worth mentioning that `GADGET-2` uses a monopole order rather than a multipole expansion of the potential. Thus, instead of including higher order corrections, the only term considered for computing the gravity for each cell, is its centre of mass. This choice, despite forcing more nodes to be opened, enables a more efficient construction of the trees: the tree walks become cache-optimized, hence increasing its performance. In addition, the tree is updated consistently with the time-integration scheme used (see section 2.2.5).

[3] `GADGET-2` also supports the use of a combination between the tree algorithm and a Particle-mesh (PM) method. In PM methods, the field quantities are described by making use of a grid. And, since it cannot properly resolve small-scale interactions, it is well suited for cosmological simulations alone. Thus, for the simulations reported in this Thesis only the tree method has been considered. See Springel (2005) and references therein, for details on the PM method.

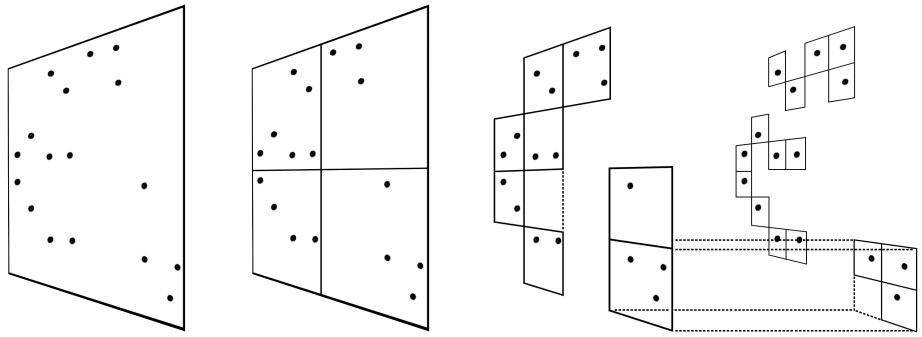

Figure 2.3: Representation of the Barnes and Hut oct-tree structure in two dimensions. Figure taken from Springel *et al.* (2001).

2.2.5 Time integration

To properly follow the evolution of fluids in time, a careful choice of the time-integration scheme used and the time-step size assigned is fundamental.

For N-body simulations the integration scheme that is most frequently used is the leapfrog method, in which the positions and velocities of the particles "leap over" each other by a half time-step. This explicit method is second-order accurate and starts by predicting the position (drift operator) at the middle of a time-step:

$$\mathbf{r}_{i+1/2} = \mathbf{r}_i + \frac{1}{2}\mathbf{v}_i \Delta t \tag{2.50}$$

This is followed by advancing the velocity (kick operator) a full time-step:

$$\mathbf{v}_{i+1} = \mathbf{v}_i + \mathbf{a}_{i+1/2} \Delta t \tag{2.51}$$

and by using this new velocity and the predicted position, we can drift a full time-step:

$$\mathbf{r}_{i+1} = \mathbf{r}_{i+1/2} + \frac{1}{2}\mathbf{v}_{i+1} \Delta t \tag{2.52}$$

where $\mathbf{r}_i$ is the position, $\mathbf{v}_i$ the velocity and $\mathbf{a}_i$ the acceleration of a particle at time t_i.

There is an alternative form of the leapfrog integrator (Quinn *et al.* 1997), where instead of involving the $Drift - Kick - Drift$ (DKD) integrator, uses the $Kick - Drift - Kick$ (KDK) cycle:

$$\mathbf{v}_{i+1/2} = \mathbf{v}_i + \frac{1}{2}\mathbf{a}_i \Delta t \tag{2.53}$$

$$\mathbf{r}_{i+1} = \mathbf{r}_i + \mathbf{v}_{i+1/2} \Delta t \tag{2.54}$$

$$\mathbf{v}_{i+1} = \mathbf{v}_{i+1/2} + \frac{1}{2}\mathbf{a}_{i+1} \Delta t \tag{2.55}$$

The simplectic and time-reversible nature of this integrator ensures conservation of energy and momentum, in addition to be a very stable method when dealing with periodic orbits. In GADGET-2, the KDK scheme is used to obtain the time evolution of any physical property associated with each particle.

In the simulations reported in this Thesis, during the expansion of the ejecta and its interaction with the accretion disk alone, the stellar companion is dynamically "inactive", meaning that the latter region does not need time-steps as small as the former. By using the same time-steps the overall computational cost is greatly increased. Thus to overcome this issue and be able to perform high-resolution simulations, GADGET-2 allows for particles to have individual and adaptive time-steps. In practice what this means is that while active regions will experience the KDK cycle, the inactive ones will feel less kicks over longer time-steps. This scheme prevents from wasting considerable computational resources since advancing the positions, rather than computing accelerations, is extremely cheaper. In GADGET-2 the time-steps are chosen by selecting the smallest value between the Courant and the acceleration time-step criterion:

$$\Delta t_i = min\left[\Delta t_i^{(Courant)}, \Delta t_i^{(accel)}\right] \tag{2.56}$$

The Courant time-step criterion ($\Delta t_i^{(Courant)}$) defined as the maximum velocity $max(v_{ij}^{sig})$ (see equation 2.40) of particle i with respect to all neighbors j, is given by:

$$\Delta t_i^{(Courant)} = \frac{C_{courant} h_i}{max_j(v_{ij}^{sig})} \tag{2.57}$$

where h_i is the smoothing length of particle i, and $C_{courant}$ the so-called Courant factor (taken as 0.15 for all the models reported in this Thesis).

The acceleration time-step criterion is given by:

$$\Delta t_i^{(accel)} = \sqrt{\eta \frac{2\epsilon}{a_i}} \tag{2.58}$$

where η is an accuracy parameter taken to be 10^{-5}, ϵ the gravitational softening and a_i the particle acceleration. The individual time-steps for each particle (δt_i) are assigned to be a fraction of the global time-step (t_{glob}) (Hernquist & Katz 1989), in the form:

$$\delta t_i = \frac{t_{glob}}{2^{n_i}} \tag{2.59}$$

where the global time-step is taken to be the minimum of the time-steps (i.e., $t_{glob} = \min_i \Delta t_i$) and $n_i \geq 0$ is an integer that characterizes the time bin of a particle. Particles are permitted to change its time-step to smaller values, and allowed to jump to larger ones only every second step. Such scheme ensures synchronization at the end of a higher time-step.

2.2.6 Additional physics

GADGET-2 was mainly thought for cosmological simulations, thus to be able to follow the orbital evolution of classical and recurrent novae systems additional physics had to be included. In the simulations presented in this Thesis, the system is placed in a rotating reference frame, meaning that both Coriolis and centrifugal forces are needed.

After computing the gravitational acceleration and before kicking the particles to a new time-step, for each particle i both the centrifugal and Coriolis terms are added to the gravitational acceleration, such that:

$$a_i^{grav} = a_i^{grav} + \Omega \times (\Omega \times r_i) + 2(\Omega \times v_i) \tag{2.60}$$

where the second and third term are the centrifugal and Coriolis terms respectively, with Ω the angular velocity vector.

2.3 Initial conditions

The initial conditions of an object in SPH are built from its one-dimensional model. The goal is to find a stable three-dimensional particle distribution, that describes both the density and pressure profiles of that model. This can be accomplished by assigning a position, a velocity, a mass as well as internal energy to each particle that compose that object. Therefore, the initial distribution of these particles deserve special attention in order to build a valid initial model. In this section, we give a description on how each component, that forms the classical or the recurrent nova systems considered in this Thesis, is modeled. For convenience, and to guarantee good accuracy in the interpolated functions, all the SPH particles that form the models shown in the present study have the same mass.

2.3.1 The companion

Fig. 2.4 depicts the modelling procedure adopted to build the companion star. We start by computing a one-dimensional profile of the density (right-top plot) and pressure.

In SPH, in order to obtain satisfactory results, a large number of particles is needed which translates into a great deal of computational resources. Thus, by performing preliminary simulations to study the penetration of the particles during the collision between the nova ejecta and the secondary, we were able to find that particles are not expected to penetrate deep inside the star (right-middle plot). In fact, the results show that the ejecta may penetrate, at most, through the outer 0.1 $R_\odot$ of the secondary (see dotted, black line in the upper-middle panel as a representation). With this in mind, and to be on the safe side, the outermost ~ 0.2 $R_\odot$ of the star has been taken into account (third panel). The rest of the star has been replaced by a point-like mass located at its center (lower-middle panel).

The next step is to generate the initial 3D particle distribution of the outer layers of the companion. Taking the density and pressure profiles of the outer layers (lower-middle panel), we slice it into several shells of equal radius. Knowing the total mass, one can easily infer the number of SPH (N_{sph}) particles within each mass shell (M_{shell}):

$$N_{sph} = \frac{M_{shell}}{m_{sph}} \tag{2.61}$$

where m_{sph} is the mass of an SPH particle.

For each shell, a "glass" technique has been implemented (White 1996): in essence, a cube is filled with a random number of particles until a uniform distribution is achieved (lower-middle panel), from which a shell with constant density is extracted. The same procedure is used for each shell at different densities. Placing one shell after another, we obtain the initial model for the outer layers of the companion (lowermost panel).

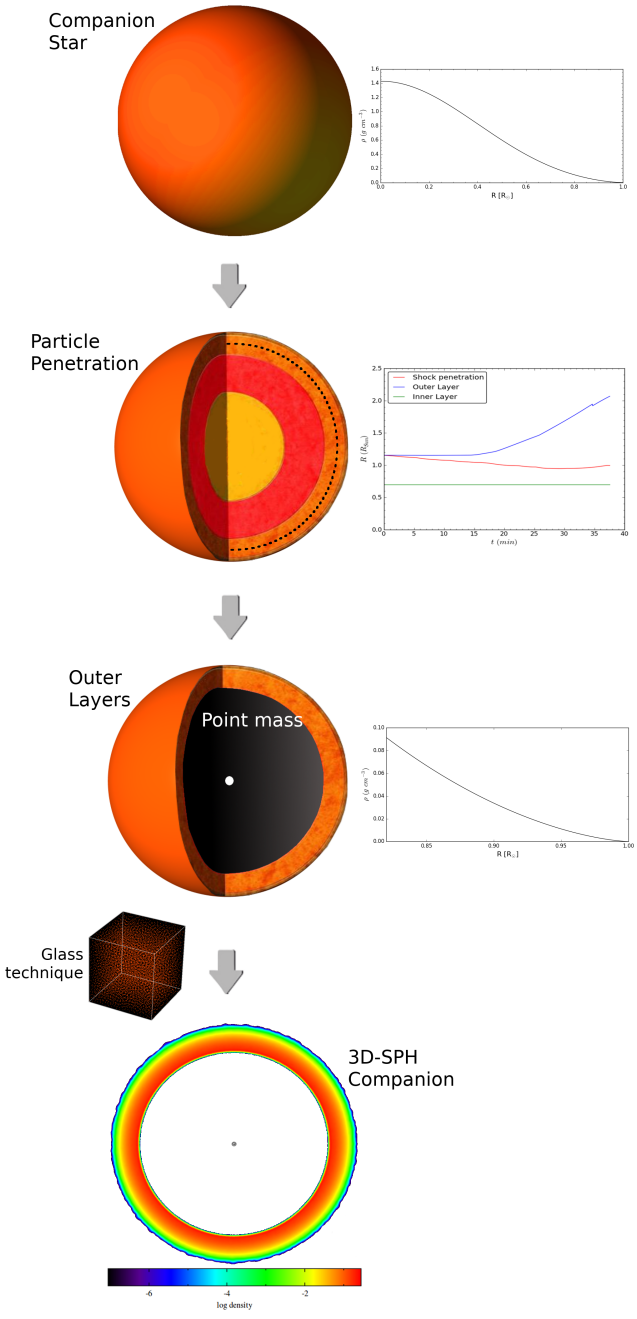

Figure 2.4: Schematic representation of the modeling procedure adopted to build the companion star. The dotted line in the middle panel represents the particle penetration after the outburst. The used values are taken from Chapter 3.

Once the star has been built, another requirement is to remove the noise resulting from this setup and to guarantee that the resulting 3D structure is in hydrostatic equilibrium. Thus, the stellar secondary is relaxed for several orbital periods. To speed up this process, we apply an explicit damping force that slows down random motions (Rosswog *et al.* 2004):

$$\frac{dv_i}{dt} = -f_d v_i \tag{2.62}$$

where f_d is the damping factor and is of the order of a few percent (e.g. $f_d = 0.01$). We allow it for several orbital periods. To know if the relaxation was effective, the particle velocities will hold near zero even without the damping term.

2.3.2 The white dwarf and the ejecta

The white dwarf is modeled as a point-like mass, which is enough to account for its gravitational pull on the system. The ejecta is extracted from models of nova outbursts, computed through accretion, expansion, and ejection by means of the 1D, spherically symmetric, Lagrangian, hydrodynamic code `SHIVA` (see José & Hernanz 1998; José 2016, for details). When most of the envelope, following expansion at high velocities, reaches escape velocities, we map the structure of the ejecta onto a 3D domain using the technique explained above (see section 2.3.1).

2.3.3 The accretion disk

As mentioned before, to generate a 3D particle distribution, the radial profiles for the density and pressure are needed. From these profiles and to obtain a uniform particle distribution, the same "glass" technique is used for each shell at different densities assuming, in this case, axial symmetry.

In addition, the sound-crossing timescale throughout the disk is of the order of hours, while the timescale required for the ejecta to reach and hit the disk is of the order of seconds or minutes. Therefore, no relaxation of the disk is needed.

2.3.3.1 Structure

We modeled the structure of the accretion disk, that orbits the point-like white dwarf in Keplerian rotation, according to the Shakura-Sunyaev thin disk solution (Shakura & Sunyaev 1973). The exact origin of the viscous dissipations that allow for the accretion disk to form are still unknown. There are theories suggesting that the source is of turbulent nature related with the presence of magnetic fields (Balbus & Hawley 1991) or driven by convection (Goldman & Wandel 1995); others propose that the origin is a combination of hydrodynamical effects (Sawada *et al.* 1986). The incomprehension on the exact mechanism led Shakura & Sunyaev (1973) to follow a different approach. They introduced a parameter (α) that accounts for all unknown variables related with the source of viscosity such that:

$$\nu = \alpha c_s H, \tag{2.63}$$

where ν is the viscosity coefficient, c_s the sound speed and H the scale height (starting at midplane) of the disk at radius R:

$$H \sim \frac{c_s}{v_\phi} R \tag{2.64}$$

where the azimuthal velocity (v_ϕ) for a geometrically-thin disk ($H/r \ll 1$) takes the Keplerian value:

$$v_\phi \sim v_K = \left(\frac{GM}{R}\right)^{\frac{1}{2}} \tag{2.65}$$

where G is the gravitational constant and M the mass of the accretor. Finally, the parameter α in equation 2.63 is a dimensionless constant, taken to be $\lesssim 1$, that determines the rate of angular momentum transportation. Observations indicate that for CV systems this parameter is $\sim 0.1 - 0.4$ (see King *et al.* 2007, and references therein). In the current study, we use this standard α-prescription to model the disks. A detailed description of such model together with the complete set of equations describing the structure of the Shakura-Sunyaev disk can be found in Frank *et al.* (2002).

2.3.3.2 Geometry

From a geometrical point of view, the accretion disk is built by considering two different configurations (Fig. 2.5):

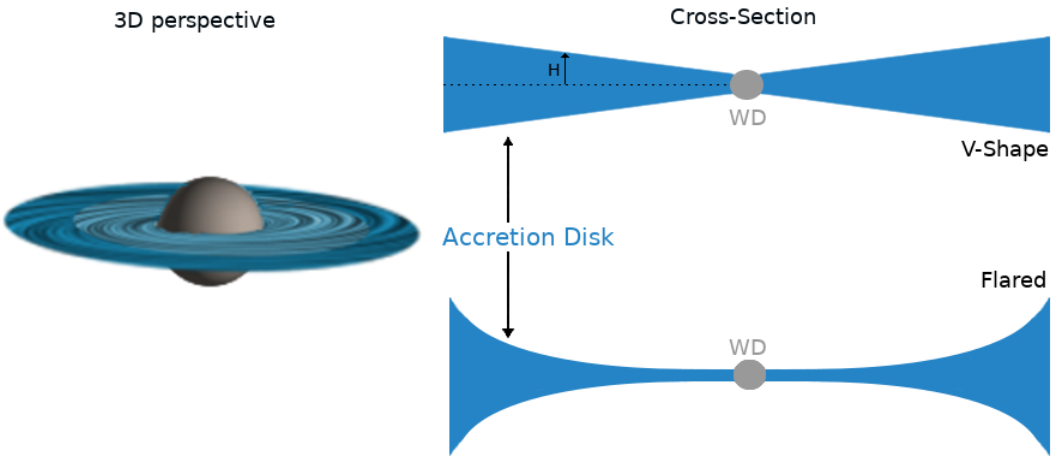

Figure 2.5: Schematic representation of the geometries adopted to build the accretion disk. H is the scale height.

- The Shakura & Sunyaev (1973) V-shaped thin disk:

$$H_{V-shape}/R \ll 1 \tag{2.66}$$

- The Hachisu & Kato (2000) flared shaped disk:

$$H_{flared} = \beta R_{disk} \left(\frac{R_{circ}}{R_{disk}}\right)^2 \tag{2.67}$$

  where β is taken to be 0.3.

The considered outer radius, R_{disk}, is taken from Warner (2005):

$$R_{disk} \cong 0.9 R_{RL}^{WD} \tag{2.68}$$

where R_{RL}^{WD} is the Roche-lobe radius of the WD (Eggleton 1983), and is given by:

$$R_{RL}^{WD} = \frac{0.49 q^{2/3}}{0.6 q^{2/3} + ln(1 + q^{1/3})} a \tag{2.69}$$

where $q = M_{WD}/M_{companion}$ is the mass ratio. The inner radius or circularization radius, (R_{circ}), is placed at the outer edge of the ejecta.

2.3.4 Binary system

In section 2.3.1, we built and relaxed the companion in isolation, not taking into account the tidal effects of the primary. This step aims at building a binary system more accurately by taking these effects into consideration. An example of the initial configuration, taken from Chapter 3, is shown in Fig. 2.6.

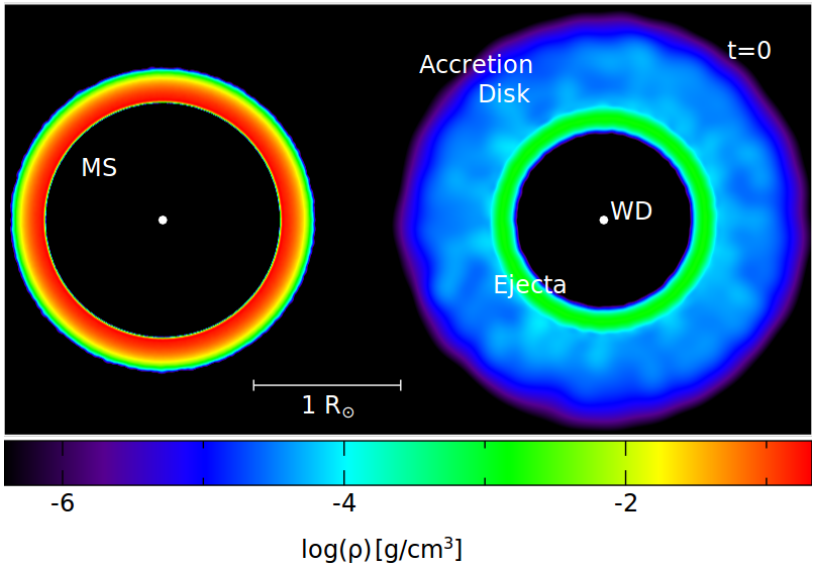

Figure 2.6: Cross-sectional slice in the binary orbital plane (XY) showing the initial conditions for Model A (see Chapter 3).

Thus, to relax the binary system we follow the procedure adopted by Rosswog *et al.* (2004) and Lajoie & Sills (2010), in which the companion and the primary are placed together in the corotating frame of the binary system. In this frame, stars should be at rest and the velocities of the SPH particles should tend to zero.

To achieve a circular orbit, we compute the angular velocity (Ω) at each time-step, by requiring that the force felt on the centre of mass of the secondary (a_{cm}^{sec}) with mass M_{sec},

$$a_{cm}^{sec} = \frac{\sum_i m_i (a_i^{hydro} + a_i^{grav})}{M_{sec}} \tag{2.70}$$

has to be canceled by the centrifugal forces evaluated at the center of mass, which yields the following condition:

$$\Omega_i^2 = \frac{\sum_i m_i(a_i^{hydro} + a_i^{grav})}{\sum_i m_i r_i}, \tag{2.71}$$

where m_i, a_i^{hydro} and a_i^{grav} are the mass, the hydrodynamic and the gravitational accelerations of particle i, respectively; r_i is the distance of each particle to the axis of rotation.

By adding the non-inertial forces, the acceleration felt by particle i, during the relaxation, can be translated into:

$$a_i = a_i^{grav} + a_i^{hydro} - \Omega \times (\Omega \times r_i) - f_d v_i, \tag{2.72}$$

where the third term in the equation is the centrifugal acceleration and the last term is a damping factor to expedite the relaxation, as discussed in section 2.3.1.

After several orbital periods and once the system reaches a stable configuration, we move the system back to reference frame of the binary and place the ejecta and the disk encircling the primary (see Fig. 2.6). Note that at this point, if rotation is considered, the radial velocities are added and in addition to the centrifugal acceleration, a coriolis term is now included (see Eq. 2.60 in section 2.2.6).

Finally, it is worth mentioning the computational time spent on the relaxation procedure. Fig. 2.7 shows the time spent on the relaxation for the companion alone and for the binary system for a total of $\sim$ 14.8 million SPH particles. As can be seen, using 12 CPUs, the overall relaxation can take nearly 4 months, with the most expensive processes being the hydrodynamics[4] and the gravitational force computation[5].

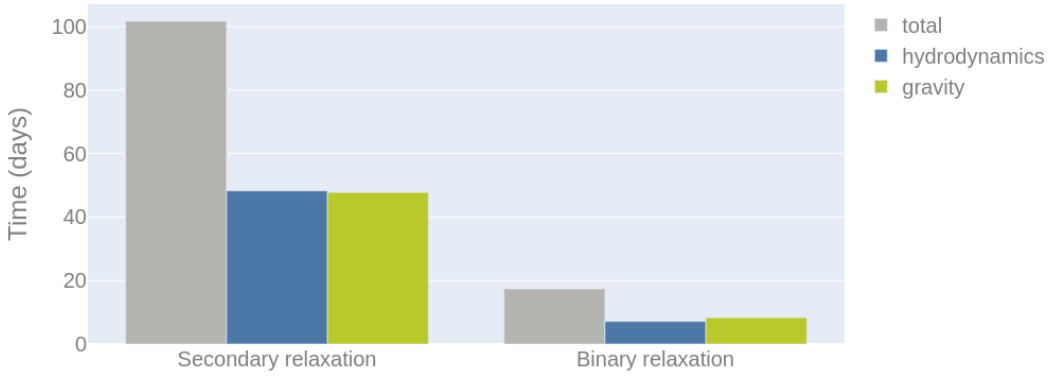

Figure 2.7: Time spent on the overall relaxation procedure for 14824752 SPH particles, using 12 CPUs.

[4]The time spent on hydrodynamics includes neighbour search, density determination, and SPH communication.

[5]The time spent on gravitational forces includes tree walks, construction as well as communication.

Chapter 3

Three-dimensional simulations of the interaction between the nova ejecta, accretion disk, and companion star

Published in Figueira, J., José, J., García-Berro, E., Campbell, S.W., García-Senz, D., Mohamed, S. (2018), Astronomy & Astrophysics, 613, A8

Shortly after the outer layers of the white dwarf expand and achieve escape velocity, a fraction of the ejected material is expected to collide with the secondary star. As a result, part of the nova ejecta mixes with the outermost layers of the secondary. The resulting chemical contamination may have potential implications for the next nova cycle, once mass transfer from the secondary resumes. Thus, in this Chapter we perform a first set of numerical simulations of the interaction between the nova ejecta, accretion disk, and companion star for a Classical Nova system.

This Chapter is organized as follows. The input physics, and initial conditions adopted are described in Sect. 3.1. A full account of the 3D simulations of the interaction of the ejecta with the accretion disk, and ultimately with the main sequence companion, is presented in Sect. 3.2. The effect of the different parameters on the stability of the accretion disk and on the amount of mass lost from the system is also analyzed in Sect. 3.2. The expected level of chemical contamination of the outer layers of the secondary star is discussed in Sect. 3.3. A summary of the most relevant conclusions of this Chapter is presented in Sect. 3.4.

3.1 Model and input physics

3.1.1 Model

The first stages of the evolution of the nova outbursts, through accretion, expansion, and ejection, were modeled by means of the 1D, spherically symmetric, Lagrangian, hydrodynamic code `SHIVA` (see José & Hernanz 1998; José 2016, for details). When the inner edge of

the ejecta reached a size of 0.65 $R_\odot$, the structure was mapped onto a 3D domain, which also included the white dwarf that hosts the nova explosion, the accretion disk, and the main sequence companion. In Section 2.3 a more comprehensive step-by-step description on how we built each component can be found. The evolution of the system was subsequently followed with the 3D smoothed-particle hydrodynamics (SPH) code `GADGET-2` (Springel *et al.* 2001; Springel & Hernquist 2002; Springel 2005). This parallelized, explicit, Lagrangian, mesh-free code describes fluids in terms of a set of discrete elements (hereafter, particles). For a more detailed description on this type of code, and in particular on `GADGET-2`, see Chapter 2.

The characteristic size of the overall binary system, for a given set of values of the masses of the primary and secondary stars, is determined by the orbital period. In the simulations reported in this Chapter, a value of $P_{\rm orb} = 8.9$ hr was adopted. This is a representative value of long-period classical nova systems, $P_{\rm orb} > 7$ hr, which may represent about 20% of all novae (Tappert *et al.* 2013). We did not consider the rotation of the binary system since the overall duration of the interaction between the ejecta, the disk, and the secondary is very small. In fact, the orbital period adopted is ~ 12 times longer than the time it takes for the ejecta to reach and hit the main sequence companion.

Table 3.1: Models computed.

Model	$M_{\rm ejecta}$ ($M_\odot$)	$M_{\rm disk}$ ($M_\odot$)	$V_{\rm ejecta}^{\rm max}$ (km s^{-1})	H/R	Disk disruption
A	5.14×10^{-4}	2.04×10^{-5}	1200	0.03	Yes
$A_{\rm hres}$[a]	5.14×10^{-4}	2.04×10^{-5}	1200	0.03	Yes
B	5.14×10^{-4}	2.04×10^{-5}	800	0.03	Yes
C	5.14×10^{-4}	9.28×10^{-5}	1200	0.03	No
D	5.14×10^{-4}	9.28×10^{-5}	800	0.03	No
E	1.60×10^{-3}	2.04×10^{-5}	1200	0.03	Yes
F	1.60×10^{-3}	2.04×10^{-5}	800	0.03	Yes
G	5.14×10^{-4}	3.96×10^{-5}	1200	0.06	No
H	1.60×10^{-3}	3.96×10^{-5}	1200	0.06	Yes
I	5.14×10^{-4}	9.28×10^{-5}	3000	0.03	No
J	5.14×10^{-4}	3.96×10^{-5}	3000	0.06	Yes
K	5.14×10^{-4}	2.04×10^{-5}	1200	0.06	Yes

[a] Model computed with twice the number of particles than Model A.

3.1.2 Initial configuration

The 3D computational domain[1] of the simulations discussed in this Chapter includes the white dwarf that hosts the nova explosion, the expanding nova ejecta, the accretion disk, and the main sequence companion.

[1]The presence of a disk, and its key role in the simulations reported in this Chapter, does not allow us to rely on SPH axisymmetric codes to increase the resolution of the models, in contrast to other astrophysical scenarios such as type Ia supernovae (See, e.g., García-Senz *et al.* 2012).

3.1.2.1 White dwarf star

The white dwarf is modeled as a 0.6 $M_\odot$ point-like mass, which is enough to account for its gravitational pull on the system. The expanding ejecta, which at the beginning of the 3D simulations is located between 0.65 $R_\odot$ (inner edge) and 0.72 $R_\odot$ (outer edge) from the underlying white dwarf, has a mean metallicity of $Z = 0.54$, and a mass, density, and velocity profiles corresponding to the values computed with the 1D code `SHIVA` (see Sect. 3.1.1, for details).

3.1.2.2 Main sequence star

A 1 $M_\odot$, solar metallicity, main sequence companion is adopted as the secondary. The star has spherical symmetry and is built in hydrostatic equilibrium conditions. A polytropic equation of state with $\gamma = 5/3$ was considered. The corresponding density and internal energy profiles were subsequently mapped onto a 3D particle distribution. To avoid a substantial computational load, only the outer layers of the main sequence star were considered, since during the collision between the nova ejecta and the secondary, particles are not expected to penetrate deep inside the star. Even though preliminary simulations suggest that the ejecta may penetrate, at most, through the outer ~ 0.1 $R_\odot$ of the secondary, the outermost ~ 0.2 $R_\odot$ (0.15 $M_\odot$) of the star was taken into account. The rest of the star was replaced by a point-like mass located at its center. See Chapter 2.3 for a detailed description on how to generate the initial 3D particle distribution of the outer main sequence layers, the accretion disk and the ejecta.

The initial density profile for the outer main sequence layers is shown in Fig. 3.1. For convenience, and to guarantee good accuracy in the interpolated functions, all smoothed-particle hydrodynamics (SPH) particles used have the same mass, $\sim 10^{-8}$ $M_\odot$. One can easily infer the number of SPH particles within each mass shell from its total mass. About 3.8 million SPH particles were used to model the outer ~ 0.2 $R_\odot$ (0.15 $M_\odot$) of the secondary. To guarantee that the resulting 3D structure is in hydrostatic equilibrium, the stellar secondary is relaxed for a total time on the order of 20 orbital periods.

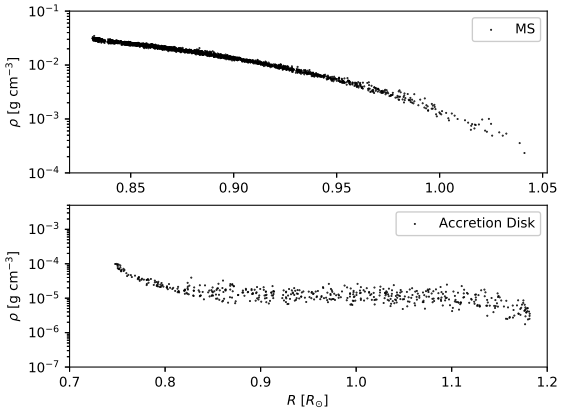

Figure 3.1: Initial density profiles for the outer main sequence layers (after relaxation) and the accretion disk.

Table 3.2: Mass (ejecta plus disk) gravitationally bound to the secondary star, $\Delta M_{\rm MS}$, and to the white dwarf, $\Delta M_{\rm WD}$, and total mass leaving the binary system, $\Delta M_{\rm esc}$, together with their fractions (in %) over the total ejecta plus disk masses, after collision with the nova ejecta. The parameter $\Delta M_{\rm MS,lost}$ is the mass lost by the main sequence star in the interaction with the nova ejecta.

Model	$\Delta M_{\rm MS}(M_\odot)$	$\Delta M_{\rm WD}(M_\odot)$	$\Delta M_{\rm esc}(M_\odot)$	$\frac{\Delta M_{\rm MS}}{(M_{\rm ejecta}+M_{\rm disk})}$	$\frac{\Delta M_{\rm WD}}{(M_{\rm ejecta}+M_{\rm disk})}$	$\frac{\Delta M_{\rm esc}}{(M_{\rm ejecta}+M_{\rm disk})}$	$\Delta M_{\rm MS,lost}(M_\odot)$
A	1.95×10^{-5}	4.64×10^{-5}	4.69×10^{-4}	3.65%	8.68%	87.7%	2×10^{-7}
$A_{\rm hres}$	2.05×10^{-5}	4.83×10^{-5}	4.66×10^{-4}	3.83%	9.03%	87.2%	1.4×10^{-7}
B	2.92×10^{-5}	1.01×10^{-4}	4.05×10^{-4}	5.46%	18.9%	75.6%	-
C	4.96×10^{-5}	1.50×10^{-4}	4.08×10^{-4}	8.17%	24.7%	67.2%	1.6×10^{-7}
D	6.20×10^{-5}	1.83×10^{-4}	3.62×10^{-4}	10.2%	30.2%	59.7%	1.2×10^{-7}
E	5.62×10^{-5}	1.12×10^{-4}	1.45×10^{-3}	3.47%	6.93%	89.7%	1.4×10^{-6}
F	9.82×10^{-5}	2.66×10^{-4}	1.26×10^{-3}	6.06%	16.4%	77.6%	4.8×10^{-7}
G	5.69×10^{-5}	1.71×10^{-4}	3.26×10^{-4}	10.3%	30.9%	58.9%	4×10^{-8}
H	6.06×10^{-5}	1.25×10^{-4}	1.46×10^{-3}	3.69%	7.60%	88.8%	1.3×10^{-6}
I	2.17×10^{-5}	4.79×10^{-5}	5.40×10^{-4}	3.57%	7.88%	88.9%	2.4×10^{-6}
J	1.66×10^{-5}	5.55×10^{-5}	4.83×10^{-4}	3.00%	10.0%	87.2%	1.4×10^{-6}
K	5.39×10^{-5}	1.61×10^{-4}	3.20×10^{-4}	10.1%	30.1%	59.8%	-

3.1.2.3 Mass-accretion disk

We modeled the accretion disk that orbits the point-like white dwarf in Keplerian rotation according to the Shakura-Sunyaev, V-shaped disk solution (Shakura & Sunyaev 1973; Frank *et al.* 2002). In our fiducial model (hereafter, Model A; see Table 3.1) we assumed a solar-composition disk with a mass of $2 \times 10^{-5}\ M_{\odot}$ and a geometry given by a ratio of height to radius of $H/R = 0.03$, (see Sects. 3.2.4 and 3.2.5, for the effect of these parameters on the simulations). Other models of accretion disks (e.g., flared disks) and inclusion of alternative assumptions (smaller extended disks; see Warner 2009) will be addressed in the next chapters; see Puebla *et al.* (2007) for a comparison between current disk models and observational data. In this Chapter, the accretion disk contains only a few thousand SPH particles, which is the truly limiting factor of the simulations; the nova ejecta contains up to 19,000 SPH particles. The sound-crossing time throughout the disk is ~ 4 hours, while the time required for the ejecta to reach and hit the disk is ~ 6 minutes. Therefore, no relaxation of the disk, also built by means of the cubic *glass* technique, is needed. The initial density profile for the mass-accretion disk is shown in Fig. 3.1.

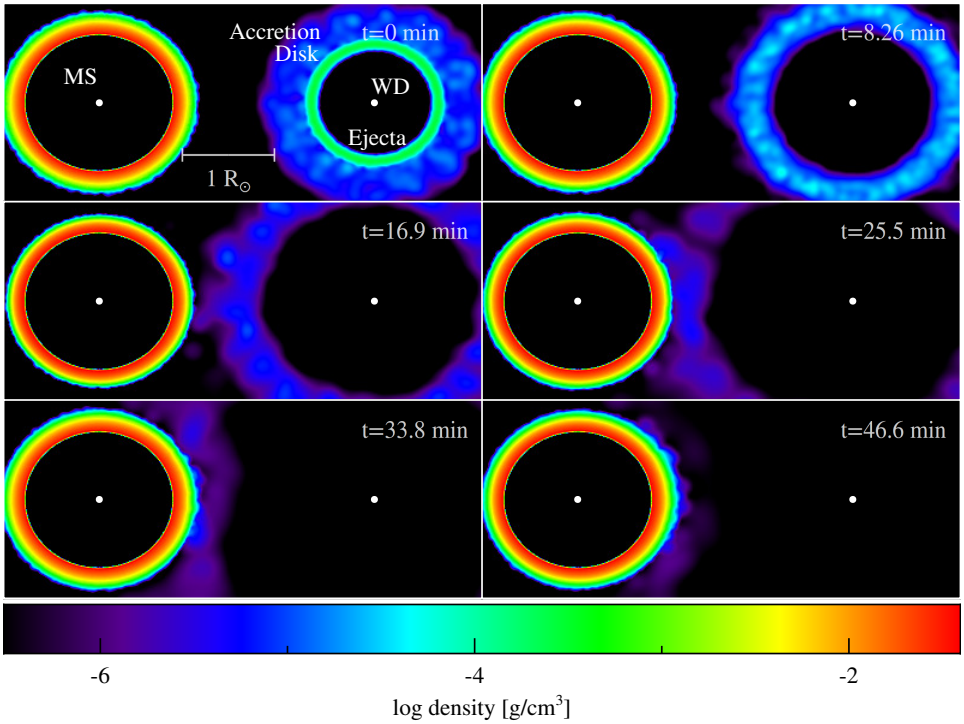

Figure 3.2: Cross-sectional slice in the binary orbital plane (XY) showing the density of Model A at various stages of the interaction between the nova ejecta and the accretion disk, subsequently followed by a collision with the main sequence companion. A movie showing the full evolution of this model, `modelA-XY.mov`, is available at `http://www.fen.upc.edu/users/jjose/Downloads.html`. See also `modelA-YZ.mov`, for a movie depicting the evolution of the system from a side view (YZ plane). Snapshots and movies were generated by means of the visualization software SPLASH (Price 2007).

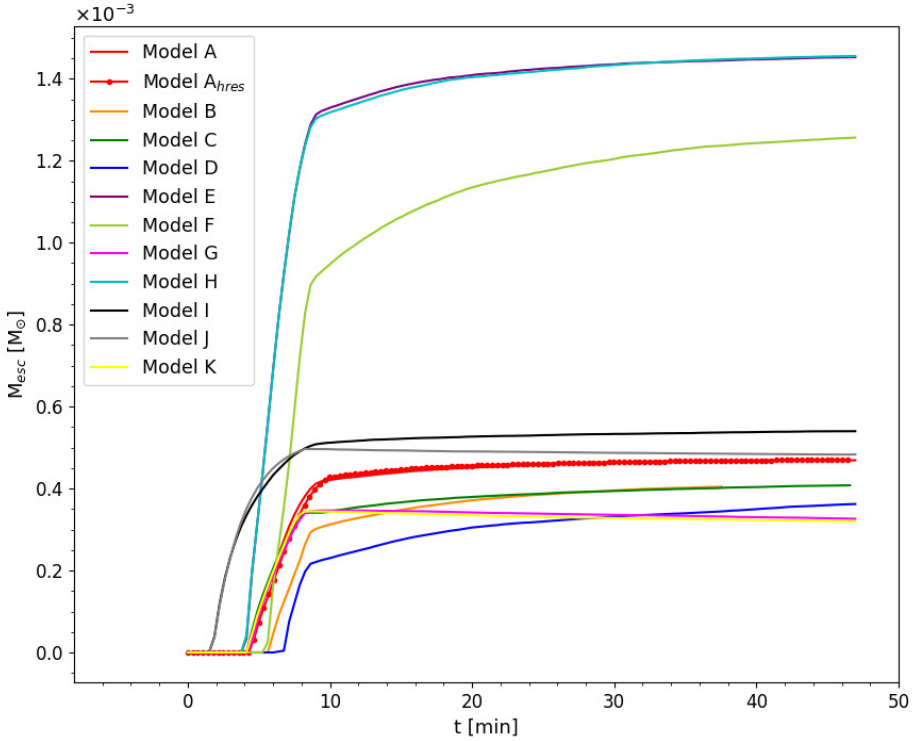

Figure 3.3: Time evolution of the mass leaving the binary system for the models reported in this Chapter.

3.2 Results: disk stability and mass loss

Observations suggest that the accretion disk does not always get disrupted by a nova outburst[2]. Indeed, in some systems, the presence of a disk has been confirmed only a few months/years after the explosion (see, e.g., Leibowitz *et al.* 1992; Retter *et al.* 1998, 1997; Skillman *et al.* 1997; Hernanz & Sala 2002), which is clearly at odds with the typical timescales required for a disk to assemble (on the order of decades). It has been suggested that the accretion disk is only disrupted if the system is an intermediate polar (Corradi *et al.* 2003). In those systems, the magnetic field could truncate the inner regions of the disk, which would be less massive than in nonmagnetic systems, and therefore, prone to be disrupted by a nova explosion. However, it is worth noting that the mass and mean density of such disks are also poorly constrained quantities from an observational viewpoint.

To elucidate the possible effect of the nova outburst on the accretion disk, we considered

[2]See, however, Drake & Orlando (2010), for simulations of recurrent nova systems leading always to full disruption of the accretion disks.

a suite of models aimed at testing the influence of the different parameters of the system (i.e., mass and velocity of the ejecta, mass, and geometry of the accretion disk; see Table 3.1).

3.2.1 Evolution of model A

Model A describes the interaction between $M_{\rm ejecta} = 5.1 \times 10^{-4}\ M_\odot$, ejected from a 0.6 $M_\odot$ white dwarf during a nova outburst (with a maximum velocity of the ejecta of $V_{\rm ejecta}^{\rm max} = 1200$ km s^{-1}), and a $2 \times 10^{-5}\ M_\odot$ accretion disk (with $H/R = 0.03$), subsequently followed by the collision with a 1 $M_\odot$ main sequence companion (see Table 3.1). Snapshots of the evolution of this model, in terms of density, are shown in Fig. 3.2. Movies showing the full evolution of this model are available at `http://www.fen.upc.edu/users/jjose/Downloads.html`.

The ejecta hits the disk a few seconds after the beginning of the simulation (Fig. 3.2, upper panels). The energy released during the collision heats the disk, which achieves a maximum temperature of $\langle T_{\rm disk}^{\rm max} \rangle \sim 1.4 \times 10^6$ K; only a handful of SPH particles (~ 20) reach $T^{\rm max} \sim 1.2 \times 10^7$ K. This suggests that nuclear reactions do not play a relevant role in the interaction[3]. Only a small fraction of the nova ejecta hit the disk ($m'_{\rm ejecta} \sim 1\% M_{\rm ejecta}$); the mean kinetic energy, $K = \frac{1}{2} m'_{\rm ejecta} V_{\rm ejecta}^2 \sim 7 \times 10^{43}$ ergs. A crude estimate of the gravitational binding energy of the disk can be obtained from $U \sim G M_{\rm WD} M_{\rm disk}/r_{\rm mean}$, where G is the gravitational constant, $M_{\rm WD}$ is the mass of the underlying white dwarf, and $M_{\rm disk}$ and $r_{\rm mean}$ are the mass of the disk and the mean distance between the white dwarf and the disk. Estimates for Model A yield $U \sim 6 \times 10^{43}$ ergs, which are similar to the kinetic energy of the impinging ejecta. In Model A, simulations reveal the total disruption of the disk (middle left panel), which gets totally swept up and mixed with the ejecta. However, other models with different choices for the geometry (H/R), mass, and velocity of the disk, and mass of the ejecta, may yield different outcomes (see below).

At about $t \sim 17$ min (middle panels), a mixture of ejecta and disk material impinges on the main sequence companion. The temperature increases slightly in the outermost layers of the secondary, but not enough to spark nuclear reactions. In the collision, a subset of the ejecta/disk particles penetrate through the outer layers of the secondary, reaching a maximum depth of $\sim 1.1 \times 10^{-5}\ M_\odot$ from the surface. The energy released in the collision drives a moderate expansion of the outer layers of the star (lower panels). Since the secondary overfills its Roche lobe, part of the material incorporated into the main sequence star is later re-accreted by the white dwarf, as soon as mass-transfer resumes and the accretion disk is re-established.

About $\sim 4.7 \times 10^{-4}\ M_\odot$ (i.e., 88% of the mixture of disk and nova ejecta) leave the binary system in Model A. In contrast, only $\sim 2 \times 10^{-5}\ M_\odot$ (3.7%; mostly nova ejecta) remain gravitationally bound to the main sequence companion, while $\sim 4.6 \times 10^{-5}\ M_\odot$ (8.7%) are bound to the white dwarf (see Table 3.2). A small amount of mass, $2 \times 10^{-7}\ M_\odot$, involving only a handful of SPH particles, is expelled from the outer main sequence layers in the interaction with the nova ejecta. Figure 3.3 shows the time evolution of the mass leaving the binary system in Model A and for all models reported in this Chapter. The early and sharp increase in mass loss ($t \leq 10$ min) results from the interaction between the nova ejecta and the disk, when the latter gets totally swept up and mixed with the former. Most of the ejecta and disk mixture leaves the binary system. The longer-term evolution of the mass

[3]The same conclusion applies to all models reported in this Chapter.

loss plot ($t > 10$ min) reveals that little is expelled from the outer main sequence layers as a result of the impact with the nova ejecta.

To test the feasibility of these results, a higher resolution run with twice the number of particles as Model A (hereafter, Model A_{hres}) was also performed. As shown in Table 3.2 (see also Fig. 3.3), both models A and A_{hres} yield similar results, which suggests that the overall number of particles adopted in this Chapter was appropriate. Movies showing the full evolution of Model A_{hres} are also available at `http://www.fen.upc.edu/users/jjose/Downloads.html`.

3.2.2 Effect of the mass of the nova ejecta

We considered two values for the mass of the nova ejecta, M_{ejecta}, to analyze the effect of this parameter. As shown in Table 3.2, a comparison between our fiducial Model A (characterized by $M_{ejecta} = 5.1 \times 10^{-4}\ M_{\odot}$) and Model E (with $M_{ejecta} = 1.6 \times 10^{-3}\ M_{\odot}$) reveals that, as expected, increasing the mass of the ejecta translates into larger masses gravitationally bound to the white dwarf (ΔM_{WD}) and to the main sequence companion (ΔM_{MS}), at the end of the simulations. In turn, the total amount of mass lost from the system, ΔM_{esc}, also increases. We found an identical pattern when comparing Models B and F—for which a maximum velocity of the nova ejecta of $V_{ejecta}^{max} = 800$ km s^{-1} was assumed—and Models G and H—for which $V_{ejecta}^{max} = 1200$ km s^{-1}, but has twice the mass of the disk compared to Model A. There is one exception to this: whereas the accretion disk gets fully disrupted in Models A, B, E, F, and H, the disk survives the collision with the ejecta in Model G (Fig. 3.4). This can be understood from the ratios M_{ejecta}/M_{disk} adopted in the various models; the lowest value, $M_{ejecta}/M_{disk} \sim 13$, corresponds to Model G, which suggests that only disks with masses much lower than the ejecta undergo total disruption. The fact that the disk gets disrupted in Model H but not in Model G affects the dynamics of the system and results in a moderately larger amount of mass that remains bound to the white dwarf in the former. Except for this peculiar case, the fraction of the overall mass available (i.e., ejecta plus disk) that escapes the binary system (or remains bound to the main sequence or to the white dwarf) does not depend much on the choice of the mass of the nova ejecta (see Table 3.2). We note, indeed, that the fraction of mass leaving the system increases from 59% to 89%, while the fraction that remains bound to the white dwarf drops from 31% to 8%, when comparing Models G and H. As reported for Model A, small amounts of mass, up to $1.4 \times 10^{-6}\ M_{\odot}$, involving only a few SPH particles, are expelled (if any) from the outer main sequence layers in the interaction with the nova ejecta, and values increase for larger nova ejected masses.

3.2.3 Effect of the velocity of the ejecta

Three values for the maximum velocity of the ejecta, V_{ejecta}^{max}, representative of classical nova systems (Gehrz et al. 1998), were adopted to analyze the influence of this parameter as follows: 800 km s^{-1}, 1200 km s^{-1}, and 3000 km s^{-1}. Comparison between Models A and B reveals that an increase in the velocity of the ejecta yields larger ejected masses from the binary system, while reducing the amount of mass that remains gravitationally bound, either to the white dwarf or to the main sequence companion.

The fraction of nova ejecta plus disk mass that escapes the binary system (or remains bound to the main sequence or to the white dwarf) follows exactly the same trend. How-

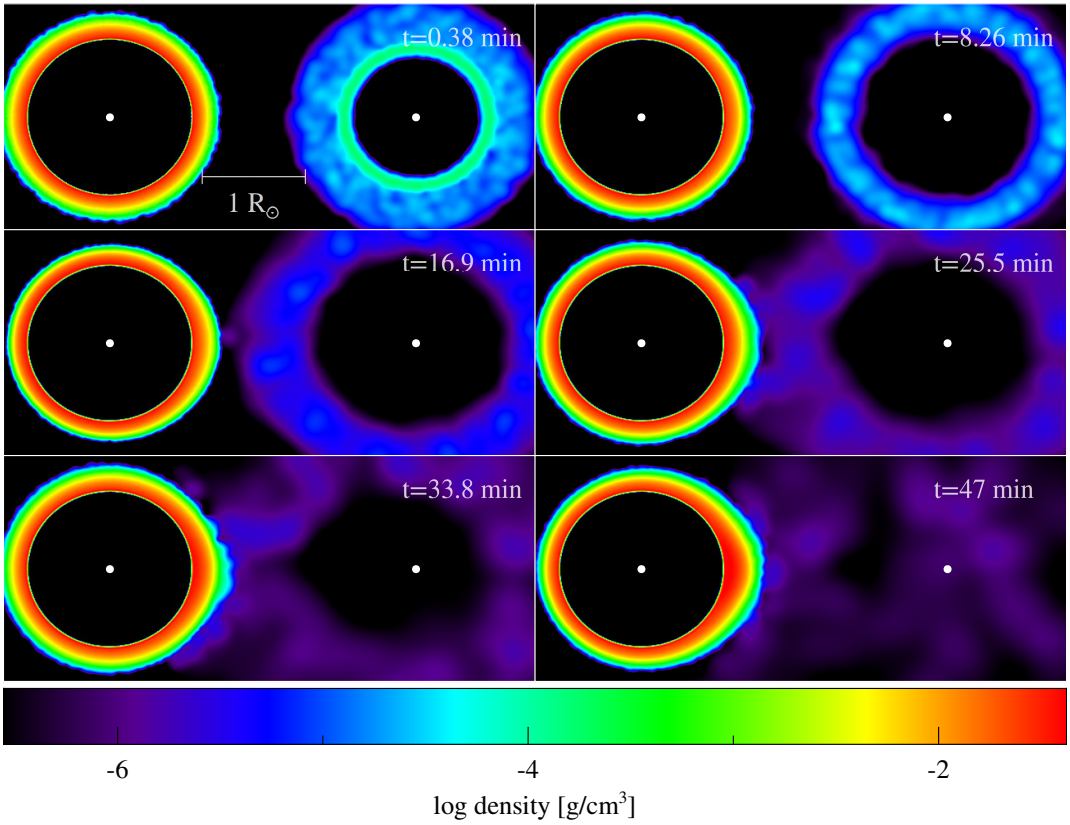

Figure 3.4: Same as Fig. 3.2, but for density plots corresponding to Model G at different times. In this model the accretion disk does not get totally swept up in the impact with the nova ejecta.

ever, in sharp contrast to the results reported in Section 3.2.2, the specific fractions depend significantly on the values adopted for the velocity of the ejecta (Table 3.2). For instance, the fraction of mass leaving the system increases from 60% to 89%, while the fractions that remain bound to the white dwarf or to the main sequence drop from 30% to 8%, and from 10% to 4%, respectively, when comparing Models D and I. Similar patterns are observed regardless of whether the disk gets disrupted or not (see, e.g., Models C, D and I, Models E and F, and Models G and J, for which different combinations of masses of the ejecta and disk have been adopted). Higher velocities for the nova ejecta drive, as expected, larger (but always tiny) amounts of mass lost by the main sequence companion; a maximum value of 2.4×10^{-6} $M_{\odot}$ is achieved in Model I.

It is worth mentioning that while the accretion disk is disrupted in Models A, B, E, and F, it survives the impact with the ejecta in all models characterized by moderately low $M_{\rm ejecta}/M_{\rm disk}$ ratios (e.g., Models C, D, I, and G, with $M_{\rm ejecta}/M_{\rm disk}$ ranging between 5.5 and 13). We note, however, that Model J, characterized by $M_{\rm ejecta}/M_{\rm disk} = 13$, results in disk disruption too. This is caused by the large kinetic energy and momentum carried by the impinging ejecta, which in this particular model expands with a maximum velocity of 3000 km s^{-1}.

3.2.4 Effect of the mass of the accretion disk

The mass of the accretion disk that orbits around the white dwarf is a poorly constrained quantity. Accordingly, we considered a series of disks with different masses, constructed in the framework of the Shakura & Sunyaev model. A comparison between Models A and C, for which two different values of the mass of the disk, $M_{\rm disk}$, were adopted (2×10^{-5} and 10^{-4} $M_{\odot}$, respectively) reveals, as mentioned before, that the lower the mass of the disk, the larger the probability of disruption. Hence, while the disk in Model A gets disrupted by the nova blast, it survives the impact in Model C. The same pattern is found for Models B and D, which are characterized by a lower expansion velocity of the nova ejecta (800 km s^{-1}), and Models K and G, for which a different geometry of the disk, with a larger H/R ratio, was assumed. Increasing the mass of the accretion disk reduces in turn the amount of mass lost by the binary system, and conversely increases the amount of mass that remains gravitationally bound to the white dwarf and main sequence companion[4].

The fraction of nova ejecta plus disk mass that escapes the binary system (or remains bound to the main sequence or to the white dwarf) follows the same pattern, and values show a clear dependence on the accretion disk mass.

3.2.5 Effect of H/R

So far, we analyzed the interaction of the nova ejecta with accretion disks characterized by a height to radius ratio of $H/R = 0.03$. However, observations increasingly support a dispersion in the value of H/R, within the range 0.03 – 0.1 (see Maccarone 2014; Shafter & Misselt 2006; Knigge *et al.* 2000). The influence of this parameter on the dynamical properties of the system was analyzed by means of Model K, in which a ratio of $H/R = 0.06$ was adopted for the accretion disk. Comparison between Model K and our fiducial Model A suggests that an increase in H/R has a similar effect as a reduction in the velocity of the expanding nova ejecta: here, a larger H/R results in an increase of the effective impact cross-section between disk and ejecta. This decelerates a larger portion of the ejecta, and as a result, the amount of mass gravitationally bound to the white dwarf and main sequence companion increases, while the overall mass lost from the binary system decreases. The fraction of nova ejecta plus disk mass that escapes the binary system (or remains bound to the main sequence or to the white dwarf) follows exactly the same trend. A thorough comparison between Models A and K reveals that the specific fractions depend significantly on the adopted H/R ratio (Table 3.2).

3.3 Chemical pollution of the secondary star

One of the possible outcomes of the dynamical interaction between the nova ejecta and main sequence companion is the pollution of the secondary, enhancing the metal content of its outer layers. The degree of contamination induced by the impact with the nova ejecta can be estimated from the overall number of particles gravitationally bound to the main sequence star (see, e.g., Lombardi *et al.* 2006). But this is by no means straightforward. On the one hand, the models presented in this Chapter follow the evolution of the binary system for

[4]However, Models K and G result in nearly identical ejected masses from the binary systems. This may partially result from the different geometry of the disks adopted and from the smaller range of values for the masses (a factor of 2 in Models G - K versus a factor of 5 in Models A - C and B - D).

about 3000 s, which corresponds to $\sim 0.1 P_{\rm orb}$. At this stage, a large number of particles gravitationally bound to the secondary are still orbiting around in a corona that surrounds the star. Even though such particles eventually fall into the star, it is difficult to anticipate how deep these particles penetrate into its envelope. Self-consistent calculations of these advanced stages would require a prohibitively intense computational effort for many orbital periods to compute the corresponding infalling trajectories. And even if such numerical simulations were feasible, a detailed account of the chemical profiles of the outer layers of the secondary would require the use of more realistic initial models for the main sequence star (see, e.g., Sills & Lombardi 1997) and the inclusion of important physical mechanisms that would be operating simultaneously (e.g., chemical diffusion and convection). This is clearly out of the scope of the present study. However, to illustrate the expected levels of chemical pollution, we provide some crude estimates of the compositional changes in the outer layers of the secondary at different mass depths, for Model A. Assuming that all the gravitationally bound particles still in orbit are incorporated and mixed with the outer 10^{-6} $M_{\odot}$ of the main sequence companion, a mean metallicity of $Z \sim 0.18$ is expected at those layers, in the hemisphere hit by the nova ejecta. The expected level of contamination obviously decreases when considering deeper layers (i.e., $Z \sim 0.036$ for 10^{-5} $M_{\odot}$, and $Z \sim 0.019$ for 10^{-4} $M_{\odot}$).

A final issue involves the relevance of these results in the framework of systems with low-mass secondaries ($M \leq 2$ $M_{\odot}$), in which the presence of a convective envelope may wash out any trace of chemical pollution induced by the impact with the nova ejecta. This aspect was addressed by Marks & Sarna (1998) and Marks *et al.* (1997), who analyzed the effect of re-accretion of material ejected during nova outbursts on the chemical evolution of the secondary, for binary systems with similar orbital periods and masses to those reported in this Chapter. The low-mass main sequence stars were evolved taking into account all major processes that may affect their surface composition as follows: nuclear reactions, mass loss, convection, thermohaline mixing, and contamination with the nova ejecta. Using a control model, where no nova ejecta was incorporated into the secondary, they reported elemental (e.g., C and N) and isotopic differences (^{12}C/^{13}C, ^{14}N/^{15}N, ^{16}O/^{17}O) on the surface layers of the secondary stars induced by the impact with the ejecta. Therefore, one may expect some effect on the next nova cycle, once mass transfer onto the white dwarf component resumes, even in binaries with low-mass secondaries. This aspect, however, deserves in-depth analysis.

3.4 Conclusions

We computed 11 3D SPH simulations of the interaction between the nova ejecta, the accretion disk, and the stellar companion aimed at testing the influence of the different parameters (i.e., mass and velocity of the ejecta and the mass and geometry of the accretion disk) on the dynamical and chemical properties of the binary system. The main conclusions reached in this Chapter are summarized as follows:

- We investigated the conditions leading to the disruption of the accretion disk that orbits the white dwarf star. In 7 out of the 11 models computed, the disk gets fully disrupted and swept up. In all these models, the disks are characterized by masses much smaller than that of the ejecta. Our simulations show that in models with V-shaped disks with height-to-radius ratios of $H/R = 0.03$ and $M_{\rm ejecta}/M_{\rm disk} \leq 5.5$ ($M_{\rm ejecta}/M_{\rm disk} \leq 13$, for $H/R = 0.06$) the disk survives the impact with the nova blast.

- Small amounts of mass, up to 1.4×10^{-6} $M_{\odot}$ are expelled from the outer main sequence

layers in the interaction with the nova ejecta. No ejection is reported from 2 out of the 11 models computed.

- An increase of the mass of the nova ejecta yields, in general, larger amounts of mass lost by the binary system, and larger masses gravitationally bound to the white dwarf and to the main sequence companion. The fraction of the overall mass available (i.e., ejecta plus disk) that escapes the binary system (or remains bound to the main sequence or to the white dwarf) does not depend much on the choice of the mass of the nova ejecta. However, the dynamics of the system is influenced by disk disruption when the increase of the mass of the nova ejecta modifies the stability of the disk, thereby moderately affecting the distribution of masses that remain gravitationally bound to the white dwarf or to the main sequence along with the amount of mass lost from the system. For instance, when comparing Models G (disk partially disrupted) and H (disk fully disrupted and swept up by the ejecta), the fraction of mass that leaves the binary system increases from 59% to 89%, while the fraction that remains bound to the white dwarf drops from 31% to 8%.

- An increase in the velocity of the ejecta results in larger ejected masses from the binary system, while reducing the amount of mass that remains gravitationally bound, either to the white dwarf or to the main sequence, regardless of whether the disk gets disrupted or not. This results from the larger kinetic energy and momentum carried by the impinging ejecta when its velocity is increased. The fraction of nova ejecta plus disk mass that escapes the binary system (or remains bound to the main sequence or to the white dwarf) follows exactly the same trend. The specific fractions depend much on the values adopted for the velocity of the ejecta. The large kinetic energy and momentum carried by the ejecta in models with $V_{ejecta}^{\max} = 3000$ km s^{-1} can lead to disk disruption even for models characterized by relatively low $M_{\rm ejecta}/M_{\rm disk}$ ratios, as in Model J.

- An increase of the mass of the accretion disk reduces the amount of mass lost by the binary system, and conversely, increases the amount of mass gravitationally bound to the white dwarf and to the main sequence companion. For instance, when comparing Models A ($M_{\rm disk} = 2.04 \times 10^{-5}\ M_\odot$) and C ($M_{\rm disk} = 9.28 \times 10^{-5}\ M_\odot$), the fraction of mass that leaves the binary system decreases from 88% to 67%, while the fractions that remain bound to the white dwarf and main sequence star increase from 9% to 25% and 4% to 8%, respectively. This results from the smaller kinetic energy and momentum transferred to the disk particles per unit mass when the mass of the disk is increased, which in turn reduces the probability of disk disruption by the nova blast.

- An increase in the height-to-radius ratio of the disk has similar effects to a reduction of the velocity of the expanding ejecta: the larger effective impact cross-section between disk and ejecta slows down a larger fraction of the nova ejecta, which in turn increases the mass gravitationally bound to the white dwarf and main sequence star, while reducing the overall mass lost by the binary system.

- A certain level of chemical contamination of the stellar secondary is induced by the impact with the nova ejecta; a mean metallicity of $Z \sim 0.18$ is estimated at the outer $10^{-6}\ M_\odot$ layers in the hemisphere hit by the ejecta, for Model A. This may have potential effects on the next nova cycle.

Chapter 4

U Sco - A Case Study of the Interaction Between the Nova Ejecta and its Environment, for a Recurrent Nova

As mentioned in Chapter 1, recurrent nova systems (hereafter, RNe) show a much wider range of orbital periods than classical novae. Three subgroups have been established (Anupama 2008), corresponding to long ($P_{\rm orb} \sim 1$ yr), intermediate-duration ($\sim$ hours to a day), and short orbital periods ($1 - 3$ hr).

A prototype of the subgroup with intermediate-duration orbital periods is U Scorpii (U Sco). These variables display rapidly declining light curves from maximum luminosity[1], and are characterized by much smaller ejected masses (by two orders of magnitude or more) and larger ejection velocities (up to 10000 km s^{-1}) than classical novae. The secondary star in this intermediate-duration RNe is either a main sequence or a subgiant star.

This Chapter is organized as follows. The main characteristics of U Scorpii are presented in Sect. 4.1. The input physics, and initial conditions adopted are described in Sect. 4.2. The effect of the rotation and the exploration of the parameter space is presented in Sect. 4.3. A summary of the most relevant conclusions of this Chapter is presented in Sect. 4.4.

4.1 Observational Properties of U Sco

U Sco, the third discovered recurrent nova, is one of the ~ 10 RNe discovered in the Milky Way[2] to date (Schaefer 2010). Located near the northern edge of the constellation Scorpius, at a distance of 12 ± 2 kpc from Earth (Schaefer 2010), it has been seen in outburst in

[1]Inferred values for the time required to drop 2 and 3 magnitudes from maximum brightness (i.e., t_2 and t_3, respectively) range between $t_2 = 1.2 - 1.7$ days and $t_3 = 2.6 - 3.6$ days (Schaefer 2010), implying the presence of a very massive white dwarf, near the Chandrasekhar limit.

[2]Several extragalactic recurrent novae have been discovered as well in the Andromeda Galaxy (M31) and in the Large Magellanic Cloud. One of these, M31N 2008-12a, erupts every 12 months (Nishiyama & Kabashima 2008).

1863, 1906, 1936, 1979, 1987, 1999, 2010, and 2022 (June 6), which corresponds to the most recent eruption[3]). The orbital period of U Sco is about 1.23 days (Schaefer 1990; Schaefer & Ringwald 1995). This relatively long orbital period, combined with the presence of a subgiant companion, suggests that accretion in this system may be driven by the expansion of the secondary star towards a red giant configuration, leading to a Roche lobe overflow[4]. This expansion drives a steady accretion at the high rates required to produce the short recurrence times reported from RNe.

- The companion star:

  The secondary is likely a subgiant star (spectral type between F8 and K2; see Hanes 1985; Schaefer 1990; Johnston & Kulkarni 1992; Anupama & Dewangan 2000), with a mass of 0.88 $M_\odot$ and a radius of $\sim 2.1\ R_\odot$ (Thoroughgood *et al.* 2001). With respect to the composition of the secondary, Maxwell *et al.* (2012) reported a He abundance in the ejecta of U Sco of N(He)/N(H) = 0.073 ± 0.031, concluding that the subgiant is not helium-rich, as other studies had previously suggested.

  It is also worth noting that mass transfer from the secondary star has been observed to resume about $\sim 8 - 10$ days since peak luminosity, after every outburst (Mason *et al.* 2012)[5].

- The primary star:

  The U Sco explosion is hosted by a massive white dwarf. Although the composition of primary remains undetermined (Mason 2013), different values for the mass of the primary have been reported in the literature: Anupama & Dewangan (2000) suggested $M_{wd} \geqslant 1.2\ M_\odot$. Dürbeck *et al.* (1993) reported a value of $M_{wd} \sim 1.16 \pm 0.69\ M_\odot$. Hachisu & Kato (2000) matched the quiescent light curve of U Sco assuming a white dwarf mass of $M_{wd} \sim 1.37\ M_\odot$, while Thoroughgood *et al.* (2001) suggested $M_{wd} \sim 1.55 \pm 0.24\ M_\odot$. Since the total mass of the system exceeds the Chandrasekhar limit of 1.4 $M_\odot$, U Sco is considered a possible SN Ia progenitor (Hachisu & Kato 2000; Livio 2000; Thoroughgood *et al.* 2001; Justham & Podsiadlowski 2008; Walder, R. *et al.* 2008; Walder *et al.* 2010). However, it is not clear whether the mass of the white dwarf in U Sco increases or decreases after each outburst (see, e.g., Schaefer 2011; Pagnotta *et al.* 2015).

- The accretion disk:

  Observationally, the presence of an optically-thick, flare-shaped disk has been inferred in U Sco, with a radius of about 2.2 $R_\odot$ (see Schaefer *et al.* 2011; Mason *et al.* 2012). Moreover, it has also been speculated that the disk may present a raised edge (Mason *et al.* 2012). Both the mass-accretion disk and the accretion stream appear to be blown away by the outburst in U Sco (Schaefer 2011)[6].

[3] The last outburst was predicted for the year 2020.7 ± 1.6 (Schaefer 2019). Two additional eruptions, in 1945 and 1969, have been suggested by some authors (see, e.g., Schaefer 2010).

[4] In other recurrent novae, such as in RS Ophiuchi, mass transfer is expected to result from the strong winds emitted from the red giant companion.

[5] See Mason *et al.* (2012), for additional observational properties of U Sco.

[6] See Drake & Orlando (2010), for multidimensional simulations of the effect of the outburst on the accretion disk.

The accretion stream is, in fact, the first structure expected to reappear after the outburst, on a freefall timescale[7], being limited by the wind continuing to blow away the infalling material. The outer edge of the reestablished accretion disk can only develop once the stream approaches the white dwarf surface (i.e., when the wind fades away). This outer edge will be formed on a timescale of the order of the orbital period of the system (Schaefer 2011). All in all, the accretion disk is expected to extend up to the inner Lagrangian point of the system, with a radius $R_{disk} = 4.21\ R_\odot$ during reformation (2.2 $R_\odot$ in quiescence; Schaefer 2011). Unfortunately, very little is known about the mass of the disk.

- The Nova ejecta:

  Multiwavelength observations of U Sco during its 2010 eruption (Pagnotta *et al.* 2015), combined with the empirical relation between ejected mass (M_{ejec}) and energy radiated during the explosion (Shara *et al.* 2010), yielded a value of $M_{ejec} \sim 2.1 \times 10^{-6}\ M_\odot$. Other studies, based on the variation of the orbital period in U Sco after an outburst, reported different values (e.g., $M_{ejec} \sim (4.3 \pm 6.7) \times 10^{-6}\ M_\odot$, for the 1999 outburst (Schaefer 2011), and $M_{ejec} \sim 2.5 \times 10^{-5}\ M_\odot$, for the 2010 outburst (Schaefer 2013))[8].

4.2 Model, input physics, and initial configuration

4.2.1 Model

As for the simulations reported in Chapter 3, the initial accretion, expansion, and ejection stages of U Sco have been modeled with the 1D, spherically symmetric, Lagrangian, hydrodynamic code `SHIVA` (see José & Hernanz 1998; José 2016, for details). When the inner edge of the ejecta reached a size of 0.08 $R_\odot$, the structure was mapped onto a 3D domain, which included the white dwarf star, the mass-accretion disk, and the secondary star. The evolution of the system was then followed with the 3D smoothed-particle hydrodynamics (SPH) code `GADGET-2` (Springel *et al.* 2001; Springel & Hernquist 2002; Springel 2005, see also Section 2.2, for an overview of the main properties of `GADGET-2`).

In the simulations reported in this Chapter, an orbital period of $P_{orb} = 29.53$ hr (1.23 days), characteristic of U Sco, has been adopted[9], such that the ejecta hit the secondary star just ~ 7 min since the beginning of the 3D simulations. Moreover, and in sharp contrast to the simulations reported in Chapter 3, rotation of this wider binary system has been considered, together with non-inertial forces (i.e., centrifugal and Coriolis forces; see Chapter 2).

4.2.1.1 The white dwarf star and the nova ejecta

The white dwarf is modeled as a 1.38 $M_\odot$ point-like mass, which is sufficient to account for the gravitational pull exerted on the overall system. The expanding nova ejecta, which at the beginning of the 3D simulations is located between 0.08 $R_\odot$ (inner edge) and 0.15 $R_\odot$ (outer edge) from the underlying white dwarf, has a mass of $2 \times 10^{-6}\ M_\odot$, a mean metallicity

[7] Observations suggest that an accretion stream reestablished about 15 days from the explosion in the 2010 U Sco outburst (see Schaefer *et al.* 2011).

[8] Other estimates include $M_{ejec} \sim 3 \times 10^{-6}\ M_\odot$ (Hachisu *et al.* 2000), and $M_{ejec} \sim 10^{-7}\ M_\odot$ (Anupama & Dewangan 2000).

[9] This period is $\sim$ 250 times longer than the time required for the ejecta to reach and hit the stellar secondary, at a speed of 10000 km s^{-1}.

of $Z = 0.011$, and a density and velocity profiles corresponding to the values obtained with the 1D code SHIVA.

4.2.1.2 The secondary star

A 0.88 $M_{\odot}$, solar metallicity, subgiant companion has been adopted as the secondary star. The structure of the secondary was computed by M. Salaris in spherical symmetry with the FRANEC code. At the time when the star enters the subgiant branch, it has a radius of about 2.2 $R_{\odot}$, and a luminosity of Log $L(L_{\odot}) \sim 0.343$ (Log $T_{eff} = 3.69$). The specific values adopted for the mass and radius of the star are in agreement with those inferred for the companion star in U Sco by Thoroughgood *et al.* (2001).

This structure was subsequently mapped onto a 3D particle distribution. As described in Chapter 3, to avoid a substantial computational load, only the outer layers of the star (i.e., the outer 0.0054 $M_{\odot}$, in this case) have been considered, since particles from the ejecta are not expected to penetrate deep inside the star. The remaining layers of the secondary have been replaced by a point-like mass located at the center of the star. To generate the initial 3D particle distribution (density) of the outer layers, a *glass* technique has been implemented (White 1996), as described in Chapter 2.3. The resulting density profile for the outer layers of the secondary star, after relaxation, is shown in Fig. 4.1. The radius of the star, after relaxation, corresponds to 2.37 $R_{\odot}$.

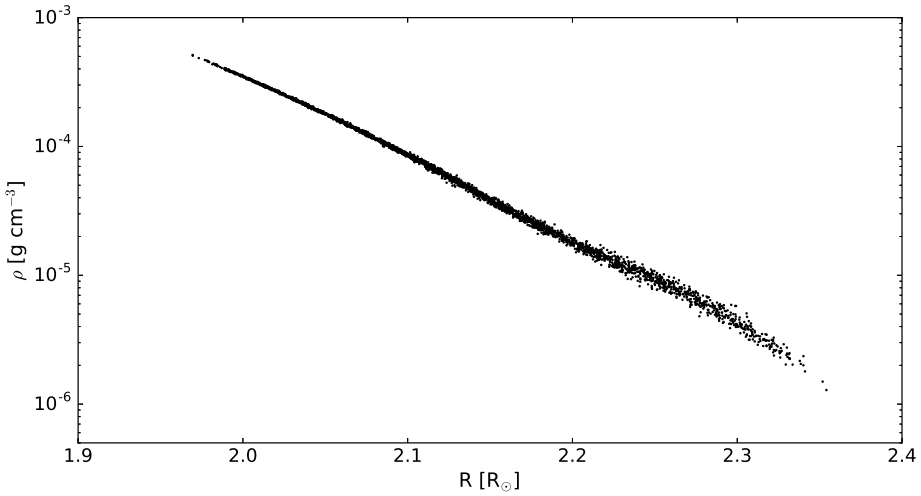

Figure 4.1: Density profile for the outer layers of the subgiant secondary star, after relaxation.

4.2.1.3 The mass-accretion disk

A flared accretion disk (see Fig. 4.2), that orbits the point-like white dwarf in Keplerian rotation, has been adopted following the prescription outlined by Hachisu *et al.* (2000). Estimates of the disk density have been obtained from the Shakura & Sunyaev (1973) model. In our fiducial model (hereafter, Model A), a solar-composition disk is adopted, with a mass

of 10^{-6} $M_{\odot}$ and a geometry given by:

$$H = \beta R_{disk} \left(\frac{d}{R_{disk}} \right)^{\nu} \tag{4.1}$$

where H represents the height of the disk from the equatorial plane, d is the distance from the center of the white dwarf, ν is an exponent related to the surface shape (taken as $\nu = 2$, following Hachisu *et al.* 2000[10]), and β is a parameter that indicates the degree of thickness of the disk (a value of $\beta = 0.3$ has been adopted, following once more Hachisu *et al.* 2000). The initial density profile for the mass-accretion disk is shown in Fig. 4.3.

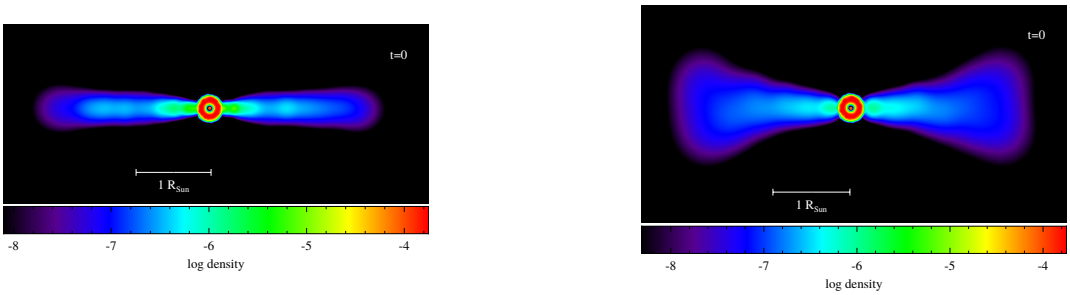

(a) A V-shaped disk.

(b) A Flared disk.

Figure 4.2: Different geometries for the mass-accretion disk.

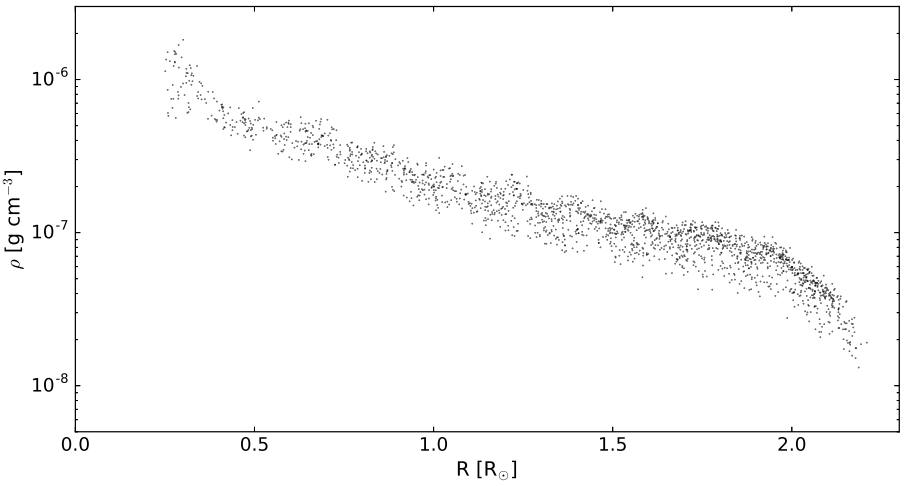

Figure 4.3: Initial density profile for the mass-accretion disk.

[10]The exact value of ν has no significant effect on the results, according to Hachisu *et al.* (2000).

4.2.2 Resolution

For convenience, and to guarantee a good accuracy in the interpolated functions, all SPH particles used in these simulations have the same mass, 5×10^{-10} $M_{\odot}$. About 9.77 million SPH particles have been used in the models reported in this Chapter, most of them (about 9.6 million) corresponding to the secondary star. The accretion disk contains only about 2000 SPH particles, while the nova ejecta contains about 3900 SPH particles, representing, as in Chapter 3, the limiting factor of the simulations.

4.2.3 Relaxation of the initial model

To guarantee that the 3D structure is in hydrostatic equilibrium, the system is relaxed before the simulations with `GADGET-2` begin. As in the models reported in Chapter 3, the stellar secondary is initially relaxed alone, for a time equivalent to 8 orbital periods. Here, however, a second relaxation stage has been implemented, in which the secondary is subsequently relaxed in the presence of the white dwarf star, for about 2 additional orbital periods. This guarantees better stability in the overall binary system, hence reducing the initial oscillations reported in the previous Chapter (see Chapter 2, for a full account of the binary relaxation procedure).

The sound-crossing time throughout the disk is ~ 5 hours, while the time required for the ejecta to reach and hit the disk is just ~ 16 seconds. Therefore, no relaxation of the disk, which has also been built through the *glass* technique, has been implemented.

4.3 Results

4.3.1 Effects of rotation. Test models

Table 4.1: Test models computed.

Model	$M_{\rm ejecta}$ ($M_{\odot}$)	$V_{\rm ejecta}^{\rm max}$ (km s^{-1})	$\rho_{\rm ejecta}$	$M_{\rm disk}$ ($M_{\odot}$)	Shape Disk	Rotation
A"	2.1×10^{-6}	10000	SHIVA	10^{-6}	Flared	No rotation
A'	2.1×10^{-6}	10000	SHIVA	10^{-6}	Flared	Centrifugal forces (only)
A	2.1×10^{-6}	10000	SHIVA	10^{-6}	Flared	Centrifugal forces + Coriolis

4.3.1.1 Evolution of Model A

Model A describes the interaction between $M_{\rm ejecta} = 2.1 \times 10^{-6}$ $M_{\odot}$, ejected from a 1.38 $M_{\odot}$ white dwarf during a recurrent nova outburst (with a maximum velocity of the ejecta of $V_{\rm ejecta}^{\rm max} = 10000$ km s^{-1}), and a 10^{-6} $M_{\odot}$ flared, accretion disk (Fig. 4.2), subsequently followed by the collision with a 0.88 $M_{\odot}$ subgiant companion (see Tables 4.1 and 4.2). The model is evolved in a co-rotating reference frame, and accordingly, includes Coriolis and centrifugal forces. Snapshots of the evolution of this model are shown in Fig. 4.4. A movie showing the time evolution of the density in Model A is available at `http://www.fen.upc.edu/users/jjose/Downloads.html`.

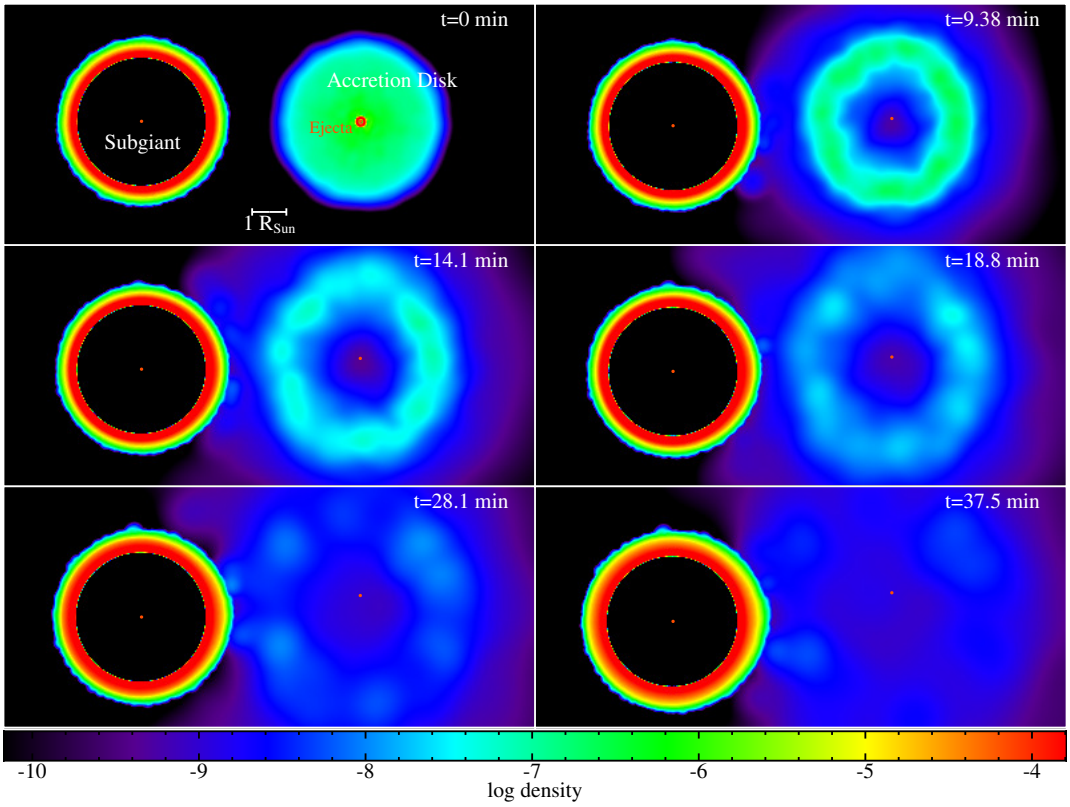

Figure 4.4: Cross-sectional slice in the binary orbital plane (XY) showing the density (in g/cm^3) of Model A at various stages of the interaction between the nova ejecta and the mass-accretion disk, subsequently followed by a collision with the subgiant stellar companion. A movie showing the full evolution of this model is available at `http://www.fen.upc.edu/users/jjose/Downloads.html`. Snapshots and movie were generated by means of the visualization software SPLASH (Price 2007).

The high ejection velocities force a fraction of the ejected plasma to hit the disk just ~ 16 s after the beginning of the simulation (Fig. 4.4, upper panels). The heat generated in this energetic collision rises the temperature of the disk to larger values than in the simulations reported in the previous Chapter. Here, an average temperature of $\sim 2.6 \times 10^7$ K is achieved in the disk that orbits the white dwarf, with with a few hundred particles (representing about 4% of the overall disk plus ejecta particles) exceeding 10^8 K. However, the low density of the plasma, $\sim 3 \times 10^{-5}$ g cm^{-3}, suggests that nuclear processing would not dramatically affect its composition.

Despite the wide orbit that characterizes U Sco, about 20% of the ejecta hits the mass-accretion disk ($m'_{\rm ejecta} \sim 20\% M_{\rm ejecta}$), with a mean kinetic energy, $K = \frac{1}{2} m'_{\rm ejecta} V^2_{\rm ejecta} \sim 4 \times 10^{44}$ ergs. This is due to the large cross-sectional area that results from the assumption of a flared geometry (see Fig. 4.2). The mean kinetic energy is slightly larger than the gravitational binding energy of the disk, $U \sim 3 \times 10^{42}$ ergs, estimated as $\sim G M_{\rm WD} M_{\rm disk} / r_{\rm mean}$, where G is the gravitational constant, $M_{\rm WD}$ is the mass of the underlying white dwarf, and $M_{\rm disk}$ and $r_{\rm mean}$ are the mass of the disk and the mean distance between the white dwarf

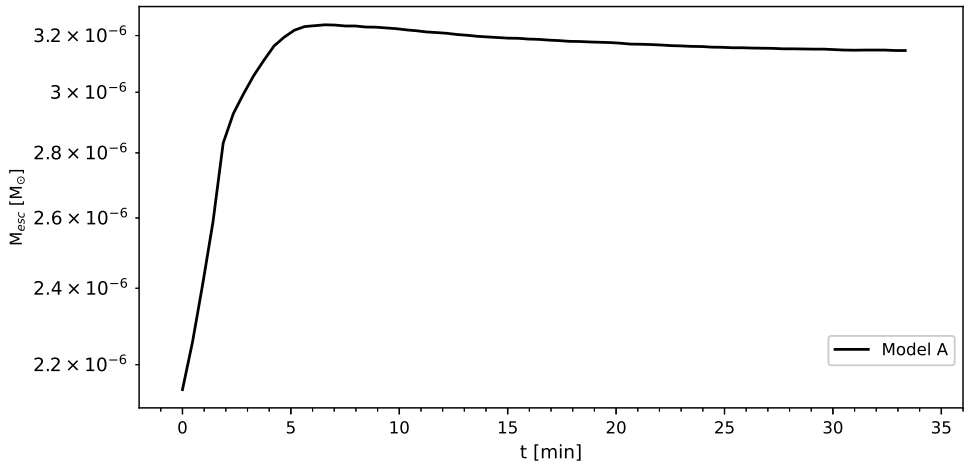

Figure 4.5: Time evolution of the mass leaving the binary system in Model A.

and the disk[11]. Accordingly, the disk gets fully disrupted in Model A.

At about $t \sim 7$ min (middle panels), a mixture of ejecta and disk material impinges upon the stellar companion. The temperature increases slightly in the outermost layers of the secondary, reaching a mean value of $\sim 3.5 \times 10^6$ K. While the energy released in the collision drives a moderate expansion of the outer layers of the star (lower panels), the temperatures achieved suggests that nuclear processing can be neglected.

About $\sim 3.14 \times 10^{-6}\ M_\odot$ ($\sim 97\%$ of the mixture of disk and nova ejecta) leave the binary system in Model A. In contrast, only $\sim 9.8 \times 10^{-7}\ M_\odot$ (about 3%) gets bound to the white dwarf (see Table 4.2). In the collision, only a handful of the ejecta/disk particles penetrate the outer layers of the secondary: in fact, only 4 SPH particles out of the 29 that impact the subgiant star (up to 37 minutes from the beginning of the simulation) are incorporated into the star; this represents a total mass of $2.2 \times 10^{-9} M_\odot$, or $\sim 0.07\%$ of the overall disk and nova ejecta, just a small amount (as expected from the large orbital period adopted, and hence, the large distance between the two stars, and from the large velocities and small masses that characterize the ejecta[12]). It is worth noting that the number of particles involved is not statistically significant. A detailed account of the contamination of the secondary would require a much larger number of SPH particles for the overall simulation, which will be addressed in the next Chapter.

Figure 4.5 shows the time evolution of the mass leaving the binary system in Model A. The early and sharp increase in mass loss ($t \leq 7$ min) results from the interaction between the nova ejecta and the disk, when the latter gets totally swept up and mixed with the former. The longer-term evolution of the mass loss reveals that little is expelled from the outer layers of the subgiant companion as a result of the impact with the nova ejecta. The

[11] A value of 2.12 $R_\odot$ (i.e., the outer radius of the disk) has been adopted for $r_{\rm mean}$. This choice clearly results in an overestimated value for the binding energy of the disk, which is still smaller than the mean kinetic energy of the ejecta.

[12] A similar pattern has been found in all the simulations reported in this Chapter.

small decline observed in M_{esc} is due to particles that marginally achieved escape velocity at some stage, and were later decelerated by interactions with the material orbiting the binary system.

4.3.1.2 Simulations with partial rotation or no rotation. Models A' and A"

As shown in Table 4.2, rotation tends to (slightly) decrease the number of particles (disk plus ejecta) bound to the white dwarf component of the binary system, while increasing the overall amount of mass lost by the system. Nevertheless, the differences between rotating and non-rotating models are really small for a wide system like U Sco. Larger differences are found, however, in the fraction of the mass lost by the subgiant that eventually becomes bound to (accreted by) the white dwarf, which decreases in model A, compared with the amount found in the non-rotating Model A".

4.3.2 Exploration of the parameter space

Bearing in mind the different parameter space that characterizes recurrent novae (i.e., lower ejected masses with much higher velocities, different densities) as well as the different shapes of the disk adopted, it is worth reanalyzing the phenomenology of the interaction between the ejecta, the accretion disk and the companion star for U Sco. Specifically, we will discuss the role played by the mass, the velocity and the density of the ejecta, as well as by the mass and shape (geometry) of the accretion disk, in the long-term evolution of the system (see Tables 4.3 and 4.4). It is worth noting that the accretion disk gets disrupted in models with flared disks and ratios $M_{\rm ejecta}/M_{\rm disk} \geq 1$ (i.e., Models A, B, C, D, G, and H). In contrast, the disk partially survives the nova blast in Model E, which is characterized by $M_{\rm ejecta}/M_{\rm disk} = 0.48$ (i.e., a massive disk). Note that the disk also survives the collision with the ejecta in Model F, characterized by a V-shaped disk and by a constant, high initial density (in sharp contrast to Model H, characterized also by a V-shaped disk, but with a density profile similar to the one depicted in Fig. 4.3).

4.3.3 Effect of the mass of the nova ejecta

Two values for the mass of the nova ejecta, $M_{\rm ejecta}$, have been considered to analyze the effect of this parameter on the simulations. As shown in Table 4.4, a comparison between our fiducial Model A (characterized by $M_{\rm ejecta} = 2.1 \times 10^{-6}\ M_{\odot}$) and Model B ($1.1 \times 10^{-6}\ M_{\odot}$) reveals that: increasing the mass of the ejecta, translates into higher mass escaping from the binary system, and in turn, lower mass remaining gravitationally bound to the white dwarf. This is in sharp contrast to the results obtained in the simulations reported in Chapter 3. Here, the extreme velocities adopted for the ejecta, with $V_{\rm ejecta}^{\rm max} = 10000$ km s^{-1}, are high enough to guarantee that a significant fraction of the disk and ejecta mass will still exceed escape velocity from the system after the collision. This affects as well the late-time interaction between the disk and ejecta with the subgiant secondary. Indeed, Table 4.4 reveals a decrease in the amount of mass ejected from the system by the secondary, $\Delta M_{\rm SS,lost}$, as well as a decrease in the fraction of mass accreted by the white dwarf, $\Delta M_{\rm SS,WD}$, as the mass of the ejecta increases.

Table 4.2: Mass (ejecta plus disk) gravitationally bound to the white dwarf, $\Delta M_{\rm WD}$, and total mass leaving the binary system, $\Delta M_{\rm esc}$, together with their fractions (in %) over the total ejecta plus disk masses, after collision with the nova ejecta. $\Delta M_{\rm MS,lost}$ is the mass lost from the system by the secondary star in the interaction with the nova ejecta, while $\Delta M_{\rm MS,WD}$ is the mass of the secondary that gets accreted by the white dwarf.

Model	$\Delta M_{\rm WD}$ ($M_\odot$)	$\Delta M_{\rm esc}$ ($M_\odot$)	$\frac{\Delta M_{\rm WD}}{(M_{\rm ejecta}+M_{\rm disk})}$	$\frac{\Delta M_{\rm esc}}{(M_{\rm ejecta}+M_{\rm disk})}$	$\Delta M_{\rm MS,lost}$ ($M_\odot$)	$\Delta M_{\rm MS,WD}$ ($M_\odot$)	Disk disruption
A"	1.08×10^{-7}	3.13×10^{-6}	3.34%	96.66%	3.85×10^{-9}	7.44×10^{-7}	Yes
A'	9.40×10^{-8}	3.15×10^{-6}	2.90%	97.10%	3.30×10^{-9}	5.59×10^{-7}	Yes
A	9.84×10^{-8}	3.14×10^{-6}	3.04%	96.96%	5.5×10^{-10}	5.92×10^{-7}	Yes

Table 4.3: U Sco Models computed.

Model	$M_{\rm ejecta}$ ($M_\odot$)	$V_{\rm ejecta}^{\rm max}$ (km s^{-1})	$\rho_{\rm ejecta}$	$M_{\rm disk}$ ($M_\odot$)	Shape Disk
A	2.1×10^{-6}	10000	SHIVA	10^{-6}	Flared
B	1.1×10^{-6}	10000	SHIVA	10^{-6}	Flared
C	2.1×10^{-6}	5000	SHIVA	10^{-6}	Flared
D	2.1×10^{-6}	2000	SHIVA	10^{-6}	Flared
E	2.1×10^{-6}	10000	SHIVA	4.4×10^{-6}	Flared
F	2.1×10^{-6}	10000	Const.	10^{-6}	V-Shaped
G	2.1×10^{-6}	10000	Const.	10^{-6}	Flared
H	2.1×10^{-6}	10000	SHIVA	10^{-6}	V-Shaped

Table 4.4: Mass (ejecta plus disk) gravitationally bound to the white dwarf, $\Delta M_{\rm WD}$, and total mass leaving the binary system, $\Delta M_{\rm esc}$, together with their fractions (in %) over the total ejecta plus disk masses, after collision with the nova ejecta. $\Delta M_{\rm SS,lost}$ is the mass lost from the system by the secondary star in the interaction with the nova ejecta, while $\Delta M_{\rm SS,WD}$ is the mass of the secondary that gets accreted by the white dwarf.

Model	$\Delta M_{\rm WD}(M_\odot)$	$\Delta M_{\rm esc}(M_\odot)$	$\frac{\Delta M_{\rm WD}}{(M_{\rm ejecta}+M_{\rm disk})}$	$\frac{\Delta M_{\rm esc}}{(M_{\rm ejecta}+M_{\rm disk})}$	$\Delta M_{\rm SS,lost}(M_\odot)$	$\Delta M_{\rm SS,WD}(M_\odot)$	Disk disruption
A	9.84×10^{-8}	3.14×10^{-6}	3.04%	96.96%	5.5×10^{-10}	5.92×10^{-7}	Yes
B	1.61×10^{-7}	2.14×10^{-6}	7.01%	92.99%	1.1×10^{-9}	2.37×10^{-6}	Yes
C	1.92×10^{-7}	3.05×10^{-6}	5.94%	94.06%	2.75×10^{-9}	1.93×10^{-6}	Yes
D	2.96×10^{-7}	2.95×10^{-6}	9.14%	90.86%	1.1×10^{-9}	2.01×10^{-6}	Yes
E	1.95×10^{-6}	4.58×10^{-6}	29.87%	70.13%	1.58×10^{-8}	2.22×10^{-6}	Partially
F	8.69×10^{-7}	2.35×10^{-6}	26.97%	73.03%	3.85×10^{-8}	9.41×10^{-7}	Partially
G	3.46×10^{-7}	2.89×10^{-6}	10.72%	89.28%	–	5.35×10^{-7}	Yes
H	5.21×10^{-7}	2.71×10^{-6}	16.12%	83.88%	8.3×10^{-8}	1.04×10^{-6}	Yes

4.3.4 Effect of the velocity of the ejecta

Three values for the maximum velocity of the ejecta, $V_{\rm ejecta}^{\rm max}$, characteristic of recurrent nova systems, have been adopted to analyze the influence of this parameter: 2000 km s^{-1} (Model D), 5000 km s^{-1} (Model C), and 10000 km s^{-1} (Model A). As shown in Table 4.4, an increase in the velocity of the ejecta reduces the amount of mass that remains gravitationally bound to the white dwarf (i.e., 9% of the disk and ejecta mass in Model D, 6% in Model C, and 3% in Model A), while increasing the mass lost from the binary system (91% in Model D, 94% in Model C, and 97% in Model A).

However, the effect of the velocity of the ejecta on the fate of the particles ejected by the subgiant companion after being hit by the nova blast is not clearly shown in the simulations reported in this Chapter: while the mass that gets accreted by the white dwarf seems to monotonically decrease when considering larger velocities of the ejecta, no clear pattern is found for the mass that leaves the system, which achieves a maximum value of $\Delta M_{\rm SS,lost} = 2.75 \times 10^{-9}\ M_{\odot}$ for Model C[13].

4.3.5 Effect of the density of the ejecta

To test whether the specific density of the ejecta has an overall effect on the simulations, a model with a flared disk and constant density of the ejecta ($\rho_{\rm ejec} = 1.8 \times 10^{-4}$ g cm^{-3}; hereafter, Model G) has been compared with our fiducial Model A, characterized by an ejecta with a density profile ranging from $\rho_{\rm ejec} = 7.9 \times 10^{-5}$ g cm^{-3} (outermost layers) and $\rho_{\rm ejec} = 1.9 \times 10^{-4}$ g cm^{-3} (innermost layers), as calculated with the 1D, hydrodynamic code `SHIVA`. A close inspection of Table 4.4 reveals that the larger, constant density adopted in Model G results in the deceleration of a larger number of particles during the collision with the disk. This translates into a larger amount of mass bound to the white dwarf star (which rises from 3% of the total disk and ejecta mass in Model A to 11% in Model G), and conversely, a decrease in the overall mass ejected from the binary system (97% in Model A, 89% in Model G).

Moreover, the subsequent impact with the subgiant companion shows a decrease in the number of particles ejected from the secondary star that leave the system (which drops to zero in Model G). A small decrease in the amount of mass of the secondary that gets ultimately accreted by the white dwarf is also obtained.

Identical patterns are also reported from the V-shaped disk Models H (with a disk characterized by a density profile) and F (disk with a constant density that partially survives the impact with the ejecta).

4.3.6 Effect of the mass of the accretion disk

The mass of the accretion disk deeply affects the long-time evolution of the binary system. Comparison between Models A and E, for which two different values of the mass of the disk have been adopted, $M_{\rm disk} = 2.1 \times 10^{-6}\ M_{\odot}$ and $4.4 \times 10^{-6}\ M_{\odot}$, respectively, reveals that a lighter disk increases the probability of disruption, as expected. Hence, while the disk in Model A gets fully disrupted by the nova blast, it (partially) survives the collision in Model E (see Fig. 4.6). Moreover, the larger mass of the disk in Model E reduces the percentage

[13] It is worth noting, however, that some of the values of $\Delta M_{\rm SS,lost}$ listed in Table 4.4 are very small, and hence, involve only a handful of particles. Better resolution is probably needed to clarify certain dependencies.

of mass lost by the binary system (70% of the total disk and ejecta in Model E, while 97% in Model A[14]), and conversely, increases the amount of mass that remains gravitationally bound to the white dwarf (30% in Model E, 3% in Model A). Finally, the amount of disk and ejecta mass that remains in the system, a fraction of which ultimately impacts the secondary star, results in a larger amount of mass ejected from the subgiant in Model E, which either leaves the system or remains bound to the white dwarf (also in larger amounts for Model E).

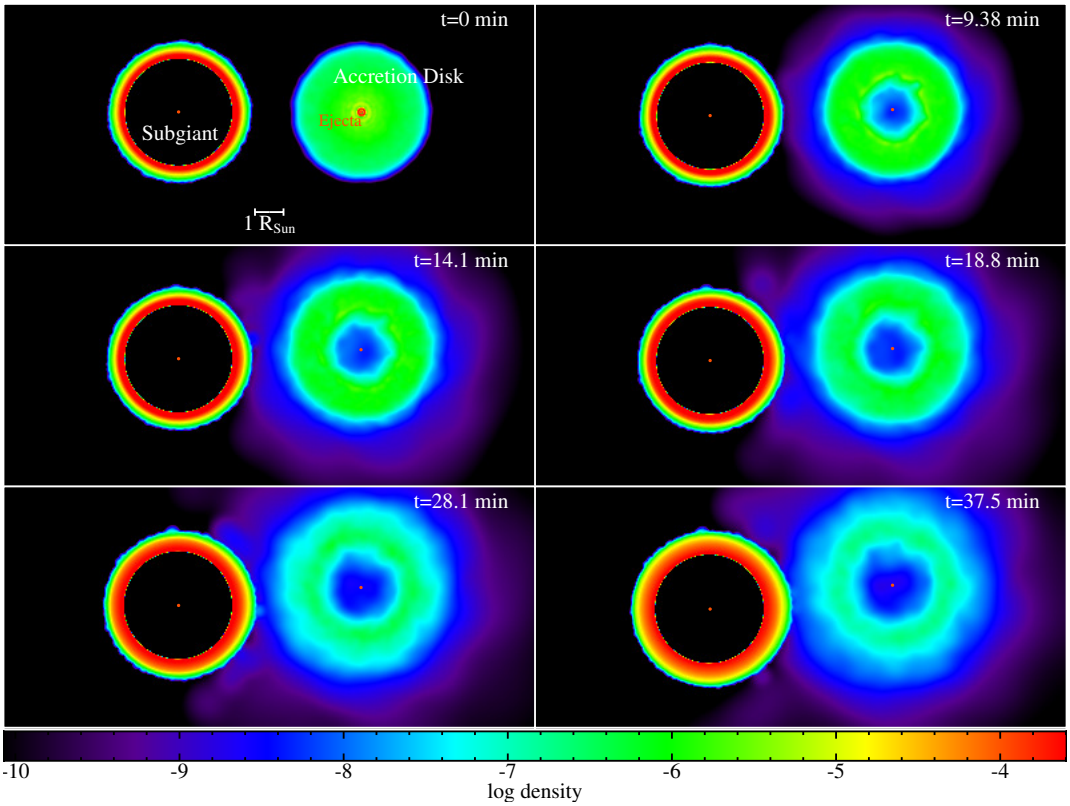

Figure 4.6: Same as Fig. 4.4, but for density (in g/cm^3) plots corresponding to Model E at different times. Note that in this model the accretion disk does not get totally swept up in the impact with the nova ejecta. Snapshots and movie have been generated by means of the visualisation software SPLASH (Price 2007).

4.3.7 Effect of the shape (geometry) of the disk

The specific shape adopted for the disk (i.e., flared vs. V-shaped; see Fig. 4.2) influences the cross-sectional area of the disk that is hit by the incoming nova ejecta. To quantify this effect, we have compared the results of two nearly identical models, Model A (with a flared disk) and Model H (in which a V-shaped disk has been adopted). The more extended

[14]Note, however, that the overall mass lost in Model E, 4.58×10^{-6} M$_\odot$, is larger than that in Model A, 3.14×10^{-6} M$_\odot$. This results from the fact that the disk adopted in Model E is 4.4 times more massive than that in Model A.

V-shaped disk tends to interact (i.e., slow down) with a larger fraction of the ejecta, thus reducing the overall mass loss from the binary system (i.e., 97% of the total disk and ejecta mass in Model A, 84% in Model H), while increasing the mass that remains gravitationally bound to the white dwarf (3% in Model A, and 16% in Model H).

The larger amount of the disk and ejecta mass that remains trapped in the binary system in Model H increases in turn the number of particle collisions with the secondary star. This translates into a larger amount of mass ejected from the outer layers of the subgiant companion, increasing both the mass that leaves the system ($\Delta M_{\rm SS,lost} = 8.3 \times 10^{-8}$ $M_\odot$ for Model H, 5.5×10^{-10} $M_\odot$ for Model A), and the amount that remains bound to the white dwarf ($\Delta M_{\rm SS,WD} = 10^{-6}$ $M_\odot$ for Model H, 5.9×10^{-7} $M_\odot$ for Model A).

Identical patterns have been found in the comparison between Model G (with a flared disk) and Model F (V-shaped disk), in which the disks are assumed to have a constant initial density. The effect of the different shape adopted for the disks is, in the case of these models, magnified by the survival of the disk after the impact with the nova blast in Model F.

4.4 Conclusions

The different parameter space that characterizes recurrent and classical novae (i.e., different masses, densities and velocities of the ejecta, as well as different shapes and densities of the disks adopted), motivated a reanalysis of the interaction between the ejecta, the accretion disk and the companion star for the case of U Sco, a well-studied Galactic recurrent nova. To that end, we computed 10 new 3D SPH simulations aimed at testing the influence of the different parameters (i.e., mass, velocity, and density of the ejecta, mass and geometry of the accretion disk) on the dynamical properties of the binary system. Rotation of the stars around the center-of-mass of the system, together with non-inertial forces (i.e., centrifugal and Coriolis forces), have been included in the simulations reported in this Chapter. The main conclusions reached are summarized as follows:

- Rotation tends to decrease the number of disk plus ejecta particles that remain bound to the white dwarf component of the binary system, while increasing the overall amount of mass lost by the system. The differences observed between rotating and non-rotating models are, however, very small for a wide system (i.e., larger orbital period) like U Sco. Larger differences are reported in the amount of mass lost by the subgiant companion that eventually becomes accreted by the white dwarf, which decreases in our fiducial, full rotating Model A, compared with the values found in the non-rotating Model A".

- We investigated the conditions leading to the disruption of the accretion disk that orbits the white dwarf star in a recurrent nova system. In 6 out of 8 models computed, the disk gets fully disrupted and swept up. These models are characterized by flared disks and ratios $M_{\rm ejecta}/M_{\rm disk} \geq 1$ (i.e., Models A, B, C, D, G, and H). In contrast, in Model E, for which a more massive disk was adopted ($M_{\rm ejecta}/M_{\rm disk} = 0.48$), the disk partially survived the collision with the ejecta. The same pattern was found in Model F, characterized by a V-shaped disk and by a constant, high initial density.

- A small amount of mass from the outer layers of the subgiant secondary are expelled during the late-time interaction with the ejecta plus disk plasma. Part of this material is ejected from the binary system (in most of the models), and part accreted by the white dwarf star.

- An increase of the mass of the nova ejecta leads to higher amounts of mass escaping from the binary system, and in turn, lower mass remaining gravitationally bound to the white dwarf. This is in sharp contrast to the results obtained in the simulations reported in Chapter 3, and are driven by the extreme velocities adopted for the ejecta, with $V_{\rm ejecta}^{\rm max} = 10000$ km s^{-1}, high enough to guarantee that a significant fraction of the disk and ejecta will still exceed escape velocity from the system after the collision.

- An increase in the velocity of the ejecta results in larger ejected masses from the binary system, while reducing the amount of mass that remains gravitationally bound to the white dwarf. The specific fractions depend much on the values adopted for the velocity of the ejecta.

- The larger, constant density adopted for the ejecta in Model G results in the deceleration of a larger number of particles during the collision with the disk, when compared with Model A, characterized by an ejecta with a density profile that decreases with the distance to the white dwarf. This translates into a larger amount of mass bound to the white dwarf star, and conversely, a decrease in the overall mass ejected from the binary system.

- An increase of the mass of the accretion disk increases the probability of disk survival after the collision with the ejecta, as shown in Model E. In turn, models with more massive disks result in a reduction of the percentage of mass lost from the binary system, and conversely, increase the amount of mass that remains gravitationally bound to the white dwarf.

- The adoption of a extended V-shaped disk forces a larger fraction of the ejecta to slow down after the collision, compared with the results obtained for a compact, flared disk geometry, thus reducing the overall mass loss from the binary system, while increasing the mass that remains gravitationally bound to the white dwarf.

- A very minor chemical contamination of the stellar secondary is induced by the impact with the nova ejecta in the case of U Sco, based on the small number of particles that ultimately hit the subgiant star.

Chapter 5

Further Exploration of the Parameter Space

For completeness, a number of additional models, aimed at testing the effect of additional parameters (e.g., the orbital period or the white dwarf mass) on the long-term evolution of a cataclysmic variable system, are presented in this Chapter (see Table 5.1). The influence of some other parameters (e.g., the mass and geometry of the disk, the mass and velocity of the ejecta) are also reanalyzed under different conditions.

This Chapter is organized as follows. The input physics, and initial conditions adopted are described in Sect. 5.1. In Sect. 5.2 the exploration of the parameter space is presented. Finally, a summary of the most relevant conclusions of this Chapter is presented in Sect. 5.3.

5.1 Model, input physics, and initial configuration

5.1.1 Model

As for the simulations reported in previous chapters, the initial accretion, expansion, and ejection stages of the nova explosion have been modeled with the 1D, spherically symmetric, Lagrangian, hydrodynamic code `SHIVA` (see José & Hernanz 1998; José 2016, for details). When the inner edge of the ejecta reached a size of 0.084 $R_{\odot}$, the structure was mapped onto a 3D domain, which included the white dwarf star, the mass-accretion disk, and the secondary star. The evolution of the system was then followed with the 3D smoothed-particle hydrodynamics (SPH) code `GADGET-2` (Springel *et al.* 2001; Springel & Hernquist 2002; Springel 2005, see also Section 2.2). All the simulations reported in this Chapter have been evolved in a co-rotating reference frame, and accordingly, include non-inertial forces (i.e., centrifugal and Coriolis forces; see Chapter 2).

5.1.2 Model 1

Model 1 is a representative model of a cataclysmic variable system. It is adopted as the fiducial model in this Chapter.

Table 5.1: Additionl models of cataclysmic binary systems computed.

Model	$M_{\rm WD}$ ($M_\odot$)	$M_{\rm MS}$ ($M_\odot$)	$M_{\rm ejecta}$ ($M_\odot$)	$V_{\rm ejecta}^{\rm max}$ (km s^{-1})	$\rho_{\rm ejecta}$	$M_{\rm disk}$ ($M_\odot$)	Shape Disk	Orbital Period (hour)
1	0.6	0.66	2.1×10^{-4}	1200	SHIVA	2.04×10^{-6}	V-Shaped	6.38
2	0.6	0.66	2.1×10^{-4}	1200	SHIVA	2.04×10^{-6}	Flared	6.38
3	0.6	0.66	2.1×10^{-4}	1200	SHIVA	1.02×10^{-6}	V-Shaped	6.38
4	1.25	0.66	2.1×10^{-4}	1200	SHIVA	2.04×10^{-6}	V-Shaped	6.38
5	0.6	0.66	2.1×10^{-4}	1200	SHIVA	2.04×10^{-6}	V-Shaped	12.76
6	1.25	0.66	2.1×10^{-5}	4800	SHIVA	2.04×10^{-6}	V-Shaped	6.38

Table 5.2: Mass (ejecta plus disk) gravitationally bound to the secondary, $\Delta M_{\rm MS}$, and the white dwarf, $\Delta M_{\rm WD}$, and total mass leaving the binary system, $\Delta M_{\rm esc}$, together with their fractions (in %) over the total ejecta plus disk masses, after collision with the nova ejecta. $\Delta M_{\rm SS,lost}$ is the mass lost from the system by the secondary star in the interaction with the nova ejecta.

Model	$\Delta M_{\rm MS}$ ($M_\odot$)	$\Delta M_{\rm WD}$ ($M_\odot$)	$\Delta M_{\rm esc}$ ($M_\odot$)	$\frac{\Delta M_{\rm MS}}{(M_{\rm ejecta}+M_{\rm disk})}$	$\frac{\Delta M_{\rm WD}}{(M_{\rm ejecta}+M_{\rm disk})}$	$\frac{\Delta M_{\rm esc}}{(M_{\rm ejecta}+M_{\rm disk})}$	Disk disruption	$\Delta M_{\rm SS,lost}$ ($M_\odot$)
1	8.99×10^{-6}	1.38×10^{-4}	6.22×10^{-5}	4.30%	65.90%	29.80%	Yes	6.60×10^{-9}
2	9.11×10^{-6}	9.98×10^{-5}	9.99×10^{-5}	4.36%	47.79%	47.85%	Yes	7.20×10^{-9}
3	7.26×10^{-6}	1.37×10^{-4}	6.38×10^{-5}	3.49%	65.82%	30.69%	Yes	5.00×10^{-9}
4	2.00×10^{-9}	2.03×10^{-4}	5.99×10^{-6}	0.001%	97.13%	2.87%	Yes	2.00×10^{-10}
5	0.00	1.32×10^{-4}	7.71×10^{-5}	0.00%	63.08%	36.92%	Yes	0.00
6	2.26×10^{-8}	1.02×10^{-6}	2.17×10^{-5}	0.10%	4.47%	95.43%	Yes	2.38×10^{-8}

5.1.2.1 The white dwarf star and the nova ejecta

The white dwarf star is modeled as a 0.6 $M_\odot$ point-like mass. As in previous chapters, this is enough to account for the gravitational pull exerted on the overall system. The expanding nova ejecta, which at the beginning of the 3D SPH simulations is located between 0.084 $R_\odot$ (inner edge) and 0.143 $R_\odot$ (outer edge) from the underlying compact star, has a mass of 2×10^{-4} $M_\odot$, a mean metallicity of $Z = 0.54$, and a density and velocity profiles corresponding to the values computed with the 1D code `SHIVA`.

5.1.2.2 The main sequence, secondary star

A 0.66 $M_\odot$, solar metallicity, main sequence companion has been adopted as the secondary star. The structure of the secondary was obtained assuming spherical symmetry and hydrostatic equilibrium conditions. To that end, a polytropic equation of state with $\gamma = 5/3$ was considered. The star has a radius of about 0.65 $R_\odot$. This structure was subsequently mapped onto a 3D particle distribution. As in previous chapters, to reduce the computational load, only the outer layers of the star (i.e., the outer 0.0030 $M_\odot$, in this case) have been considered, since particles from the ejecta are not expected to penetrate deep inside the secondary star. The rest of the star has been replaced by a point-like mass located at its center. As in previous chapters, a *glass* technique (White 1996) has been used to generate the initial 3D particle distribution (density) for the main sequence. The resulting density profile is shown, after relaxation, in Fig. 5.1. The radius of the secondary star, in this relaxed configuration, is 0.7 $R_\odot$.

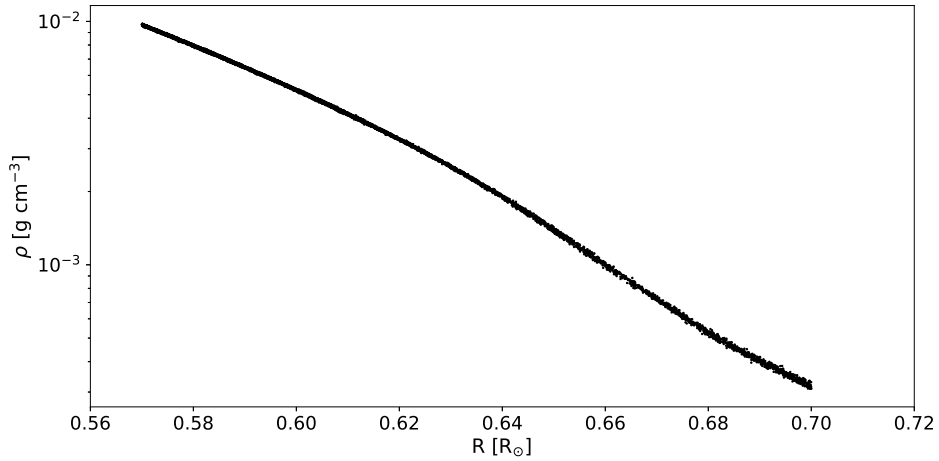

Figure 5.1: Density profile for the outer layers of the main sequence, secondary star, after relaxation.

5.1.2.3 Orbital period

The white dwarf star and the main sequence companion are assumed to orbit around the center-of-mass of the binary system with an orbital period of $P_{\rm orb} = 6.38$ hr[1]. The system is subsequently evolved in a co-rotating reference frame, and non-inertial forces (i.e., centrifugal and Coriolis forces) have been considered.

5.1.2.4 The mass-accretion disk

A V-shaped accretion disk that orbits the point-like white dwarf in Keplerian rotation, has been adopted following the prescription outlined by Shakura & Sunyaev (1973) and Frank *et al.* (2002)[2]. In our fiducial Model 1, a solar-composition disk is adopted, with a mass of 2×10^{-6} $M_\odot$ and a geometry given by the ratio of height to radius, H/R = 0.03. The initial density profile for the mass-accretion disk is shown in Fig. 5.2.

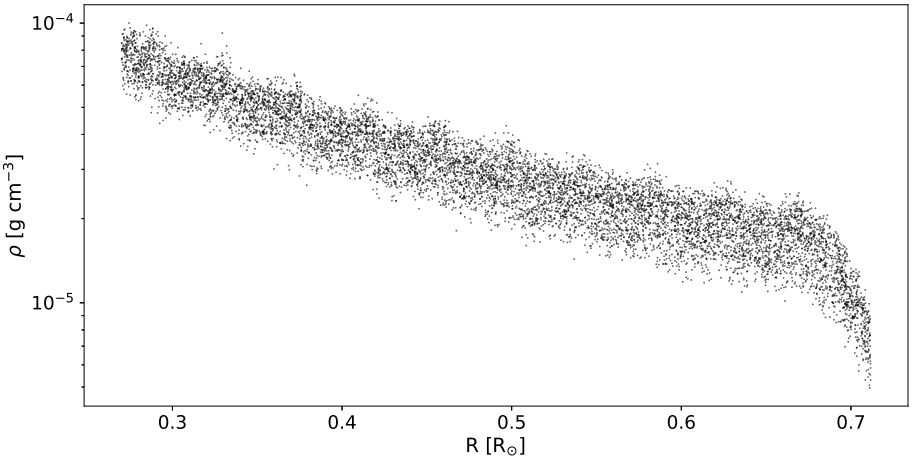

Figure 5.2: Initial density profile for the mass-accretion disk.

5.1.3 Resolution

As in previous chapters, and to guarantee a good accuracy in the interpolated functions, all SPH particles used in these simulations have the same mass, 2×10^{-10} $M_\odot$. About 15.8 million SPH particles have been used in the models reported in this chapter, most of them (about 14.8 million) associated to the main sequence star. The accretion disk contains about 10000 SPH particles, while the nova ejecta contains about 1 million SPH particles, improving the resolution with respect to previous chapters.

[1]This period is $\sim$ 21 times longer than the time required for the ejecta to reach and hit the stellar secondary, at a speed of 1200 km s^{-1}.

[2]See also Chapter 4, for a comparison between flared and V-shaped disks.

5.1.4 Relaxation of the initial model

To guarantee that the 3D structure fulfills hydrostatic equilibrium, the system is relaxed prior to the simulations with `GADGET-2`. Here, we adopted the same methodology implemented in Chapter 4, beginning with the relaxation of the stellar secondary alone, for a time equivalent to 5 orbital periods. This was followed by a second relaxation stage, in which the secondary is relaxed in the presence of the white dwarf star, for about 2 additional orbital periods. This methodology improves the stability of the overall binary system, and as discussed in Chapter 4, efficiently contributed to reduce the initial oscillations of the simulations reported in Chapter 3, in which only the first relaxation stage was implemented. The sound-crossing time throughout the disk is ~ 8 hours for Model 1, while the time required for the ejecta to reach and hit the disk is just ~ 0.6 seconds. Therefore, no relaxation of the disk, which has also been built through the *glass* technique, has been implemented.

5.2 Results

5.2.1 Evolution of Model 1

A movie showing the time evolution of the density in Model 1 is available at `http://www.fen.upc.edu/users/jjose/Downloads.html`. Snapshots of the evolution of this model are shown in Fig. 5.3. In this model, the nova ejecta hits the disk just ~ 0.6 s after the beginning of the simulation. The heat generated in this collision rises slightly the temperature of the disk to an average temperature of $\sim 2.5 \times 10^6$ K, with just $\sim 10\%$ of the particles reaching a maximum temperature of $\sim 1.8 \times 10^7$ K. The moderate maximum temperature, combined with the low density of the plasma, $\sim 1.3 \times 10^{-3}$ g cm^{-3}, suggests that nuclear processing can be neglected (Fig. 5.3, upper panels).

In this model, about 14% of the ejecta hits the mass-accretion disk ($m'_{\rm ejecta} \sim 14\% M_{\rm ejecta}$), with a mean kinetic energy, $K = \frac{1}{2} m'_{\rm ejecta} V^2_{\rm ejecta} \sim 6 \times 10^{42}$ ergs. Here, the mean kinetic energy is quite similar than the gravitational binding energy of the disk, $U \sim 7 \times 10^{42}$ ergs, estimated as $\sim G M_{\rm WD} M_{\rm disk}/r_{\rm mean} \sim$, where G is the gravitational constant, $M_{\rm WD}$ is the mass of the underlying white dwarf, and $M_{\rm disk}$ and $r_{\rm mean}$ are the mass of the disk and the mean distance between the white dwarf and the disk[3]. While the crude estimates used for the mean kinetic energy and gravitational binding energy yield similar values, the disk gets eventually disrupted in Model 1[4].

At about $t \sim 18$ min (middle panels), a mixture of ejecta and disk material impinges upon the stellar companion. The temperature increases slightly in the outermost layers of the secondary, reaching a mean value of only $\sim 5.8 \times 10^4$ K. While the energy released in the collision drives a moderate expansion of the outer layers of the star (lower panels), the temperatures achieved allow us to neglect again nuclear processing.

Only $\sim 6.22 \times 10^{-5}$ $M_\odot$ ($\sim 30\%$ of the mixture of disk and nova ejecta) leave the binary system in Model 1. In contrast, $\sim 1.38 \times 10^{-4}$ $M_\odot$ (about 66%) gets bound to the white dwarf (see Table 5.2). In the collision, some ejecta/disk particles manage to penetrate the outer layers of the secondary, $\sim 9 \times 10^{-6}$ $M_\odot$ (or $\sim 4.3\%$ of the overall disk and nova ejecta, up

[3]A value of 0.71 $R_\odot$ (i.e., the outer radius of the disk) has been adopted for $r_{\rm mean}$. This choice clearly results in an overestimated value for the binding energy of the disk.

[4]Note, however, that the disk does not get fully disrupted. In fact, only in Model 6 the disk gets fully disrupted and is swept up by the ejecta.

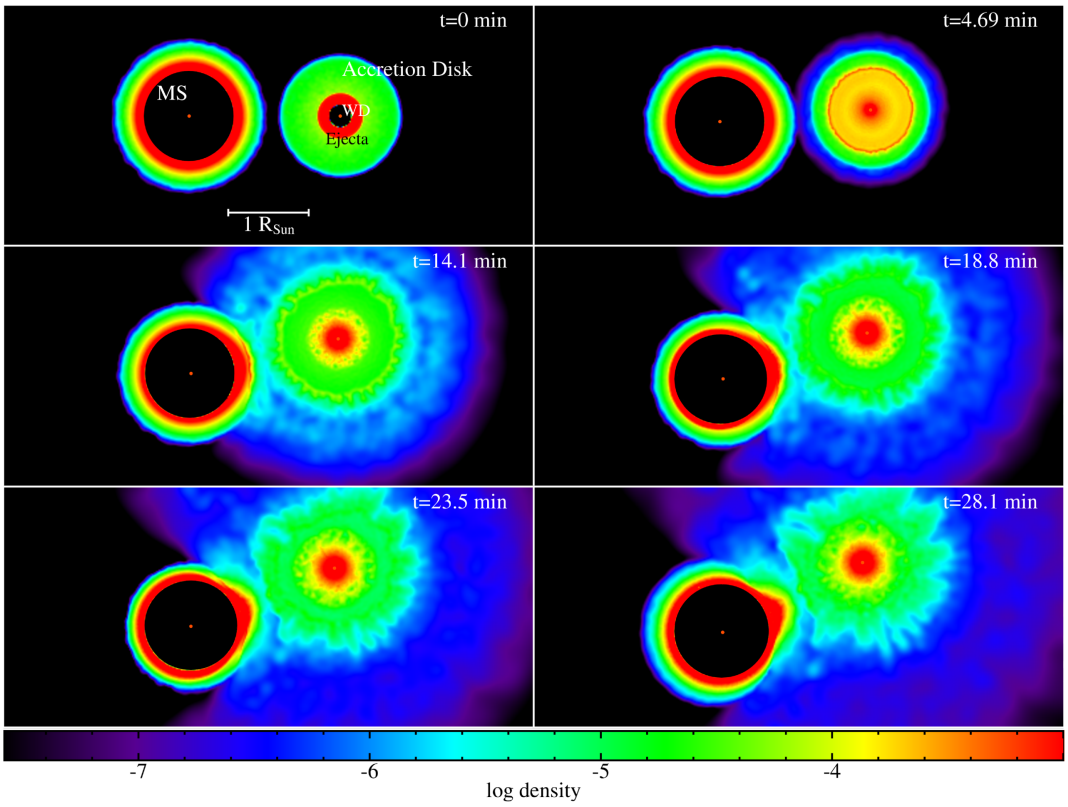

Figure 5.3: Cross-sectional slice in the binary orbital plane (XY) showing the density (in g/cm^3) of Model 1 at various stages of the interaction between the nova ejecta and the mass-accretion disk, subsequently followed by a collision with the main sequence, secondary star. A movie showing the full evolution of this model is available at `http://www.fen.upc.edu/users/jjose/Downloads.html`. Snapshots and movie were generated by means of the visualization software SPLASH (Price 2007).

to 28 minutes from the beginning of the simulation), representing a source of contamination of the outer layers of the secondary star. It is also worth noting that about $\sim 6.6 \times 10^{-9}$ $M_\odot$ are expelled from the main sequence star out of the binary system, while a tiny amount, $\sim 6 \times 10^{-10}$ $M_\odot$ of the same secondary star gets accreted by the white dwarf star.

Figure 5.4 shows the time evolution of the mass leaving the binary system in Model 1. The early and sharp increase in mass loss ($t \leq 3$ min) results from the interaction between the nova ejecta and the disk, when the latter receives the impact and gets mixed with the former. The longer-term evolution of the mass loss reveals that little is expelled from the outer layers of the subgiant companion as a result of the impact with the nova ejecta. The small decline observed in M_{esc} is due to particles that marginally achieved escape velocity at some stage, and were later decelerated by interactions with the material orbiting the binary system.

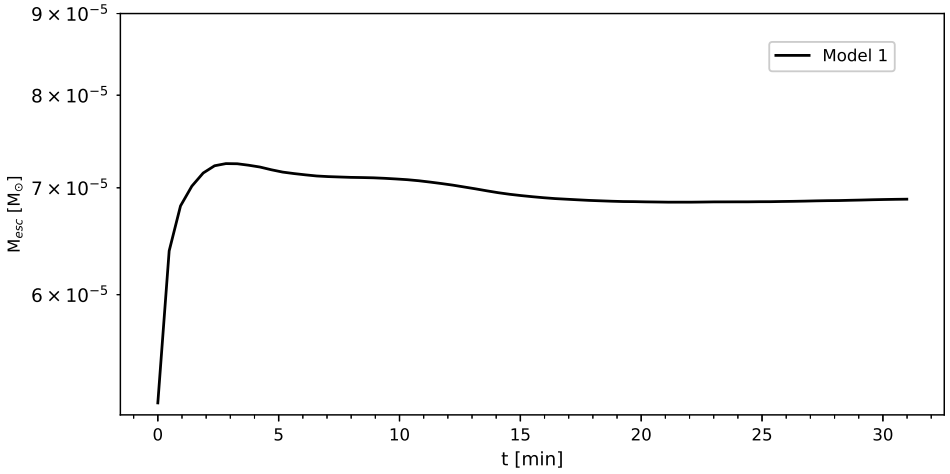

Figure 5.4: Time evolution of the mass leaving the binary system in Model 1.

5.2.2 Effect of the white dwarf mass

The fiducial model (hereafter, Model 1) discussed in the previous subsection relies on a 0.6 $M_\odot$ white dwarf that hosts a nova outburst. To analyze the effect of the white dwarf mass on the long-term evolution of a cataclysmic binary system, we have computed Model 4 (see Figure 5.5), which is identical to Model 1, except by the presence of a more massive, 1.25 $M_\odot$ white dwarf. The stronger gravitational pull exerted by a more massive white dwarf translates into a larger amount of ejecta that remains bound to the white dwarf (2.03×10^{-4} $M_\odot$ for Model 4 and 1.38×10^{-4} $M_\odot$ for Model 1, representing 97.1% and 65.9% of the overall disk and ejecta, respectively), reducing in turn both the mass that escapes the binary system as well as the mass that reaches and remains bound to the main sequence companion. Hence, while $\Delta M_{esc} = 6.22 \times 10^{-5}$ $M_\odot$ and $\Delta M_{MS} = 8.99 \times 10^{-6}$ $M_\odot$ were found in Model 1, $\Delta M_{esc} = 5.99 \times 10^{-6}$ $M_\odot$ and $\Delta M_{MS} = 2 \times 10^{-9}$ $M_\odot$ were obtained when a more massive white dwarf is adopted (Model 4). These values represent 29.8% and 4.3% of the disk and ejecta for Model 1, while merely 2.87% and 0.001% for Model 4. Finally, it is also worth noting the reduced amount of mass from the secondary star that gets lost from the binary system ($\Delta M_{MS} = 2 \times 10^{-10}$ $M_\odot$ in Model 4 vs. $\Delta M_{MS} = 6.6 \times 10^{-9}$ $M_\odot$ in Model 1). The interaction with the main sequence companion in Model 4 (see lower panels of Figure 5.5) resumes the mass transfer to the primary.

5.2.3 Effect of the orbital period

Cataclysmic variable systems leading to classical nova outbursts are characterized by orbital periods between 1.4 and 16 hr (Diaz & Bruch 1997), with a large fraction in the 2.8-4.1 hr range (Warner 2002). To analyze the effect of the orbital period on the long-term evolution of these systems, we have computed Model 5, characterized by an orbital period of 12.76 hr, twice the value adopted for Model 1 (6.38 hr). This implies a wider orbit, according to Kepler's third law. While this have a negligible effect on the amount of nova ejecta that

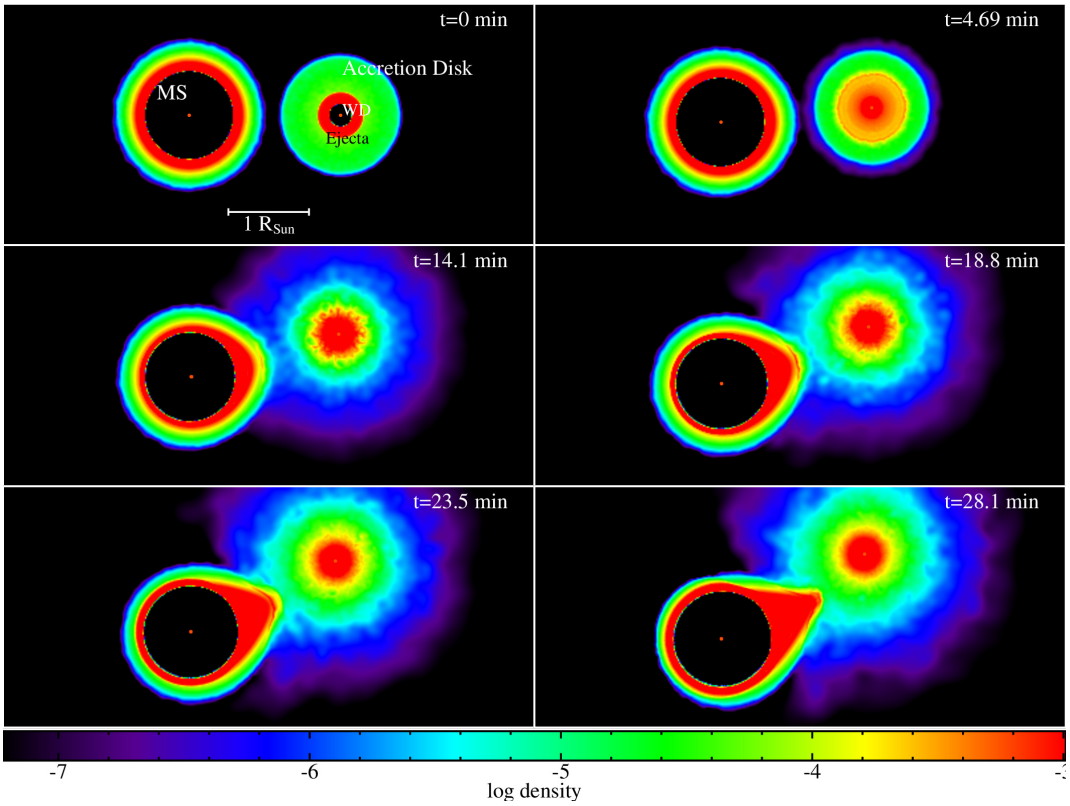

Figure 5.5: Cross-sectional slice in the binary orbital plane (XY) showing the density (in g/cm^3) of Model 4 at various stages of the interaction between the nova ejecta and the mass-accretion disk, subsequently followed by a collision with the main sequence, secondary star. A movie showing the full evolution of this model is available at `http://www.fen.upc.edu/users/jjose/Downloads.html`. Snapshots and movie were generated by means of the visualization software SPLASH (Price 2007).

remains bound to the white dwarf (1.32×10^{-4} M$_\odot$ for Model 5 and 1.38×10^{-4} M$_\odot$ for Model 1, representing 63.1% and 65.9% of the overall disk and ejecta, respectively), there is a strong effect on both the mass that escapes the binary system as well as on the mass that reaches and remains bound to the main sequence companion. Hence, while $\Delta M_{esc} = 6.22 \times 10^{-5}$ M$_\odot$ and $\Delta M_{MS} = 8.99 \times 10^{-6}$ M$_\odot$ were found in Model 1, $\Delta M_{esc} = 7.71 \times 10^{-5}$ M$_\odot$ and $\Delta M_{MS} \sim 0$ were obtained for Model 5. These values, which represent 29.8% and 4.3% of the disk and ejecta for Model 1, and 36.9% and 0% for Model 5, can be understood on the basis of the wider orbit that characterizes Model 5: this reduces the effective gravitational pull exerted by the secondary star on the ejecta+disk plasma, which increases the fraction that leaves the binary system. With regard to the mass of the secondary star that got lost from the binary system, which reached $\Delta M_{MS} = 6.6 \times 10^{-9}$ M$_\odot$ in Model 1, the reduced interaction with the main sequence companion reported in Model 5 translates into a fully negligible amount ($\Delta M_{MS} \sim 0$).

5.2.4 Effect of the mass of the accretion disk

As discussed in previous chapters, the mass of the accretion disk that orbits the white dwarf star is a poorly constrained quantity. Its effect on the long-term evolution of an interacting stellar binary system has already been analyzed in this Thesis, in the framework of two different scenarios: in Chapter 3, several disks, with masses ranging between 2×10^{-5} $M_\odot$ and 9×10^{-5} $M_\odot$, were considered to evaluate the likelihood of survival in the impact with a more massive ejecta, $M_{\rm ej} = 2 \times 10^{-5}$ $M_\odot$; In Chapter 4, the disks adopted, with masses ranging between 10^{-6} $M_\odot$ and 4.4×10^{-6} $M_\odot$, were comparable to the mass of the ejecta[5], $M_{\rm ej} = 2.1 \times 10^{-6}$ $M_\odot$. In this Chapter, we wanted to test the sensitivity of `GADGET-2` to small differences in the mass of the disk, in a collision dominated by a massive ejecta. To this end, the long-term evolution of the system has been analyzed by a thorough comparison between Models 1 and 3, for which two different values of the mass of the disk, $M_{\rm disk}$, that just differ by a factor of 2, were adopted (2×10^{-6} $M_\odot$ and 10^{-6} $M_\odot$, respectively). Both disks were eventually hit by a fraction (about 14%) of a more massive ejecta, $M_{\rm ej} = 2 \times 10^{-4}$ $M_\odot$. While the analyses of the systems described in Chapters 3 and 4 were swamped by the different outcome, with a mixture of models in which the disk survived the hit and others in which the disk was fully disrupted by the nova blast, here we will compare two models that experienced the same fate: disk disruption. As expected, differences between Models 1 and 3 are really small, of the order of 1% variation in the fractions of masses bound to the secondary star or leaving the binary system, over the total ejecta plus disk masses (see Table 5.2), which proves the robustness of the conclusions reached in previous chapters with regard to the effect of the mass of the disk.

5.2.5 Effect of the geometry of the accretion disk: flared vs. V-shaped disks

The effect of the geometry of the disk was previously analyzed in Chapter 4, in the context of the recurrent nova U Sco. That system is characterized by a much wider orbit ($P_{\rm orb} \sim 30$ hr) than the cataclysmic systems considered in this Chapter. Moreover, in the simulations already reported (see Models A-H and F-G, in Chapter 4), disk and ejecta had very similar masses, while most of the models discussed in this Chapter are clearly dominated by a more massive ejecta. All in all, it is worth reanalyzing the effect of the geometry of the accretion disk in these conditions. To this end, we will compare the properties of two models (Models 1 and 2), that just differ in the geometry adopted for the disk: a V-shaped disk in Model 1 and a flared disk in Model 2. The more extended disk of the V-shaped configuration favors a larger fraction of the disk plus ejecta to bounce back, remaining gravitationally bound to the white dwarf star: indeed, while 9.98×10^{-5} $M_\odot$, representing 47.79% of the disk plus ejecta, is obtained in the flared-disk Model 2, 1.38×10^{-4} $M_\odot$, representing 65.9% of the disk plus ejecta, is obtained in Model 1, characterized by a V-shaped disk. In turn, the shape of the disk, through the different effective cross-section of interaction with the ejecta, dramatically affects the amount of matter that leaves the binary system: while 9.99×10^{-5} $M_\odot$, representing 47.85% of the disk plus ejecta, is obtained in the flared-disk Model 2, a smaller 6.22×10^{-5} $M_\odot$, representing only 29.8% of the disk plus ejecta, is obtained in Model 1. Another striking difference with respect to the models presented in Chapter 4 involves the interaction with the secondary: while only a handful of particles from the disk

[5]Note, however, that the collision in all models involves only a fraction of the ejecta (typically, 10%-20%).

plus ejecta reach the subgiant secondary in the simulations reported for U Sco, here the number of particles that reach and hit the main sequence secondary is noticeable: all in all, 8.99×10^{-6} $M_\odot$, representing 4.30% of the disk plus ejecta, reach the secondary in the flared-disk Model 2, almost identical to the 9.11×10^{-6} $M_\odot$, representing 4.36% of the disk plus ejecta, obtained in Model 1, suggesting that the shape of the disk does not play a crucial role in the contamination of the secondary. This explains in turn the similar values obtained in the amounts of mass of the secondary star that get lost from the binary system ($\Delta M_{MS} = 7.2 \times 10^{-9}$ $M_\odot$ in Model 2 vs. $\Delta M_{MS} = 6.6 \times 10^{-9}$ $M_\odot$ in Model 1).

5.2.6 Combined effect of the mass and velocity of the ejecta

Finally, we wanted to address the combined effect of the mass and velocity of the ejecta through the analysis of two models: Model 4, for which 2.1×10^{-4} $M_\odot$ of ejecta, with a maximum velocity of 1200 km s^{-1}, had been considered; and Model 6, characterized by a less massive ejecta, 2.1×10^{-5} $M_\odot$, but with a higher maximum velocity of 4800 km s^{-1}. It is important to highlight that both ejecta, despite their differences, are characterized by a similar kinetic energy (just 1.6 times higher in Model 6). To understand the different outcome obtained from both models[6], however, it is important to realize that while Model 4 is fully dominated by the mass of the ejecta (the value adopted corresponds to 100 times the mass of the disk), differences are smaller in Model 6, with a disk that contains only 10% of the mass of the ejecta. Assuming that about 10% of the mass of the ejecta is effectively involved in the collision with the disk, we expect about 2.2×10^{-5} $M_\odot$ of disk plus ejecta in the collision resulting in Model 4, while only 4×10^{-6} $M_\odot$ in Model 6. Bearing in mind that the kinetic energy of the material that collides with the disk is similar in both models (less than a factor of 2 difference), we conclude that the collision with the disk in Model 4 involves more mass while similar kinetic energy is being deposited by the incoming ejecta, or in other words: a collision with less energy per unit mass. Therefore, we can anticipate a larger fraction of material to remain bound to the white dwarf and an overall reduction in the amount of mass leaving the system in Model 4, compared to Model 6. Indeed, this is what the results of the simulations, summarized in Table 5.2, show: while $\Delta M_{\rm WD} = 2.03 \times 10^{-4}$ $M_\odot$ and $\Delta M_{\rm lost} = 5.99 \times 10^{-6}$ $M_\odot$ have been obtained in Model 4, representing 97.1% and 2.9% of the overall disk and ejecta, respectively, $\Delta M_{\rm WD} = 1.02 \times 10^{-6}$ $M_\odot$ and $\Delta M_{\rm lost} = 2.17 \times 10^{-5}$ $M_\odot$ have been obtained in Model 6, which correspond to 4.5% and 95.4% of the disk plus ejecta, respectively. In both cases, the amount of disk plus ejecta that finally hits the secondary star is very small (10 times larger in Model 6, as expected from the much lower percentage that remains bound to the white dwarf), as negligible as the number of particles from the secondary that leave the binary system after interacting with the incoming flow (about a 100 times larger in Model 6, also as expected).

5.3 Conclusions

We have extended the analysis of the different parameters of a cataclysmic stellar binary system (i.e., mass, velocity and density of the ejecta, mass and geometry (shape) of the accretion disk), presented in previous chapters, to additional parameters, such as the orbital period or the white dwarf mass, in a series of 3D SPH simulations of the interaction between

[6] Both models yield to the total disruption of the accretion disk, however.

the nova ejecta, the accretion disk and the secondary star. The fiducial model adopted in this chapter consists of a 0.6 $M_{\odot}$ white dwarf (treated as a point-like mass) and a 0.66 $M_{\odot}$ main sequence secondary (built in spherical symmetry and hydrostatic equilibrium conditions, assuming a polytropic equation of state with $\gamma = 5/3$). A V- shaped accretion disk of 2×10^{-6} $M_{\odot}$ has been placed in Keplerian rotation, orbiting around the point-like white dwarf. The white dwarf star and the main sequence companion are assumed to orbit around the center-of-mass of the binary system with an orbital period of $P_{\rm orb} = 6.38$ hr. The simulation follows the long-term evolution of the system after 2.1×10^{-4} $M_{\odot}$ of nuclear-processed ejecta from a nova outburst have been expelled by the white dwarf, with a maximum velocity of 1200 km s^{-1}. Five additional models have been computed for slightly different conditions, all of them resulting in the disruption of the accretion disk. The six models considered have been evolved in a co-rotating reference frame, and accordingly, include non-inertial forces (i.e., centrifugal and Coriolis forces). The main conclusions reached in this chapter can be summarized as follows:

- The presence of a more massive white dwarf (e.g., Model 4) translates into larger amounts of ejecta that remain bound to the white dwarf, reducing in turn both the mass that leaves the binary system as well as the mass that reaches and remains bound to the main sequence companion. In turn, it also reduces the amount of mass from the secondary star that gets lost from the system.

- The adoption of a larger orbital period (or of a wider binary system; e.g., Model 5), while having a negligible effect on the amount of disk plus ejecta that remains bound to the white dwarf, has a strong impact on both the mass that leaves the binary system and on the mass that reaches and remains bound to the main sequence companion. The wider orbit reduces the effective gravitational pull exerted by the secondary star on the ejecta plus disk plasma, which increases the fraction of mass that leaves the binary system. The reduced interaction with the main sequence companion translates also into a reduction of the overall mass of the secondary star that leaves the binary system (negligible, in Model 5).

- The robustness of the results obtained (and the conclusions reached) in previous chapters with regard to the effect of the mass of the disk has been validated by a study aimed at testing the sensitivity of the `GADGET-2` code to small differences in the mass of the disk, in collisions dominated by a massive nova ejecta (e.g., Models 1 and 3).

- The effect of the geometry of the disk (i.e., V-shaped vs. Flared disks) has been reanalyzed in the context of closer binary systems characterized by massive ejecta (i.e., Models 1 and 2). The more extended configuration of the V-shaped disk favors a larger fraction of the disk plus ejecta to bounce back, remaining gravitationally bound to the white dwarf star. This dramatically affects the amount of matter that leaves the binary system, significantly reduced in the model evolved with a V-shaped disk. However, the shape of the disk does not seem to play a key role in the degree of contamination of the secondary star by the disk plus ejecta plasma.

- The combined effect of the mass and velocity of the ejecta has been analyzed by means of two models with different masses and velocities but similar kinetic energy of the ejecta (i.e., Models 4 and 6). A collision with a more massive ejecta but equal kinetic energy implies smaller energy per unit mass, which results in a larger amount of

material remaining bound to the white dwarf and an overall reduction in the amount of mass leaving the system.

Chapter 6

Conclusions and Future work

6.1 Conclusions

In this Thesis, a suite of three-dimensional, SPH (Smoothed Particle Hydrodynamics) simulations of the interaction between the nova ejecta, the accretion disk, and the stellar companion were performed by making use of `GADGET-2` (Springel *et al.* 2001; Springel & Hernquist 2002; Springel 2005, see also Section 2.2). The goal was to test the influence of the different parameters (i.e., mass and velocity of the ejecta, mass and geometry of the accretion disk, mass of the white dwarf (WD), orbital period...) on the dynamical (and chemical) properties of different classical and recurrent nova systems.

Shortly after the outer layers of the white dwarf envelope expand and achieve escape velocity, the ejecta hits the disk. Though the characteristics of the disk are poorly constrained quantities, some observations seem to indicate its presence much sooner than expected (Leibowitz *et al.* 1992; Retter *et al.* 1997, 1998; Skillman *et al.* 1997; Hernanz & Sala 2002; Schaefer 2011, see, e.g.,). In this Thesis, we have investigated this interaction and the conditions that lead to the disruption of the disk. We found that in some models, the disk gets fully disrupted and swept up, while in others the disk survives or gets only partially disrupted, depending on the M_{ejecta}/M_{disk} ratio. As expected, massive disks tend to survive the impact of the ejecta. However, the velocity (kinetic energy) of the ejecta plays an important role in this regard: the large kinetic energy and momentum carried by high-velocity ejecta lead, in some cases, to disk disruption even for systems characterized by relatively low M_{ejecta}/M_{disk} ratio, favoring as well larger amounts of mass to be ejected from the binary system, and reducing in turn the mass that remains bound to the primary, white dwarf star. Clues on the expected outcome of the disk can be obtained from a rough comparison between the mean kinetic energy of the impinging ejecta and the binding energy of the disk, particularly when both estimates are significantly different.

To further understand the influence of the disk in the long-term evolution of these binary systems, we also considered different geometries (i.e., V-shaped and flared disk models). Our simulations indicate that extended V-shaped disks tend to force a larger fraction of the ejecta to slow down after the collision with respect to models with flared disks, thus increasing the amount of mass that remains gravitationally bound to the white dwarf after the impact. As the system evolves, part of the ejecta plus disk mixture is expelled out of the binary system, while some amount of this material ultimately impinges on the companion star. As

a result, it is expected that part of this plasma ends up mixing with the outermost layers of the secondary. To understand the implications of this contamination for the next nova cycle, we estimated the mean metallicity at the hemisphere of the secondary star hit by the ejecta. We found that for models with moderate ejecta velocities and masses, characteristic of classical nova systems, chemical pollution of the secondary may have an impact on the next nova cycle, once mass transfer from the secondary resumes; however, in models with extreme velocities and low mass ejecta, as in recurrent nova systems, contamination of the secondary is much more limited, as less particles stay bound to the companion star.

During the interaction between the disk plus ejecta and the secondary star, a small amount of material from the outer layers of the companion can effectively be expelled from the star and be eventually ejected from the binary system (up to $1.4\times\ 10^{-6} M_{\odot}$, for the classical nova models analyzed in this Thesis, and up to $8.3\ \times\ 10^{-8} M_{\odot}$, in the case of recurrent novae). It is also worth mentioning that both the mass and the geometry of the disk have an impact on the mass ejected from the system and on the amount that gets bound to the white dwarf. Increasing the mass of the disk or the cross-section between disk and ejecta (as in V-shaped disks), slows down a larger fraction of the nova ejecta, which in turn increases the mass that remains gravitationally bound to the white dwarf, while reducing the overall mass lost from the binary system. However, the shape of the disk does not seem to affect deeply the amount of material that hits the secondary star in classical nova systems (Chapter 5).

Finally, we have also analyzed the effect of the orbital period and the mass of the white dwarf. A larger orbital period (i.e., a wider binary system) leads to a more limited gravitational pull exerted by the secondary star on the ejecta plus disk, which results in a larger amount of mass ejected from the binary system, while reducing the overall mass that hits the secondary (as well as reducing the amount of material of the secondary that leaves the binary system). The presence of a more massive white dwarf increases the amount of ejecta plus disk material that remains bound to the white dwarf, reducing in turn both the mass that leaves the binary system and the mass that reaches and remains bound to the companion (which, in turn, reduces the amount of mass from the secondary star that gets lost from the system). It is also worth noting that the larger gravitational pull exerted by a more massive white dwarf forces also an acceleration in the mass transfer process from the secondary, which resumes at much earlier times when compared to models with less massive white dwarfs, as shown in our simulations.

6.2 Future work

The biggest limitation that we came across during this Thesis is related with the resolution of the disk and the ejecta, caused by adoption of the same mass for all SPH particles, to guarantee a good accuracy in the interpolated functions, in all simulations. In an attempt to minimize this limitation, we modeled only the outer layers of the companion star. However, this was not enough, given the high density contrasts between both the ejecta plus disk and the companion star. This limitation translates into a great deal of computational resources. A possible way to increase this resolution is to use a conical 3D computational domain, in which the point-like white dwarf is located at the vertex of the cone, so that only a fraction of the ejecta and disk, together with the full stellar secondary, are taken into account. The expected gain in resolution could reach a factor of ~ 2, having ~ 10 times more particles in the conical computational domain.

We would also be interested in the study of the evolution of the orbital period, in an attempt to shed light into whether the orbital period increases or decreases in cataclysmic and symbiotic binary systems. For instance, V1017 Sgr, a system that displayed a classical nova outburst in 1919 as well as several dwarf nova eruptions (1901, 1973, 1991), has been claimed to experience a decrease in orbital period (V. Salazar *et al.* 2017) that is at odds with some scenarios proposed for classical novae that suggest instead a period increase, such as the "hibernation" model (Shara *et al.* 1986). To that end, we plan to run an extensive set of 3D SPH simulations for an entire orbital period and covering the wide parameter space, to elucidate possible variations in the orbital period during the long-term evolution of these interacting systems.

The low densities that characterize the ejected plasma, together with the limited peak temperatures frequently reached in the collisions with the disk and secondary star reported in this Thesis, suggest that nuclear processing is not important. Nevertheless, we plan to incorporate a nuclear reaction network to validate such conclusions.

A detailed analysis of the contamination of the secondary star in the models reported in this Thesis requires the inclusion of additional (and relevant) physical processes, such as chemical diffusion and convection. This could be done by matching the structure of the secondary star, at the moment when it is hit by the fraction of ejecta plus disk, into a suitable grid, that could subsequently be implemented and followed by any of the available grid-based codes, such as `FLASH` (). In the very-long term, one may even think on performing a full series of nova outbursts, beginning with 1D simulations of the nova outbursts, assuming a given composition for the mass transferred from the companion star (`SHIVA`), continuing with 3D SPH simulations of the interaction between the ejecta, the accretion disk and the secondary star (`GADGET-2`), determining the level of contamination of the secondary (`FLASH`), and extending this to a series of explosions, as the composition of the mass transferred from the companion varies as a result of contamination. Moreover, collaborations with other teams (e.g., K. Lodders, WUST in St Louis, USA), could also help to clarify whether contamination of the secondary, after a series of bursts, helps in better matching the isotopic ratios measured in meteoritic presolar grains of a putative nova origin (see, e.g., Amari *et al.* 2001; Amari 2002), through models of condensation of the different ejecta.

Finally, it would be interesting to extend the simulations reported in this Thesis to the determination of observables (e.g., X-ray signatures of the interaction with the ejecta and the secondary star), that in turn, would expand the impact and interest of this work to other astrophysical areas (e.g., high-energy astrophysics).

Bibliography

Ackermann, M., Ajello, M., Albert, A., Baldini, L., Ballet, J., Barbiellini, G., Bastieri, D., Bellazzini, R., Bissaldi, E., Blandford, R. D., Bloom, E. D., Bottacini, E., Brandt, T. J., Bregeon, J., Bruel, P., Buehler, R., Buson, S., Caliandro, G. A., Cameron, R. A., Caragiulo, M., Caraveo, P. A., Cavazzuti, E., Charles, E., Chekhtman, A., Cheung, C. C., Chiang, J., Chiaro, G., Ciprini, S., Claus, R., Cohen- Tanugi, J., Conrad, J., Corbel, S., D'Ammando, F., de Angelis, A., den Hartog, P. R., de Palma, F., Dermer, C. D., Desiante, R., Digel, S. W., Di Venere, L., do Couto e Silva, E., Donato, D., Drell, P. S., Drlica-Wagner, A., Favuzzi, C., Ferrara, E. C., Focke, W. B., Franckowiak, A., Fuhrmann, L., Fukazawa, Y., Fusco, P., Gargano, F., Gasparrini, D., Germani, S., Giglietto, N., Giordano, F., Giroletti, M., Glanzman, T., Godfrey, G., Grenier, I. A., Grove, J. E., Guiriec, S., Hadasch, D., Harding, A. K., Hayashida, M., Hays, E., Hewitt, J. W., Hill, A. B., Hou, X., Jean, P., Jogler, T., Jóhannesson, G., Johnson, A. S., Johnson, W. N., Kerr, M., Knödlseder, J., Kuss, M., Larsson, S., Latronico, L., Lemoine-Goumard, M., Longo, F., Loparco, F., Lott, B., Lovellette, M. N., Lubrano, P., Manfreda, A., Martin, P., Massaro, F., Mayer, M., Mazziotta, M. N., McEnery, J. E., Michelson, P. F., Mitthumsiri, W., Mizuno, T., Monzani, M. E., Morselli, A., Moskalenko, I. V., Murgia, S., Nemmen, R., Nuss, E., Ohsugi, T., Omodei, N., Orienti, M., Orlando, E., Ormes, J. F., Paneque, D., Panetta, J. H., Perkins, J. S., Pesce-Rollins, M., Piron, F., Pivato, G., Porter, T. A., Rainò, S., Rando, R., Razzano, M., Razzaque, S., Reimer, A., Reimer, O., Reposeur, T., Saz Parkinson, P. M., Schaal, M., Schulz, A., Sgrò, C., Siskind, E. J., Spandre, G., Spinelli, P., Stawarz, Ł., Suson, D. J., Takahashi, H., Tanaka, T., Thayer, J. G., Thayer, J. B., Thompson, D. J., Tibaldo, L., Tinivella, M., Torres, D. F., Tosti, G., Troja, E., Uchiyama, Y., Vianello, G., Winer, B. L., Wolff, M. T., Wood, D. L., Wood, K. S., Wood, M., Charbonnel, S., Corbet, R. H. D., De Gennaro Aquino, I., Edlin, J. P., Mason, E., Schwarz, G. J., Shore, S. N., Starrfield, S., Teyssier, F., & Fermi-LAT Collaboration. 2014. Fermi establishes classical novae as a distinct class of gamma-ray sources. *Science*, **345**(Aug.), 554–558.

Alexakis, A., Calder, A. C., Heger, A., Brown, E. F., Dursi, L. J., Truran, J. W., Rosner, R., Lamb, D. Q., Timmes, F. X., Fryxell, B., Zingale, M., Ricker, P. M., & Olson, K. 2004. On Heavy Element Enrichment in Classical Novae. *The astrophysical journal*, **602**(2), 931–937.

Amari, S. 2002. Presolar grains from novae: their isotopic ratios and radioactivities. *New astronomy reviews*, **46**(July), 519–524.

Amari, S., Gao, X., Nittler, L. R., Zinner, E., José, J., Hernanz, M., & Lewis, R. S. 2001. Presolar Grains from Novae. *The astrophysical journal*, **551**(Apr.), 1065–1072.

Anupama, G. C. 2008 (Dec.). The Recurrent Nova Class of Objects. *Page 31 of:* Evans, A., Bode, M., O'Brien, T., & Darnley, M. (eds), *Rs ophiuchi (2006) and the recurrent nova phenomenon*. Astronomical Society of the Pacific Conference Series, vol. 401.

Anupama, G. C., & Dewangan, G. C. 2000. The 1999 outburst of the recurrent nova u scorpii. *The astronomical journal*, **119**(3), 1359–1364.

Baade, W. 1938. The Absolute Photographic Magnitude of Supernovae. *Astrophysical journal*, **88**(Oct.), 285.

Baade, W., & Zwicky, F. 1934. On Super-novae. *Proceedings of the national academy of sciences of the united states of america*, **20**(May), 254–259.

Balbus, S. A., & Hawley, J.F. 1991. A Powerful Local Shear Instability in Weakly Magnetized Disks. I. Linear Analysis. *The astrophysical journal*, **376**(July), 214.

Balsara, D. S. 1995. von Neumann stability analysis of smooth particle hydrodynamics–suggestions for optimal algorithms. *Journal of computational physics*, **121**, 357–372.

Barnes, J., & Hut, P. 1986. A hierarchical O(N log N) force-calculation algorithm. *Nature*, **324**(Dec.), 446–449.

Benz, W. 1990. *Smooth Particle Hydrodynamics - a Review*. Vol. 302.

Bode, J., & Evans, A. 1989. *Classical novae*. Wiley, Chichester.

Cabezón, R. M., García-Senz, D., & Relaño, A. 2008. A one-parameter family of interpolating kernels for Smoothed Particle Hydrodynamics studies. *Journal of computational physics*, **227**(Oct.), 8523–8540.

Casanova, J., José, J., García-Berro, E., Shore, S. N., & Calder, A. C. 2011. Kelvin-Helmholtz instabilities as the source of inhomogeneous mixing in nova explosions. *Nature*, **478**(Oct.), 490–492.

Catalán, S., Isern, J., García-Berro, E., & Ribas, I. 2008. The initial-final mass relationship of white dwarfs revisited: effect on the luminosity function and mass distribution. *Monthly notices of the royal astronomical society*, **387**(4), 1693–1706.

Chomiuk, L., Nelson, T., Mukai, K., Sokoloski, J. L., Rupen, M. P., Page, K. L., Osborne, J. P., Kuulkers, E., Mioduszewski, A. J., Roy, N., Weston, J., & Krauss, M. I. 2014. The 2011 Outburst of Recurrent Nova T Pyx: X-ray Observations Expose the White Dwarf Mass and Ejection Dynamics. *The astrophysical journal*, **788**(June), 130.

Corradi, R. L. M., Mikolajewska, R., & Mahoney, T. J. (eds). 2003. *The Transition Phase in Classical Novae*. Astronomical Society of the Pacific Conference Series, vol. 303.

Darnley, M., Williams, S., Bode, M., Shafter, A., Henze, M., Ness, J., & Hounsell, R. 2014. Recurrent Nova M31N 2008-12a: Liverpool Telescope discovery of 6th eruption in 7 years. *The astronomer's telegram*, **6527**(Oct.), 1.

Darnley, M. J. 2021 (Feb.). Accrete, Accrete, Accrete... Bang! (and repeat): The remarkable Recurrent Novae. *Page 44 of: The golden age of cataclysmic variables and related objects v*, vol. 2-7.

Darnley, M. J., Bode, M. F., Kerins, E., Newsam, A. M., An, J., Baillon, P., Belokurov, V., Calchi Novati, S., Carr, B. J., Crézé, M., Evans, N. W., Giraud-Héraud, Y., Gould, A., Hewett, P., Jetzer, Ph.; Kaplan, J., Paulin-Henriksson, S., Smartt, S. J., Tsapras, Y., & Weston, M. 2006. Classical novae from the POINT-AGAPE microlensing survey of M31 - II. Rate and statistical characteristics of the nova population . *Monthly notices of the royal astronomical society*, **369**(June), 257–271.

Diaz, M. P., & Bruch, A. 1997. The orbital period distribution of novae. *Astronomy and astrophysics*, **322**(June), 807–816.

Drake, J. J., & Orlando, S. 2010. The early blast wave of the 2010 explosion of u scorpii. *The astrophysical journal*, **720**(2), L195–L200.

Duerbeck, H. W. 2008. *Novae: an historical perspective*. 2 edn. Cambridge Astrophysics. Cambridge University Press. Page 1â15.

Dürbeck, H. W., Dümmler, R., Seitter, W. C., Leibowitz, E. M., & Shara, M. M. 1993. The recurrent nova U Sco - a touchstone of nova theories. *The messenger*, **71**(Mar.), 19–21.

Eckart, C. 1960. Variation Principles of Hydrodynamics. *Physics of fluids*, **3**(May), 421–427.

Eggleton, P. 2006. *Evolutionary Processes in Binary and Multiple Stars*.

Eggleton, P. P. 1983. Approximations to the radii of Roche lobes. *The astrophysical journal*, **268**(May), 368.

Evans, A., & Rawlings, J. M. C. 2008. *Dust and molecules in nova environments*. 2 edn. Cambridge Astrophysics. Cambridge University Press. Page 308â334.

Fourtakas, G., K., Stansby P., D., Rogers B., & J., Lind S. 2018. An eulerian-lagrangian incompressible sph formulation (eli-sph) connected with a sharp interface. *Computer methods in applied mechanics and engineering*, **329**, 532–552.

Frank, J., King, A., & Raine, D. J. 2002. *Accretion Power in Astrophysics: Third Edition*.

Fujimoto, M. Y. 1982. A theory of hydrogen shell flashes on accreting white dwarfs. I - Their progress and the expansion of the envelope. II - The stable shell burning and the recurrence period of shell flashes. *The astrophysical journal*, **257**(June), 752–779.

García-Berro, E., Ritossa, C., & Iben, I. Jr. 1997. On the Evolution of Stars that Form Electron-Degenerate Cores Processed by Carbon Burning. III. The Inward Propagation of a Carbon-Burning Flame and Other Properties of a 9 $M_{\odot}$ Model Star. *The astrophysical journal*, **485**(Aug.), 765–784.

García-Senz, D., Badenes, C., & Serichol, N. 2012. Is There a Hidden Hole in Type Ia Supernova Remnants? *The astrophysical journal*, **745**(Jan.), 75.

Gehrz, R. 2008. Infrared studies of classical novae. *Chap. 6, pages 167–191 of:* Bode, M. F., & Evans, A. E. (eds), *Classical novae, 2nd edition.* Cambridge: Cambridge University Press.

Gehrz, R. D. 1988. The infrared temporal development of classical novae. *Annual review of astronomy and astrophysics*, **26**(Jan.), 377–412.

Gehrz, R. D., Truran, J. W., Williams, R. E., & Starrfield, S. 1998. Nucleosynthesis in Classical Novae and Its Contribution to the Interstellar Medium. *Publications of the astronomical society of the pacific*, **110**(Jan.), 3–26.

Gingold, R. A., & Monaghan, J. J. 1977. Smoothed particle hydrodynamics - Theory and application to non-spherical stars. *Monthly notices of the royal astronomical society*, **181**(Nov.), 375–389.

Glasner, S. A., Livne, E., & Truran, J. W. 2007. Novae: The evolution from onset of convection to the runaway. *The astrophysical journal*, **665**(2), 1321–1333.

Goldman, I., & Wandel, A. 1995. Turbulent convection in thin accretion disks. *The astrophysical journal*, **443**(01).

Hachisu, I., & Kato, M. 2000. A theoretical light-curve model for the 1985 outburst of RS ophiuchi. *The astrophysical journal*, **536**(2), L93–L96.

Hachisu, I., & Kato, M. 2001. Recurrent novae as a progenitor system of type ia supernovae. i. RS ophiuchi subclass: Systems with a red giant companion. *The astrophysical journal*, **558**(1), 323–350.

Hachisu, I., Kato, M., T, Kato., Matsumoto, K., & Nomoto, K. 2000. A model for the quiescent phase of the recurrent nova u scorpii. *The astrophysical journal*, **534**(2), L189–L192.

Hachisu, I., Saio, H., & Kato, M. 2016. Shortest Recurrence Periods of Forced Novae. *The astrophysical journal*, **824**(June), 22.

Haenecour, P., Howe, J.Y., Zega, T.J., Amari, S., Lodders, K., José, J., Kaji, K., Sunaoshi, T., & Atsushi, M. 2019. Laboratory evidence for co-condensed oxygen- and carbon-rich meteoritic stardust from nova outbursts. *Nature astronomy*, 04, 626–630.

Hanes, D. A. 1985. The recurrent nova U Scorpii in post-outburst quiescence. *MNRAS*, **213**(Mar.), 443–449.

Hernanz, M., & José, J. 2008. The recurrent nova rs oph: A possible scenario for type ia supernovae. *New astronomy reviews*, **52**(7), 386–389. Astronomy with Radioactivities. VI.

Hernanz, M., & Sala, G. 2002. A Classical Nova, V2487 Oph 1998, Seen in X-rays Before and After Its Explosion. *Science*, **298**(5592), 393–395.

Hernquist, L., & Katz, N. 1989. TREESPH - A unification of SPH with the hierarchical tree method. *Astrophysical journal supplement series*, **70**(June), 419–446.

Hillman, Y., Prialnik, D., Kovetz, A., & Shara, M. 2015. Observational signatures of SNIa progenitors, as predicted by models. *MNRAS*, **446**(Jan.), 1924–1930.

Hurley, J. R., Pols, O. R., & Tout, C. A. 2000. Comprehensive analytic formulae for stellar evolution as a function of mass and metallicity. *MNRAS*, **315**(3), 543–569.

Iliadis, C., Downen, L., José, J., Nittler, L. R., & Starrfield, S. 2018. On presolar stardust grains from CO classical novae. *The astrophysical journal*, **855**(2), 76.

Johnston, H. M., & Kulkarni, S. R. 1992. Spectroscopy of the Recurrent Nova U Scorpii. *The astrophysical journal*, **396**(Sept.), 267.

José, J. 2016. *Stellar explosions: hydrodynamics and nucleosynthesis*. CRC/Taylor and Francis: Boca Raton, FL.

José, J., & Hernanz, M. 1998. Nucleosynthesis in Classical Novae: CO versus ONe White Dwarfs. *The astrophysical journal*, **494**(Feb.), 680–690.

José, J., & Shore, S. N. 2008. Observational mysteries and theoretical challenges for abundance studies. *Chap. 6, pages 121–138 of:* Bode, M. F., & Evans, A. E. (eds), *Classical novae, 2nd edition*. Cambridge: Cambridge University Press.

José, J., Hernanz, M., García-Berro, E., & Gil-Pons, P. 2003. The Impact of the Chemical Stratification of White Dwarfs on the Classification of Classical Novae. *The astrophysical journal*, **597**(1), L41–L44.

Justham, S., & Podsiadlowski, P. 2008 (Dec.). RS Ophiuchi-like Systems as SN Ia Progenitors: Direct Evidence and Potential Remnants. *Page 161 of:* Evans, A., Bode, M. F., O'Brien, T. J., & Darnley, M. J. (eds), *Rs ophiuchi (2006) and the recurrent nova phenomenon*. Astronomical Society of the Pacific Conference Series, vol. 401.

Kahabka, P., Hartmann, H. W., Parmar, A. N., & Negueruela, I. 1999. Luminous supersoft X-ray emission from the recurrent nova U Scorpii. *A&A*, **347**(July), L43–L46.

King, A. R., Pringle, J. E., & Livio, M. 2007. Accretion disc viscosity: how big is alpha? *MNRAS*, **376**(Apr.), 1740–1746.

Knigge, C., Long, K. S., Hoard, D. W., Szkody, P., & Dhillon, V. S. 2000. A Self-occulting Accretion Disk in the SW Sextantis Star DW Ursae Majoris. *The astrophysical journal*, **539**(1), L49–L53.

König, O., Wilms, J., Arcodia, R., Dauser, T., Dennerl, K., Doroshenko, V., Haberl, F., Hämmerich, S., Kirsch, C., Kreykenbohm, I., Lorenz, M., Malyali, A., Merloni, A., Rau, A., Rauch, T., Sala, G., Schwope, A., Suleimanov, V., Weber, P., & Werner, K. 2022. X-ray detection of a nova in the fireball phase. *Nature*, **605**(05), 248–250.

Kraft, R. P. 1964. Binary Stars among Cataclysmic Variables. III. Ten Old Novae. *The astrophysical journal*, **139**, 457.

Lajoie, C., & Sills, A. 2010. Mass transfer in binary stars using smoothed particle hydrodynamics. I. Numerical Method. *The astrophysical journal*, **726**(2), 66.

Leibowitz, E. M., Mendelson, H., Mashal, E., Prialnik, D., & Seitter, W. C. 1992. The Presence of an Accretion Disk in the Eclipsing Binary System Nova Herculis 1991 Three Weeks after Outburst. *The astrophysical journal*, **385**(Feb.), L49.

Lind, S. J., & Stansby, P. K. 2016. High-order Eulerian incompressible smoothed particle hydrodynamics with transition to Lagrangian free-surface motion. *Journal of computational physics*, **326**, 290–311.

Livio, M. 2000. The progenitors of type ia supernovae. *Type ia supernovae, theory and cosmology*, **33**.

Lombardi, J. C., Jr., Proulx, Z. F., Dooley, K. L., Theriault, E. M., Ivanova, N., & Rasio, F. A. 2006. Stellar Collisions and Ultracompact X-Ray Binary Formation. *The astrophysical journal*, **640**(1), 441–458.

Lucy, L. B. 1977. Numerical approach to the testing of the fission hypothesis. *Astronomical journal*, **82**(Dec.), 1013–1024.

Lundmark, K. 1925. The Motions and the Distances of Spiral Nebulæ. *MNRAS*, **85**(June), 865.

Maccarone, T. J. 2014. Observational Tests of the Picture of Disk Accretion. *Space Sci. Rev.*, **183**(1-4), 101–120.

MacDonald, J. 1983. CNO abundances and the strengths of nova outbursts and hydrogen flashes on accreting white dwarfs. *The astrophysical journal*, **267**(Apr.), 732–746.

Marietta, E., Burrows, A., & Fryxell, B. 2000. Type IA Supernova Explosions in Binary Systems: The Impact on the Secondary Star and Its Consequences. *The astrophysical journal supplement series*, **128**(June), 615–650.

Marks, P. B., & Sarna, M. J. 1998. The chemical evolution of the secondary stars in close binaries, arising from common-envelope evolution and nova outbursts. *MNRAS*, **301**(3), 699–720.

Marks, P. B., Sarna, M. J., & Prialnik, D. 1997. The chemical evolution of the secondary stars in close binary systems during nova outbursts. *MNRAS*, **290**(2), 283–291.

Mason, E. 2013 (Aug.). *U Scorpii 2010 outburst: observational evidence of an underlying ONeMg white dwarf (Corrigendum).* Astronomy & Astrophysics, Volume 556, id.C2, 1 pp.

Mason, E., Ederoclite, A., Williams, R. E., Della Valle, M., & Setiawan, J. 2012. U scorpii 2010 outburst: a new understanding of the binary accretion disk and the secondary star. *Astronomy and astrophysics*, **544**, A149.

Maxwell, M. P., Rushton, M. T., Darnley, M. J., Worters, H. L., Bode, M. F., Eyres, S. P. S., Kouwenhoven, M. B. N., Walter, F. M., Hassall, B. J. M., & Evans, A. 2012. The helium abundance in the ejecta of u scorpii. *Monthly notices of the royal astronomical society*, **419**(2), 1465–1471.

McLaughlin, D. B. 1944. The spectral changes of a typical nova. *Popular astronomy*, **52**(Jan.), 109.

Monaghan, J. J. 1992. Smoothed particle hydrodynamics. *ARA&A*, **30**, 543–574.

Monaghan, J. J. 1997. SPH and Riemann Solvers. *Journal of computational physics*, **136**(Sept.), 298–307.

Nelemans, G., Siess, L., Repetto, S., Toonen, S., & Phinney, E. S. 2016. The formation of cataclysmic variables: The influence of nova eruptions. *The astrophysical journal*, **817**(1), 69.

Nishiyama, K., & Kabashima, F. 2008. *http://www.cbat.eps.harvard.edu/iau/cbat*$_m$31.*html*2008−12*a*.

O'Brien, T., & Bode, M. 2008. Resolved nebular remnants. *Chap. 6, pages 285–306 of:* Bode, M. F., & Evans, A. E. (eds), *Classical novae, 2nd edition*. Cambridge: Cambridge University Press.

Paczynski, B. 1976 (Jan.). Common Envelope Binaries. *Page 75 of:* Eggleton, Peter, Mitton, Simon, & Whelan, John (eds), *Structure and evolution of close binary systems*, vol. 73.

Pagnotta, A., & Schaefer, B. E. 2014. Identifying and Quantifying Recurrent Novae Masquerading as Classical Novae. *The astrophysical journal*, **788**(2).

Pagnotta, A., Schaefer, B. E., Clem, J. L., Landolt, A. U., Handler, G., Page, K. L., Osborne, J. P., Schlegel, E. M., Hoffman, D. I., Kiyota, S., & Maehara, H. 2015. The 2010 Eruption of the Recurrent Nova U Scorpii: The Multi-wavelength Light Curve. *The astrophysical journal*, **811**(1), 32.

Pakmor, R., Edelmann, P., Röpke, F. K., & Hillebrandt, W. 2012. Stellar gadget: a smoothed particle hydrodynamics code for stellar astrophysics and its application to Type Ia supernovae from white dwarf mergers. *Monthly notices of the royal astronomical society*, **424**, 2222–2231.

Payne-Gaposchkin, C. 1957. *The galactic novae*.

Pietsch, W. 2010. X-ray emission from optical novae in M 31. *Astronomische nachrichten*, **331**(Feb.), 187.

Prialnik, D. 1986. The evolution of a classical nova model through a complete cycle. *The astrophysical journal*, **310**(Nov.), 222–237.

Prialnik, D., & Kovetz, A. 1984. The effect of diffusion on prenova evolution - CNO-enriched envelopes. *The astrophysical journal*, **281**(June), 367–374.

Price, D. 2005. *Smoothed particle hydrodynamics*. Ph.D. thesis, PhD Thesis, 2005.

Price, D. J. 2007. splash: An Interactive Visualisation Tool for Smoothed Particle Hydrodynamics Simulations. , **24**(3), 159–173.

Price, D. J. 2012. Smoothed particle hydrodynamics and magnetohydrodynamics. *Journal of computational physics*, **231**(3), 759 – 794. Special Issue: Computational Plasma Physics.

Puebla, R. E., Diaz, M. P., & Hubeny, I. 2007. A statistical study of accretion disk model spectra for cataclysmic variables. *The astronomical journal*, **134**(5), 1923–1933.

Quinn, T., Katz, N., Stadel, J., & Lake, G. 1997. Time stepping N-body simulations. *eprint arxiv:astro-ph/9710043*, Oct.

Retter, A., Leibowitz, E. M., & Ofek, E. O. 1997. Permanent superhumps in nova V1974 Cygni (1992). *MNRAS*, **286**(3), 745–756.

Retter, A., Leibowitz, E. M., & Kovo-Kariti, O. 1998. Nova V1425 Aquilae 1995: The Early Appearance of Accretion Processes in an intermediate polar Candidate. *MNRAS*, **293**(2), 145–150.

Rosswog, S. 2009. Astrophysical smooth particle hydrodynamics. *New astronomy reviews*, **53**(Apr.), 78–104.

Rosswog, S. 2015. SPH Methods in the Modelling of Compact Objects. *Living reviews in computational astrophysics*, **1**(1), 1.

Rosswog, S., Speith, R., & Wynn, G. A. 2004. Accretion dynamics in neutron star-black hole binaries. *MNRAS*, **351**(4), 1121–1133.

Sawada, K., Matsuda, T., & Hachisu, I. 1986. Spiral shocks on a Roche lobe overflow in a semi-detached binary system. *Monthly notices of the royal astronomical society*, **219**(1), 75–88.

Schaefer, B. E. 1990. Orbital Periods of Recurrent Novae. *The astrophysical journal*, **355**(June), L39.

Schaefer, B. E. 2010. Comprehensive photometric histories of all known galactic recurrent novae. *The astrophysical journal supplement series*, **187**(2), 275–373.

Schaefer, B. E. 2011. The change of the orbital periods across eruptions and the ejected mass for recurrent novae and u scorpii. *The astrophysical journal*, **742**(2), 112.

Schaefer, B. E. 2013 (Jan.). The Recurrent Nova U Scorpii Blew Off A Century Worth Of Accreted Material During Its 2010 Eruption, So It Will Not Become A Type Ia Supernova. *Page 233.06 of: American astronomical society meeting abstracts #221*. American Astronomical Society Meeting Abstracts, vol. 221.

Schaefer, B. E. 2014 (June). Nova Discovery Efficiency 1890-2014; Only 43%±6% of the Brightest Nova Are Discovered. *Page 306.04 of: American astronomical society meeting abstracts #224*. American Astronomical Society Meeting Abstracts, vol. 224.

Schaefer, B. E. 2019 (June). Predictions for Upcoming Recurrent Novae Eruptions; T CrB in 2023.6±1.0, U Sco in 2020.0±0.7, RS Oph in 2021±6, and more. *Page 122.07 of: American astronomical society meeting abstracts #234*. American Astronomical Society Meeting Abstracts, vol. 234.

Schaefer, B. E., & Ringwald, F. A. 1995. An improved orbital period for the recurrent nova u scorpii. *The astrophysical journal*, **447**(1), L45–L48.

Schaefer, B. E., Pagnotta, A., LaCluyze, A. P., Reichart, D. E., Ivarsen, K. M., Haislip, J. B., Nysewander, M. C., Moore, J. P., Oksanen, A., Worters, H. L., Sefako, R. R., Mentz, J., Dvorak, S., Gomez, T., Harris, B. G., Henden, A. A., Guan Tan, T., Templeton, M., Allen, W. H., Monard, B., Rea, R. D., Roberts, G., Stein, W., Maehara, H., Richards, T., Stockdale, C., Krajci, T., Sjoberg, G., McCormick, J., Revnivtsev, Mi., Molkov, S., Suleimanov, V., Darnley, M. J., Bode, M. F., Handler, G., Lepine, S., & Shara, M. M. 2011. Eclipses during the 2010 Eruption of the Recurrent Nova U Scorpii. *The astrophysical journal*, **742**(2), 113.

Schatzman, E. 1951. Remarques sur le phénomène de Nova: IV. L'onde de détonation due à l'isotope ^3He. *Annales d'astrophysique*, **14**, 294.

Schoenberg, I. J. 1946a. Contributions to the problem of approximation of equidistant data by analytic functions, Part A: On the problem of smoothing or graduation, a first class of analytic approximation formulas. *Quart. appl. math.*, **4**, 45–99.

Schoenberg, I. J. 1946b. Contributions to the problem of approximation of equidistant data by analytic functions, Part B: On the problem of osculatory interpolation, a second class of analytic approximation formulae. *Quart. appl. math.*, **4**, 112–141.

Schreiber, M. R., Zorotovic, M., & Wijnen, T. P. G. 2016. Three in one go: consequential angular momentum loss can solve major problems of CV evolution. *Monthly notices of the royal astronomical society: Letters*, **455**(1), L16–L20.

Shafter, A. W. 2017. The galactic nova rate revisited. *The astrophysical journal*, **834**(2), 196.

Shafter, A. W., & Misselt, K. A. 2006. Modeling Eclipses in the Classical Nova V Persei: The Role of the Accretion Disk Rim. *The astrophysical journal*, **644**(June), 1104–1117.

Shafter, A. W., Darnley, M. J., Hornoch, K., Filippenko, A. V., Bode, M. F., Ciardullo, R., Misselt, K. A., Hounsell, R. A., Chornock, R., & Matheson, T. 2011. A Spectroscopic and Photometric Survey of Novae in M31. *The astrophysical journal*, **734**(1), 12.

Shakura, N. I., & Sunyaev, R. A. 1973. Reprint of 1973A&A....24..337S. Black holes in binary systems. Observational appearance. *A&A*, **500**(June), 33–51.

Shara, M. M. 1981. A theoretical explanation of the absolute magnitude-decline time /M_{B-t} sub 3/ relationship for classical novae. *The astrophysical journal*, **243**(Feb.), 926–934.

Shara, M. M. 1989. Recent Progress in Understanding the Eruptions of Classical Novae. *Publications of the astronomical society of the pacific*, **101**(635), 5.

Shara, M. M., Livio, M., Moffat, A. F. J., & Orio, M. 1986. Do Novae Hibernate during Most of the Millennia between Eruptions? Links between Dwarf and Classical Novae, and Implications for the Space Densities and Evolution of Cataclysmic Binaries. *ApJ*, **311**(Dec.), 163.

Shara, M. M., Yaron, O., Prialnik, D., & Kovetz, A. 2010. Non-equipartition of energy, masses of nova ejecta and type ia supernovae. *The astrophysical journal*, **712**(2), L143–L147.

Shore, S., Starrfield, S., Gonzalez-Riestrat, R., Hauschildt, P., & Sonneborn, G. 1994. Dust formation in Nova Cassiopeiae 1993 seen by ultraviolet absorption. *Nature*, **369**(June), 539–541.

Shore, S. N. 2002 (Nov.). Panchromatic Study of Novae in Outburst: Phenomenology and Physics. *Pages 175–187 of:* Hernanz, M., & José, J. (eds), *Classical nova explosions*. American Institute of Physics Conference Series, vol. 637.

Shore, S. N., De Gennaro Aquino, I., Schwarz, G. J., Augusteijn, T., Cheung, C. C., Walter, F. M., & Starrfield, S. 2013. The spectroscopic evolution of the γ-ray emitting classical nova Nova Mon 2012. I. Implications for the ONe subclass of classical novae. *A&A*, **553**(May), A123.

Sills, A., & Lombardi, J. C. Jr. 1997. The Importance of Realistic Starting Models for Hydrodynamic Simulations of Stellar Collisions. *The astrophysical journal*, **484**(1), L51–L54.

Skillman, D. R., Harvey, D., Patterson, J., & Vanmunster, T. 1997. Superhumps in Cataclysmic Binaries. X. V1974 Cygni (Nova Cygni 1992). *Pub. Ast. Soc. Pacific*, **109**(Feb.), 114–124.

Smith, R. C. 2006. Cataclysmic variables. *Contemporary physics*, **47**(6), 363–386.

Soraisam, M. D., Gilfanov, M., Wolf, W. M., & Bildsten, L. 2016. Population of post-nova supersoft X-ray sources. *Monthly notices of the royal astronomical society*, **455**(Jan.), 668–679.

Sparks, W. M., Starrfield, S., & Truran, J. W. 1978. A hydrodynamic study of a slow nova outburst. *The astrophysical journal*, **220**(Mar.), 1063–1075.

Springel, V. 2005. The cosmological simulation code GADGET-2. *Monthly notices of the royal astronomical society*, **364**(Dec.), 1105–1134.

Springel, V., & Hernquist, L. 2002. Cosmological smoothed particle hydrodynamics simulations: the entropy equation. *Monthly notices of the royal astronomical society*, **333**(July), 649–664.

Springel, V., Yoshida, N., & White, S. D. M. 2001. GADGET: A code for collisionless and gasdynamical cosmological simulations. *New astronomy*, **6**(Apr.), 79–117.

Starrfield, S. 1971a. On the cause of the nova outburst. *Monthly notices of the royal astronomical society*, **152**(June), 307–322.

Starrfield, S. 1971b. On the cause of the nova outburst - II: Evolution at 1.00 $M_{\odot}$. *Monthly notices of the royal astronomical society*, **155**(Dec.), 129–137.

Starrfield, S., Truran, J. W., Sparks, W. M., & Kutter, G. S. 1972. CNO Abundances and Hydrodynamic Models of the Nova Outburst. *The astrophysical journal*, **176**(Aug.), 169.

Starrfield, S., Sparks, W. M., & Shaviv, G. 1988. A Model for the 1987 Outburst of the Recurrent Nova U Scorpii. *The astrophysical journal*, **325**(Feb.), L35.

Starrfield, S., Iliadis, C., & Hix, W. R. 2008. Thermonuclear processes. *Chap. 4, pages 77–99 of:* Bode, M. F., & Evans, A. E. (eds), *Classical novae, 2nd edition*. Cambridge: Cambridge University Press.

Starrfield, S., Iliadis, C., & Hix, W. R. 2016. The thermonuclear runaway and the classical nova outburst. *Publications of the astronomical society of the pacific*, **128**(963), 051001.

Steinmetz, M. 1996. GRAPESPH: cosmological smoothed particle hydrodynamics simulations with the special-purpose hardware GRAPE . *Monthly notices of the royal astronomical society*, **278**(Feb.), 1005–1017.

Tappert, C., Schmidtobreick, L., Vogt, N., & Ederoclite, A. 2013. Life after eruption - III. Orbital periods of the old novae V365 Car, AR Cir, V972 Oph, HS Pup, V909 Sgr, V373 Sct and CN Vel. *Monthly notices of the royal astronomical society*, **436**(3), 2412–2425.

Tatischeff, V., & Hernanz, M. 2007. Evidence for Nonlinear Diffusive Shock Acceleration of Cosmic Rays in the 2006 Outburst of the Recurrent Nova RS Ophiuchi. *The astrophysical journal*, **663**(July), L101–L104.

Thoroughgood, T. D., Dhillon, V. S., Littlefair, S. P., Marsh, T. R., & Smith, D. A. 2001. The mass of the white dwarf in the recurrent nova U Scorpii. *MNRAS*, **327**(4), 1323–1333.

V. Salazar, I., LeBleu, A., Schaefer, B. E., Landolt, A. U., & Dvorak, S. 2017. Accurate pre- and post-eruption orbital periods for the dwarf/classical nova V1017 Sgr. *Monthly notices of the royal astronomical society*, **469**(4), 4116–4132.

Walder, R., Folini, D., Favre, J. M., & Shore, S. N. 2010 (Sept.). Recurrent Novae: Progenitors of SN Ia? *Page 173 of:* Pogorelov, Nikolai V., Audit, Edouard, & Zank, Gary P. (eds), *Numerical modeling of space plasma flows, astronum-2009*. Astronomical Society of the Pacific Conference Series, vol. 429.

Walder, R., Folini, D., & Shore, S. N. 2008. 3d simulations of rs ophiuchi: from accretion to nova blast. *Astronomy and astrophysics*, **484**(1), L9–L12.

Walker, M. F. 1954. Nova DQ Herculis (1934): an Eclipsing Binary with Very Short Period. *Pasp*, **66**, 230.

Warner, B. 1972. On the outburst of cataclysmic variables. *Monthly notices of the royal astronomical society*, **160**(Dec.), 35–36.

Warner, B. 2002 (Nov.). General Properties of Quiescent Novae. *Pages 3–15 of:* Hernanz, M., & José, J. (eds), *Classical nova explosions.* American Institute of Physics Conference Series, vol. 637.

Warner, B. 2008. Properties of novae: an overview. *Chap. 4, pages 16–32 of:* Bode, M. F., & Evans, A. E. (eds), *Classical novae, 2nd edition.* Cambridge: Cambridge University Press.

Warner, B. 2009. *Cataclysmic Variable Stars.*

Wendland, H. 1995. Piecewise polynomial, positive definite and compactly supported radial functions of minimal degree. *Journal of computational physics*, **4**(May), 389–396.

White, S. 1996 (Jan.). Formation and Evolution of Galaxies. *Page 349 of:* Schaeffer, R., Silk, J., Spiro, M., & Zinn-Justin, J. (eds), *Cosmology and large scale structure.*

Williams, R. 2012. Origin of the "He/N" and "Fe II" spectral classes of novae. *The astronomical journal*, **144**(4), 98.

Williams, R. E. 1992. The Formation of Novae Spectra. *AJ*, **104**(Aug.), 725.

Yaron, O., Prialnik, D., Shara, M., & Kovetz, A. 2005. An Extended Grid of Nova Models. II. The Parameter Space of Nova Outbursts. *The astrophysical journal*, **623**(Apr.), 398–410.